UNIVERSITÀ
DEGLI STUDI
FIRENZE

DOTTORATO DI RICERCA IN ENERGETICA E
TECNOLOGIE INDUSTRIALI E AMBIENTALI INNOVATIVE

CICLO XXXII
COORDINATORE Prof. Maurizio De Lucia

Analytical and Experimental Evaluation of Ejector Refrigeration System using Environmentally Friendly Fluid

Settore scientifico disciplinare ING-IND/10

PhD Candidate
Jafar Mahmoudian

Tutor
Prof. Adriano Milazzo

Co-ordinatore
Prof. Maurizio De Lucia

DE LUCIA

Firmato digitalmente da DE LUCIA
ND: cn=DE LUCIA, o=DIEF, ou=Università di FIRENZE, email=delucia@unifi.it, c=IT
Data: 2020.07.16 12:33:31 +02'00'

Firenze 2016/2019

UNIVERSITÀ
DEGLI STUDI
FIRENZE

DOTTORATO DI RICERCA IN ENERGETICA E TECNOLOGIE INDUSTRIALI E AMBIENTALI INNOVATIVE

CICLO XXXII

COORDINATORE Prof. Maurizio De Lucia

Analytical and Experimental Evaluation of Ejector Refrigeration System using Environmentally Friendly Fluid

Settore scientifico disciplinare ING-IND/10

PhD Candidate
Jafar Mahmoudian
_____

Tutor
Prof. Adriano Milazzo
_____

Co-ordinatore

Prof. Maurizio De Lucia

_____

Firenze 2016/2019

UNIVERSITÀ
DEGLI STUDI
FIRENZE

DOTTORATO DI RICERCA IN ENERGETICA E TECNOLOGIE INDUSTRIALI E AMBIENTALI INNOVATIVE

CICLO XXXII

COORDINATORE Prof. Maurizio De Lucia

Analytical and Experimental Evaluation of Ejector Refrigeration System using Environmentally Friendly Fluid

Settore scientifico disciplinare ING-IND/10

PhD Candidate
Jafar Mahmoudian
Department of Industrial Engineering, Univerity of Florence

Tutor
Prof. Adriano Milazzo
Department of Industrial Engineering, Univerity of Florence

Co-Tutors
Dr. Andrea Rocchetti
Department of Industrial Engineering, Univerity of Florence

Dr. Federico Mazzelli
Department of Industrial Engineering, Univerity of Florence

Firenze 2016/2019

Abstract

During the recent years the interest of industry and scientific community in refrigeration systems working with natural fluids has considerably grown because of the more and more strict regulations regarding environmentally safe refrigerants. This thesis mainly describes a theoretical and experimental investigation of the jet pump refrigerator, and the application of Computational Fluid Dynamic (CFD) to validate the performance of the system.

The present work is divided into two main parts plus introduction chapter which is devoted to literature reviews and theoretical concept of refrigeration system especially heat-powered ejector refrigeration cycle. Part I is devoted to the presentation of the results obtained with the industrial prototype developed by the University of Florence. Chapter 1 propose a detailed examination of the phenomena occurring in the various ejector regions with R245fa as refrigerant. The knowledge and experience of these tests sets the basic to move on the new refrigerant, R1233zd, due to the same thermodynamic properties with the previous one and low GWP. The numerical and analytical modelling of the ejector validate the experimental results of the new refrigerant that is explored in Chapter 2.

Part II is examined the fundamental study on water vapour condensation inside a supersonic nozzle operated through shock tunnel. Chapter 3 is dedicated to this issue for the final goal of the Thermo Group which is substituting synthetic refrigerant with steam as the best natural and environmentally friendly fluid. Experimental data of the condensation shocks inside a nozzle and shock behavior through the tunnel was validated with the thermodynamic theoretical and recorded photos.

Contents

Nomenclature

Latin letters		P	Precision index or random error of a measured quantity
a	Speed of sound [m s^{-1}]	*p*	Pressure [Pa]
A	Tube inlet area [mm^2]	$\dot{Q}$	Heat flux [W]
*A**	Nozzle throat area [mm^2]	*R*	Specific gas constant [J kg^{-1} K^{-1}] or Derived quantity
B	Bias or systematic error of a measure quantity	*S*	*Sampling standard derivation*
G	Gibbs Free-Energy [J]	*T*	Temperature [K]
h	Specific enthalpy [kJ kg^{-1}]	*t*	Student's estimator
k	Turbulent kinetic energy [m^2 s^{-2}]	*U*	Total uncertainty of a measured quantity
M	Mach number	*u*	Mass motion speed [m s^{-1}]
m	Mass [kg]	*W*	Wave speed [m s^{-1}]
$\dot{m}$	Mass flow rate [kg s^{-1}]	$\dot{W}$	Power [W]
x	Measured quantity	*ref*	Reference

$\bar{x}$	Average of a measuring quantity	*s*	Suction or secondary
Greek letters		*sat*	Saturation
γ	Specific heat ratio [-]	*95%*	Level of confidence in the uncertainty
ρ	Density [kg m^{-3}]	Acronyms	
ω	Specific dissipation rate [s^{-1}]	CAM	Constant Area Mixing
ε	Rate of turbulence dissipation [m^2 s^{-3}]	CFD	Computational Fluid Dynamics
θ	Sensitivity index	COP	Coefficient of Performance
μ	Condensation shock angle [rad]	CPM	Constant Pressure Mixing
Superscripts/subscripts		EOS	Equation Of State
C	Condensation	ER	Entrainment Ratio
E	Evaporation	EXP	Experimental
G	Generator	HFO	Hydro-Fluoro-Olefin
m	Motive or primary	RNG	Renormalization Group
RSM	Reynolds Stress Model		

SST	Shear Stress Transport		
TC	Thermocouple		

Introduction

Energy is one of the most debated research fields especially for the environmental impact related to many energy conversions. General concern is to protect our environment from the global warming and ozone depletion which is caused by some greenhouse gases. Refrigeration system is concerned due to the refrigerants. The international agreement have produced a gradual phase out of environmentally harmful refrigerants aimed at reducing greenhouse emission to their 1990 levels [1]. On the energy efficiency side, waste and solar thermal energy may substitute low-grade heat to electric energy input, improving refrigeration system efficiency.

Alternative refrigerants which are environmentally acceptable working fluids and waste heat driver in heat powered refrigeration system, offer a sustainable way to reduce fossil fuel consumption and refrigerant environmental impact. Systems include the absorption cycle, adsorption cycle and the jet-pump cycle.

Ejectors, as a mechanical device in the refrigeration systems, have a long history. They were used to create a vacuum in train braking systems since the 19th century. In power stations, they are used for removing non-condensable gasses from condenser. Nowadays, ejectors are commercially available in a wide range of configurations, either single or multistage. Use of ejectors in thermal systems have been developed since the early 20th century. In 1910, Maurice Leblanc proposed and built the first steam ejector refrigeration machine driven by heat, although only air conditioning application could be realized. It is interesting that he used water as refrigerant in the steam ejector refrigeration cycle [2].

Ejector theory based on one-dimensional ideal gas model was first introduced by Flügel, who applied equation of continuity, momentum and energy to the design of ejector [3] [4]. The same method of analysis of ejector is used by Keenan et al. [5] [6], who extended it to different geometries and pressure conditions

and compared its result with experimental ones. Their model showed good agreement with experimental data, though neglecting friction losses, and has been used as theoretical basis in ejector design for the past fifty years [7]. Work of Munday and Bagster [8] proposed, about a quarter of a century later, a model which considered primary and secondary flow distinct and postulated secondary flow reach sonic velocity at some cross section of the ejector. This model permitted to explain the constant cooling capacity of ejector refrigerators.

The historical path of ejector refrigeration is tightly nestled in the broader history of refrigeration. This has seen his birth and flourishing all the way in the era of the positivism, during the second half of the 19th century. There is good detail on the history of refrigeration available in books like those of Kneeass (1910) [9], Thevenot (1979) [10] or Arora (2003) [11]. Below, a non-exhaustive timeline is presented in order to give a bird-eye-view of the most relevant historical events which are specifically relevant to ejector refrigeration up to the first half of the last century.

1797 – Giovanni B. Venturi describes the “Venturi effect” which relates pressure and velocity variations of a fluid flowing through an orifice or a variable area channel

1858 – Henri, J. Giffard invents the first steam/water injector to pump a continues stream of water into boilers feeding the engines of steam locomotives

1869 – An engineer named Schau discover the advantage of the convergent/divergent nozzle for uses in steam injectors

1869 – Ernst Koerting devices and patents a double tube injector that improves the Giffard invention in terms of mass flow rate regulation

1876 – E. Koerting & L. Schutte found the “Schutte and Koetring” Company

1888 – Gustaf De Laval applies the converging/diverging nozzle (later named the “De Laval” nozzle) to steam turbines and greatly improves the rotary speed and efficiency

1901 – Sir Charles Parsons use supersonic ejectors for removing air from a steam engine's condenser

1903 – Aurel, B. Stodola demonstrates experimentally the existence of supersonic flow inside a De Laval nozzle, by measuring the axial pressure profile at various discharge pressures

1908/10 – Maurice Leblanc invents the "steam jet refrigeration cycle"

1909 – Westinghouse realize the first commercial system of steam jet refrigerator based on Leblanc's design

1926 – The French engineer Follain improved the steam jet cycle by introducing multiple stages of vaporization and condensation of the suction steam

1931 – Norman, H. Gay patents a cycle in which a two-phase ejector is used to improve the performance of refrigeration systems by partly recovering the throttling losses of the expansion valve

1940/50 – Joseph H. Keenan and his collaborators develop the first practical theory for the mixing inside a supersonic ejector, assuming either constant pressure or constant suction mixing chambers

The scheme of a standard Supersonic Ejector Cycle is shown in Figure 1. The configuration is similar to that of a conventional vapour compression machine, except the mechanical compressor is replaced by a system composed by a liquid feed-pump, vapour generator and supersonic ejector. The operation of the cycle is quite simple: the "primary" or "motive" stream arriving from the generator (high pressure and temperature – point G) flows through a de LAVAL nozzle and accelerates to supersonic speed. As it enters the mixing chambers, the primary steam entrains the "secondary" or "suction" flow coming from the secondary fluid. Subsequently, the mixed stream is compressed as it flows through the diffuser section of the ejector and enters the condenser at point C. the condensate is then split into two currents: one is expanded through a throttling valve and fed back

to the evaporator whilst the other is returned to the boiler via a feed pump.

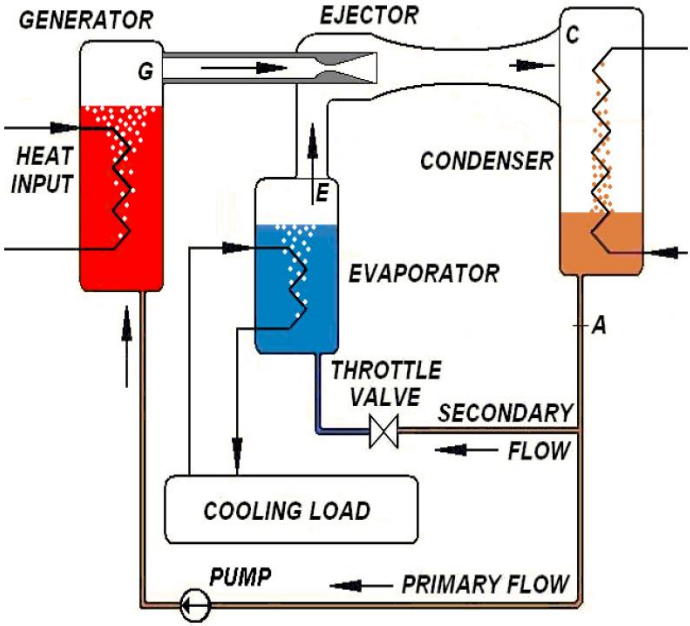

Figure 1 Schematics of the ejector refrigeration system

Basically, the whole system can be thought as composed of two parts, the power and refrigeration system. The two cycles share the condenser and the power exchange between them occurs by means of a supersonic ejector. Under stationary conditions the power output of the motive cycle must equate that absorbed by the chiller.

System performance can be quantified by means of the Coefficient of Performance (COP) that is defined as the cooling load divided by the total heat and power inputs:

$$COP = \frac{\dot{Q}_{refr}}{\dot{Q}_{gen}+\dot{W}_{pump}} = \frac{\dot{m}_s}{\dot{m}_m}\frac{(h_E-h_A)}{(h_G-h_A)} \qquad \textit{Eq 1}$$

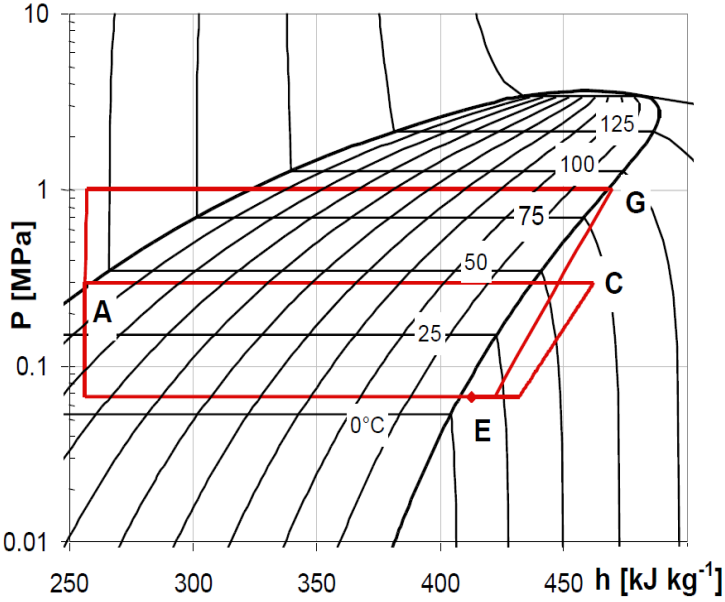

Figure 2 p-h diagram of the ejector refrigeration system

The p-h diagram in Figure 2 qualitatively illustrates the ratio between enthalpy differences in Eq 1. The ratio between the suction to motive mass flowrates defines the Entrainment Ratio (ER), which is a fundamental parameter for the performance of both the ejector chiller and the supersonic ejector:

$$ER = \frac{\dot{m}_s}{\dot{m}_m} \qquad \textit{Eq 2}$$

Figure 3 shows a typical supersonic ejector operating curve obtained at fixed evaporator and generator conditions and varying outlet pressure. The ejector's operation is said to be "on design" or in "double-chocking regime" when the mixed flow in the mixing chamber/diffuser reaches supersonic speed. Under these conditions the quantity of entrained suction flow is independent of the discharge pressure (i.e., it is chocked, whence the name double-chocking regime) and the Entrainment Ratio (ER) is

maximum. This region is the horizontal part of the operating curve in Figure 3, also called “the plateau”. On the contrary, if the mixed (or better partially mixed) flow is subsonic, the amount of suction flow drawn into the ejector depends almost linearly on the outlet pressure and the operation is said to be “off-design”. The value of discharge pressure separating these two operation zones is called “critical pressure”.

It is worth mentioning here, that the term “on-design” is not intended as the condition for which the performance of the cycle is optimized. As will be demonstrated at the end of this chapter, the best operating condition in terms of efficiency is the locus of all the critical points at the various operating temperatures. However, being the critical conditions unstable (a small pressure perturbation can lead to the subcritical regime, with substantial decrease in system COP and cooling load), practical functioning of the cycle requires operation at a certain distance from the critical points, whence the “on-design” appellation for the plateau region.

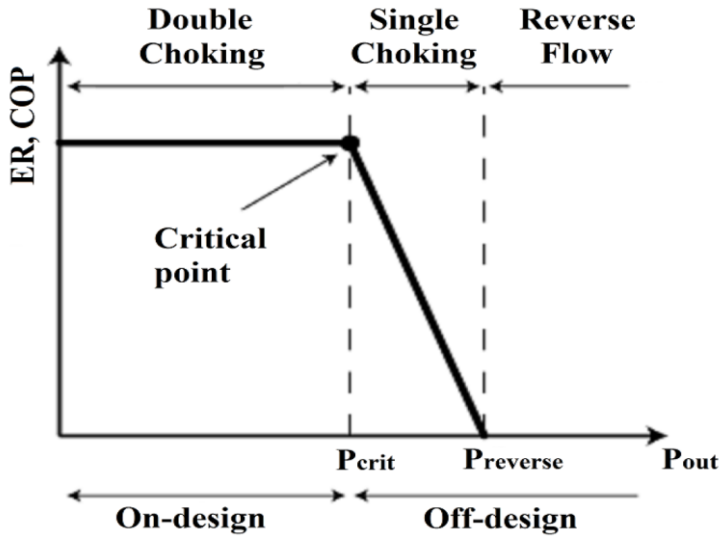

Figure 3 Typical supersonic ejector operating curve at fixed generator and evaporator P or T

When the condenser pressure goes above the critical pressure, the entrainment ratio decreases as well as the COP. Several curves can also be obtained at different generator and/or evaporator temperatures. Despite it's the most common way to describe the operation of heat powered cycle ejectors and the same conclusion is, in principle, valid for any ejector, Using ejectors to recover the throttling loss in a transcritical vapor compression cycle, does not allow for a precise control of the pressure and temperatures at the outlet of the ejector. Therefore, such an operating curve is difficult to reproduce experimentally. Moreover, since there is not a direct connection between the ejector efficiency and the system COP, any attempt to maximize the component efficiency could reduce the performance of the system. In this case the ejector should fit the required values of entrainment ratio and pressure lift that allow for the best possible COP. However, as shown in [12], this may not correspond to the highest value of component efficiency.

Figure 4 not only shows a classic COP-P_{cond} diagram with a set of operating curves at fixed evaporator temperature and different generator temperature but also shows the effect of optimal operational conditions on the performance of the system.

Supposedly that the system is operating on a point laying on the plateau of a curve with high generator temperature (point a). By ideally changing the generator temperature and keeping the condenser and evaporator temperature fixed, the operating point moves on a vertical line. At first, the point intersects curves with a higher COP that are still in the double-chocking regime (e.g., point b). However, the new operating points are closer to the critical pressure and work with a lower generator temperature. The trend is the same until the point reaches the curve that intersects the vertical line right at the critical pressure (point c). From this condition, further increase in the generator pressure drive the operating point into the off-design region of operating curves with higher generator temperatures, with a significant reduction of the system COP (point d).

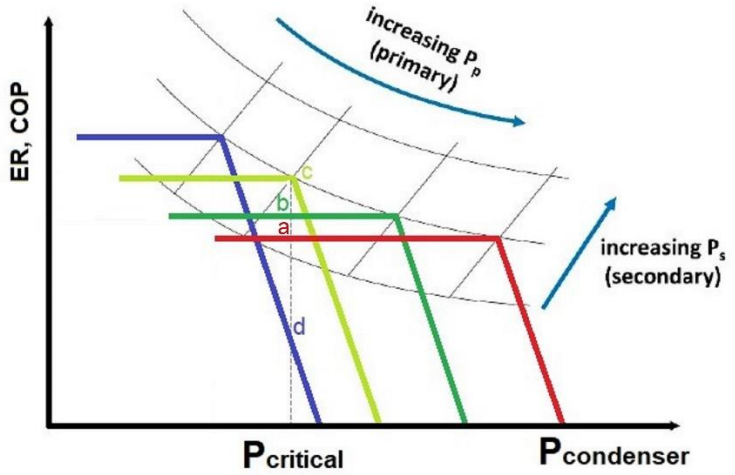

Figure 4 Operating curves at fixed evaporator temperatures and varying generator temperature

On the other side, Figure 4 shows clearly that COP of the system can be improved but with the effect of decreasing critical pressure. When the evaporator temperature increases, the higher pressure at suction inlet causes a greater secondary mass flux and, consequently, a greater ER. Higher saturation temperature of the evaporator lead also to greater critical pressures. This is due to the increase in secondary flow total pressure, which allows the mixed flow to withstand higher backpressure at the condenser. By contrast, by increasing the generator temperature, the rise in primary mass flow rate is generally not followed by a higher entrainment of the secondary stream and consequently, the ER is reduced. Nevertheless, the greater energy content introduced by the motive flow allows reaching higher backpressures, thus moving the critical point toward larger values of condenser pressures.

The ejector working principle as a passive compression device with no moving part is shown in Figure 5 where the single-phase compressible type with air and steam has been the most used [13]. This schematic represents a typical ejector lay-out, consisting of two distinct parts.

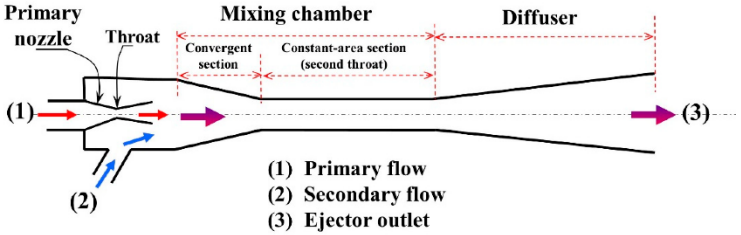

Figure 5 Schematic representation of the ejector geometry

The first part is a primary nozzle which may be simply convergent or convergent-divergent and used to expand a primary fluid, converting in the process its potential energy into kinetic energy. The primary nozzle convergent outlet corresponds to the first throat of the ejector.

The external part of the ejector constitutes in effect the secondary nozzle and comprises three zones: the convergent section, the second throat or constant-area section and the diffuser. The convergent suction chamber is the part where the expansion of a high-pressure (motive or primary, red points) fluid from the Generator is used to entrain and compress a low-pressure (suction or secondary, blue points) fluid by means of momentum transfer between the two streams of fluid (Figure 6) and guide them to the ejector second throat in the form of a cylinder with constant cross-section. The diffuser consists of a divergent, generally a reversed cone, following immediately after the second throat. [14].

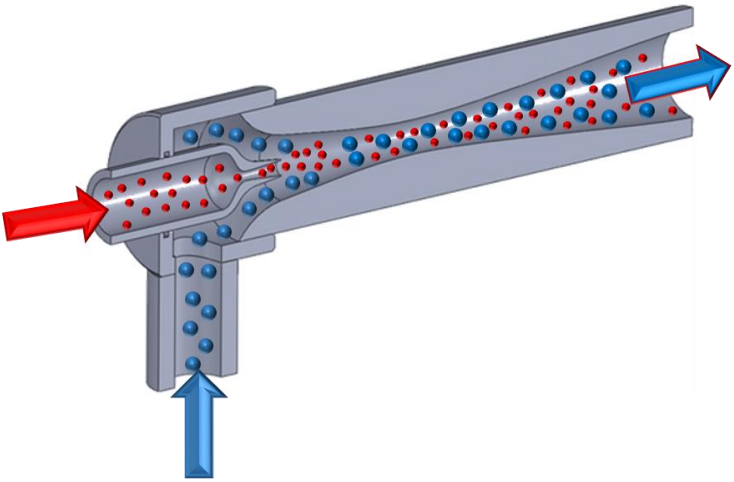

Figure 6 Ejector working principle

There are two different jet pump designs based on one dimensional theory which were proposed by *Keenan et al.* at 1942 and 1950 [5] [6]. Firstly, he introduced Constant Area Mixing CAM (Figure 7a [14]) considering mathematical analysis based on an ideal gas dynamic. This model has a constant cross-sectional area along the entire mixing chamber and is supposed to have a good performance by entraining a large amount of secondary flow.

The second concept is Constant Pressure Mixing CPM (Figure 7b [14]) that has a variable cross section zone immediately before the constant cross section part with the primary nozzle exit located at the inlet or within this zone and providing a wider range of condensing pressures. This design is the most commonly encountered due to the fact that it has better performance and more favorable comparison against experimental data.

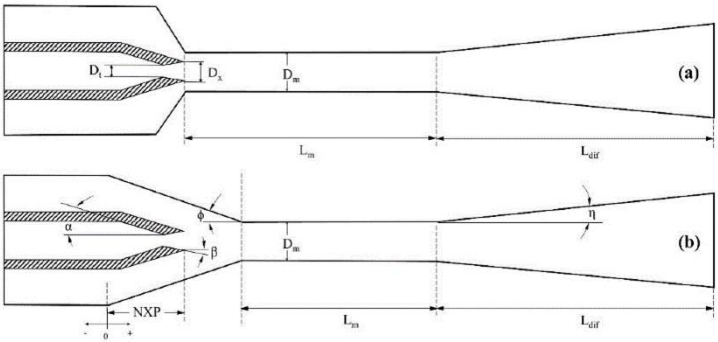

Figure 7 Constant area mixing (a) and constant pressure mixing (b) ejector geometry

There are many investigations to compare CAM and CPM, not only experimentally but also numerically under the same operating condition. They confirmed that the CAM offers higher entrainment but lower compression than CPM [14] [15] [16] [17].

Figure 8 shows the behavior of the flow in terms of static pressure and velocity based on Munday and Bagster's 1977 paper [8]. The primary flow enters the ejector at relatively high pressure (section p) and its pressure decreases while its velocity increases when flowing through the nozzle. The primary flow reaches the sound speed at the nozzle throat (section t), and even higher velocity at the nozzle exit (section 1) and further higher velocity at the exit of primary flow core (section 2). The secondary flow (section s) is sucked into the ejector and is accelerated to sound speed at the hypothetical throat (section 2) formed by the boundary of the primary flow core and the ejector wall. In the meantime its pressure reduces to the same value as that of the primary fluid at section 2. The mixing takes place between sections 2 and 3, where the pressure of the mixed stream increases due to the constant mixing area. The normal shock occurs at section 'sh' where the pressure increases and the velocity drops to subsonic level. Finally, the pressure of the working fluid is promoted and the velocity drops after flowing through the diffuser (from section 4 to d) [18] [19].

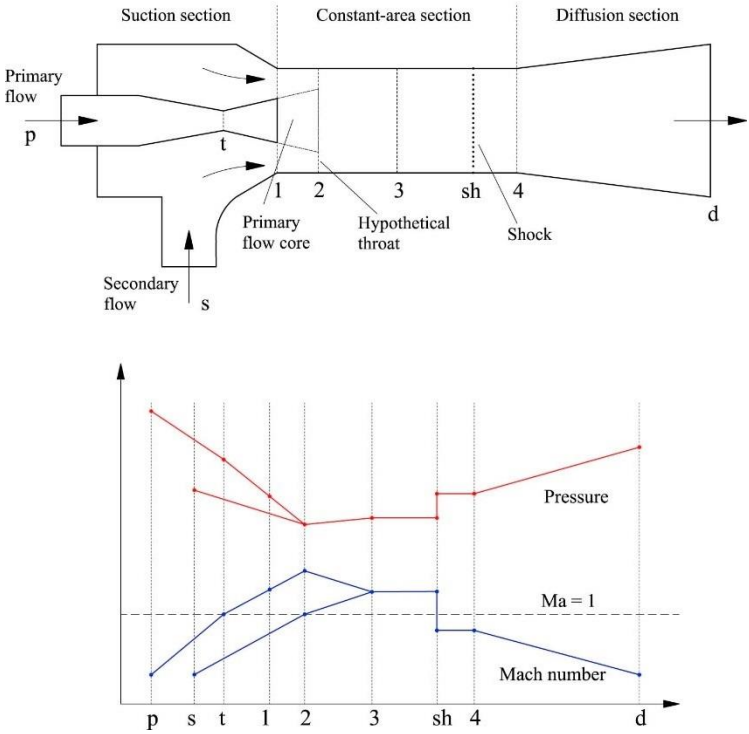

Figure 8 Schematic view of jet pump and pressure-velocity variation along jet pump according to Mundary and Bagster' theory

Part I: Ejector Refrigeration System Working with Environmentally Friendly Fluids

1 Ejector cycle working with R245fa

The part of the thesis about experimental activity on R245fa is described in this Chapter. The results shown in this chapter have been published in [20].

1.1 Overview

The design and optimization of the DIEF prototype ejector chiller, which is operating since 2011 and has undergone several refinements, have been discussed elsewhere. The prototype features a modified CRMC design of the ejector and a cooling power of a 40 kW_f. The working fluid, R245fa, has favorable thermodynamic properties (e.g. dry expansion and moderate pressure at generator) and allows sub-zero temperatures at evaporator. Therefore, even if the prototype was designed for 5°C evaporation temperature, a set of low temperature tests has been carried on. The results show that the CRMC ejector chiller is rather flexible with respect to off-design conditions and, once specifically optimized, could be a candidate for sub-zero applications, unfeasible for water-lithium bromide absorption chillers.

1.2 Experimental Apparatus

1.2.1 Hydraulic part

The hydraulic part consist of a cooling tower, a storage tank, pumps, flowmeters and pipes which are shown in Figure 1.1, Figure 1. 2 and Figure 1.3. The design and calculation of this part was done in Microsoft Excel and checked in MATLAB and LABVIEW, also. In this part, we added an expansion tank on the top of the system, higher than condenser, to keep it filled

and bypass pipes to control the pumps because they have no inverter.

Figure 1.1 Cooling tower

Figure 1. 2 pump on the chilled water loop and Coriolis mass flow meter

Figure 1.3 Hydraulic pipes

The final scheme of the bench was drawn in 3D and AutoCAD software, fitting all pipes with respect to our laboratory walls and free space (Figure 1.4 and Figure 1.5).

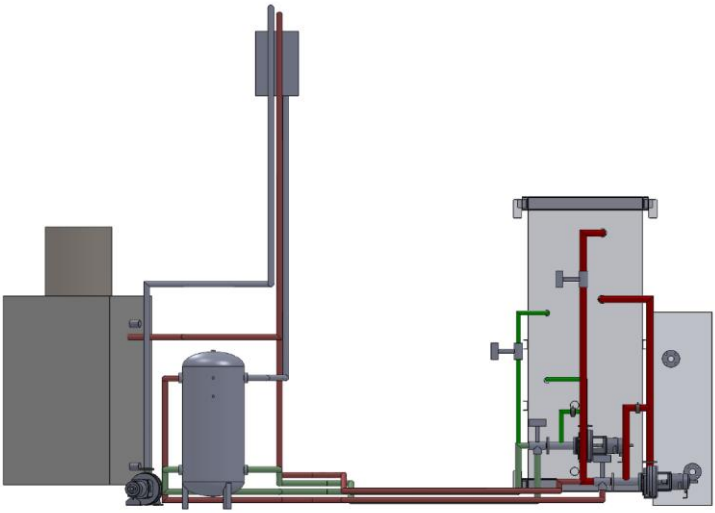

Figure 1.4 3D scheme of hydraulic part, side view

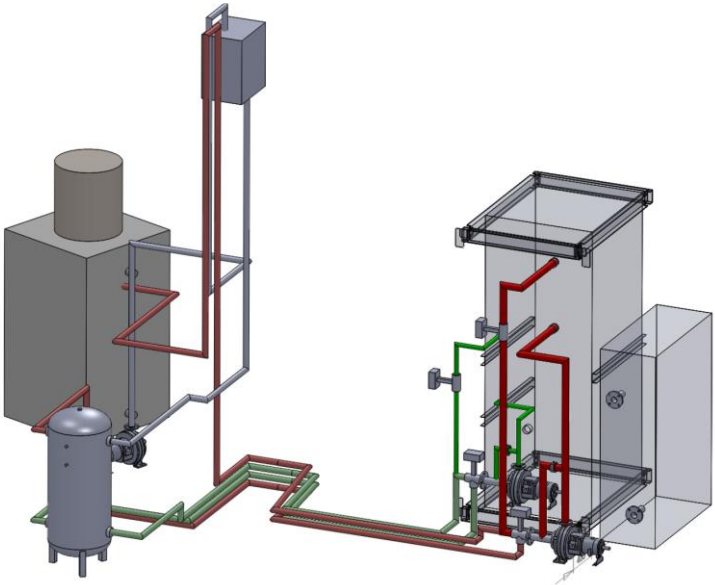

Figure 1.5 3D scheme of the hydraulic part, panorama view

Also, Figure 1.6 shows the calculated pressure drop in all hydraulic pipes considering fitting parts by the Pipe Flow Expert software in order to choose the right length and size of the pipes, considering the power of the system pumps in the simulation. Subsequently, the hydraulic part of the test bench has been built and tested, showing substantially correct operation.

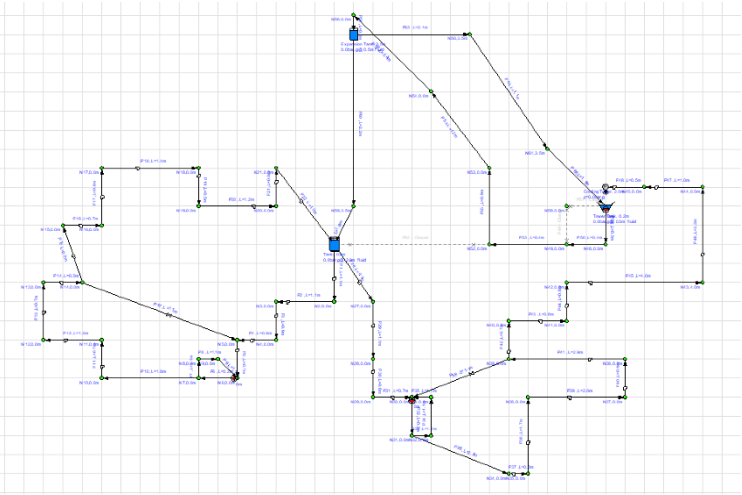

Figure 1.6 Pipe Flow Expert simulation of the hydraulic part

1.2.2 Heater

Originally a heater using water was employed, but subsequently it was decided to use a commercial heater that works on thermal oil, in order to be able to reach higher temperature without safety problems.

Figure 1.7 twk heater, APOLLO 90 OAE

Company	twk srl
Model	APOLLO 90 OAE
Installed power	98.5 kW
Project temperature	200°C
Fluid	Therminol oil
Total thermal potential	90 kW
Number of resistors	2

Table 1.1 Heater properties

1.2.3 General view

This heat-powered refrigeration system (Figure 1.8) is designed to give 40 kW of refrigeration to a chilled water stream entering at 12°C and exiting at 7°C. A vertical layout saves floor-space and guarantees a substantial liquid head between the condenser (on top) and the generator feed-pump (Figure 1.9, on the bottom). This latter is a multi-stage side-channel pump, featuring a good resistance to cavitation.

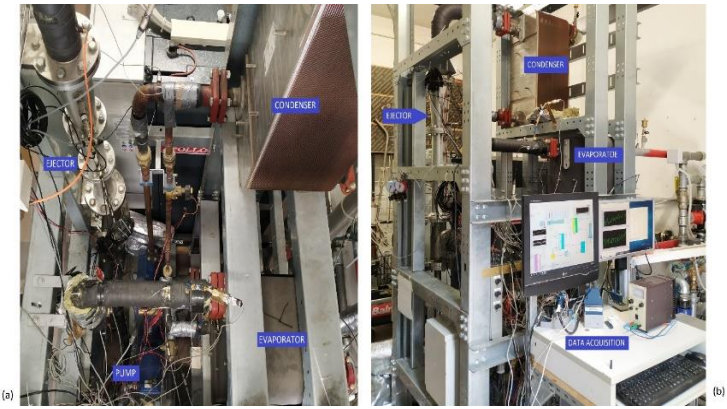

Figure 1.8 Top (a) and side (b) view of prototype

Figure 1.9 Speck pumpen SK20 7stage side-channel pump with magnetic coupling and inverter

The evaporative cooling tower discharges the system power into the ambient air outside the laboratory. The cooling tower receives the warm water directly from the condenser and feeds a buffer tank, in order to have a stable water source at near ambient temperature. The tank water is used to give the heat load to the evaporator and to cool the condenser. By-pass branches are used to regulate the temperature at evaporator and condenser inlets (Figure 1.10).

1. Ejector cycle working with R245fa

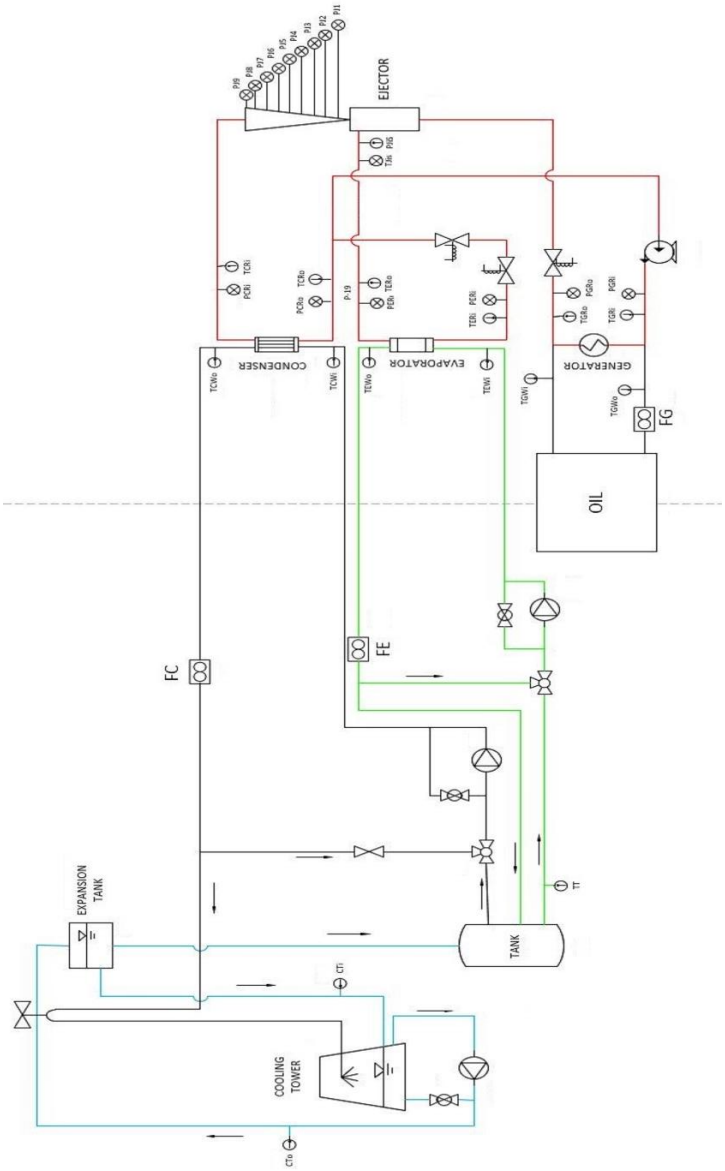

Figure 1.10 Experimental setup

1.2.4 Ejector Design

The ejector was designed following the CRMC (Constant Rate of Momentum Charge) criterion that was introduced in 2002 by Ian Eames [21]. The continuous profile generated by the CRMC criterion is free from sharp turns of the flow and may be easily optimized by setting the rate of momentum change, which dictates the length of the diffuser. This is beneficial in terms of efficiency, either in terms of entrainment ratio or compression ratio [22]. Recently Kitrattana *et al* [23] reported a comparison between a CRMC and a conventional steam ejector in the same conditions and found that the CRMC has a 40% higher entrainment ratio.

The manufacturing problems due to the small inner diameter and substantial length forced the ejector to be built in three pieces, carefully aligned by flanged connections. In this way, a roughness of the internal surface from 4 to 6 microns was obtained. A bell shaped mouth has been added to the CRMC profile on the suction side, while on the discharge side the profile has been reduced to a straight cone as soon as divergence angle overcomes 5°.

The present arrangement is the result of a long refinement work, as described in previous publications [24] [25]. Main geometrical data of the ejector in the present configuration are reported in Table 1.2.

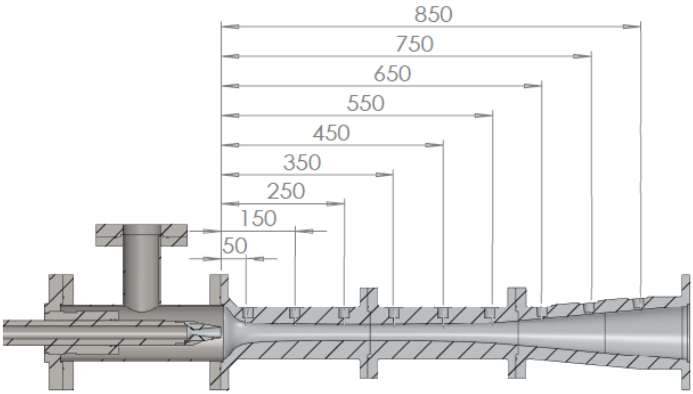

Figure 1.11 CRMC ejector with static pressure ports and moveable primary nozzle

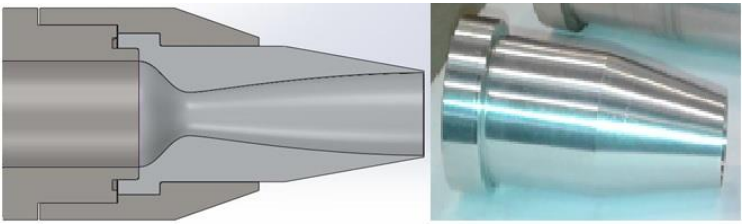

Figure 1.12 Motive nozzle

	Nozzle	Diffuser
Throat diameter [mm]	10.2	31.8
Exit diameter [mm]	20.2	108.3
Length [mm]	66.4	950
Material	Aluminium	Aluminium

Table 1.2 Main geometrical parameters of the ejector

Nine ports have been drilled perpendicularly to the ejector inner surface in order to measure the local static pressure. The holes are placed at 100 mm intervals, starting at 50 mm from the inlet

flange of the ejector, as shown in Figure 1.11. The primary nozzle (Figure 1.12) can be moved forward and backward from a reference position having the nozzle exit plane coincident with the inlet plane of the bell-shaped inlet of the suction chamber.

1.2.5 Measuring Sensors and Data Acquisition

Mass flow meters and temperature sensors are mounted on the condenser and evaporator water circuits, in order to have the instantaneous energy balance of the system. Temperature and pressure sensors are mounted in all the significant points along the refrigerant circuit. The specifications of the main sensors are reported in Table 1.3.

LABVIEW 2014 software was used to acquire sensors signals and made some calculations during experimental tests to assist us for controlling the system. Figure 1.13 shows the final view of the LABVIEW code.

1. Ejector cycle working with R245fa

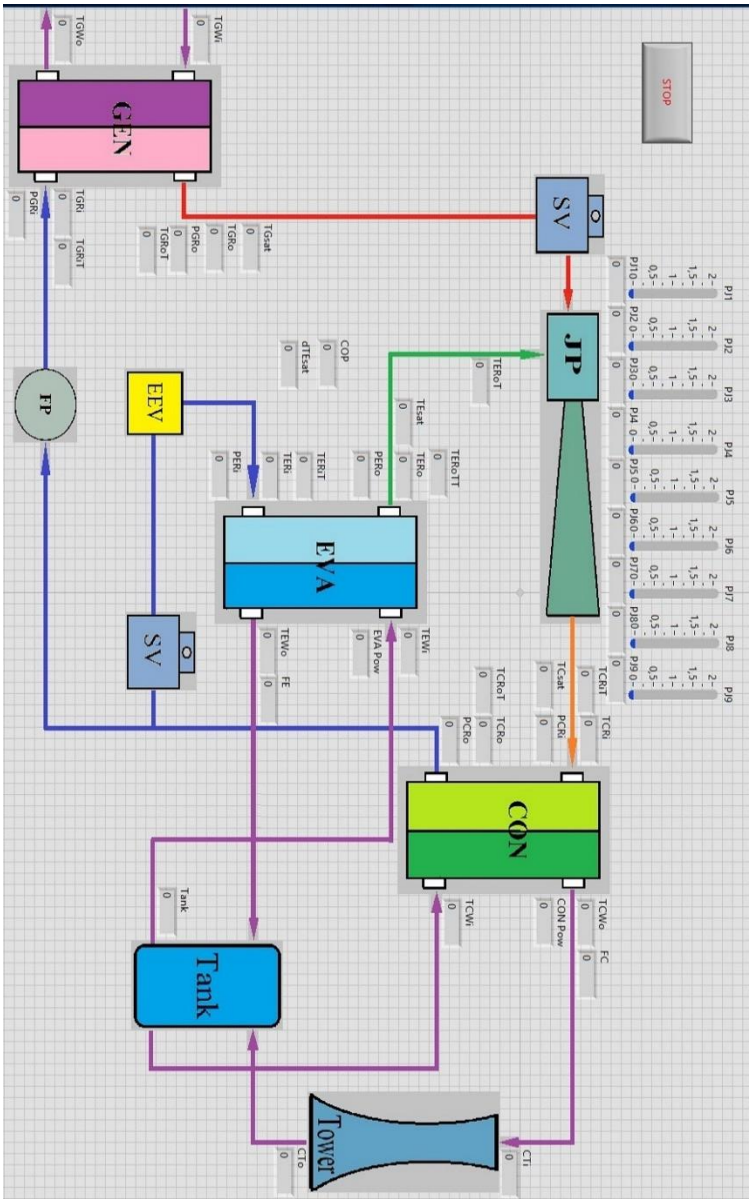

Figure 1.13 Acquiring data program scheme in LABVIEW

Instrument	Model/type	Position	ADC Module	Total uncertainty
Piezoresistive pressure transducer	PA25HTT 0-30 bar	Diffuser	NI9208	±(0.1% + 0.22% FS)
	PR23R 0.5-5 bar	Evaporator	NI9208	±(0.1% + 0.22% FS)
	PA21Y 0-30 bar	Generator, Condenser	NI9208	±(0.08% + 1.0% FS)
Resistance temperature detector	Pt100	Whole Plant	NI9216, NI9217	±0.25°C
Thermocouple	T	Whole Plant, Cooling Tower, Tank	NI9213	±1.0°C
Electromagnetic water flowmeters	Endress Hauser Promog 50P	Condenser	NI9219	±(0.5% + 0.04% FS)
Compact Rotamass mass flowmeter	YOKOGAWA RCCT28	Evaporator	NI9219	±(0.05% + 0.1% FS)
Vortex flowmeter	YOKOGAWA YF105	Generator	NI9219	±(0.8% + 0.1% FS)

Table 1.3 Specification of the transducers and data acquisition modules

Calibration procedure can include: offset factors, scale factors or a combination of them. With a calibration it's also possible to define the characteristic function that allows to pass from the indication of the instrument to the physical parameter that we want to evaluate. For example, resistance thermometers give an indication of the temperature under the form of a resistance, while thermocouple give a voltage.

Calibration of the thermocouple was based on a thermostatic bath as testing environment and a resistance thermometer as a reference instrument. Activities carried out are:

- Characterization of reference instrument, with the construction of resistance-temperature equations and tolerance equations;
- Analysis of the stability of the thermostatic bath;
- Construction of calibration curves for the instruments under test; and
- Evaluation of uncertainty;

Many tests have been done during many days resulting in a large amount of data being generated, so we had to:

- Acquire a certain number of reference temperature in a quite wide range. There is no need to have many reference points in a limited range or to have very few of them in a very wide range;
- Understand how long the bath is able to maintain a set temperature;
- Repeat the measurement to obtain reference points for heating and cooling of the bath's liquid.

(Thermostatic bath FK2 produced by *Gebrüder Haake. An internal refrigeration cycle and a heating resistance adjust the temperature. The refrigeration cycle is always working, the resistance has a power that can be set from 0 to 1 kW (0.1, 0.2 …). Under 0.4 kW the resistance can't heat the*

liquid because of the action of refrigeration cycle. The testing liquid is a solution of 50% water – 50% ethylene glycol. Bath has been used for calibration in the range [-30; 60] °C.)

At each reference point, we have the temperature of the instrument (Inst) acquired at the same time of the reference RTD and the two readings are compared on the calibration point. For n = 60 observations, sampling standard derivation is evaluated with this formula:

$$S(x) = \sqrt{S^2(x)} = \sqrt{\frac{1}{n-1}\sum_{i=1}^{n}(x_i - \bar{x})^2} \qquad \textbf{Eq 1. 1}$$

In Table 1. 4 *there are:*

- *The combined standard uncertainty (u_c), useful for the interpolation method.*
- *The difference between temperature of reference RTD and instrument, used for the paired data test; T_{ref}-T_{TC} (°C)*
- *The result of the test for paired data; test is satisfied if Student's distribution (t) is higher than 2.66. The value of the Student's distribution has 59 degrees of freedom and a confidence interval of 99%.*

T_{ref} (°C)	T_{TC} (°C)	u_c (T_{true})(°C)	T_{ref}-T_{TC} (°C)	t
-26.91	-27.70	0.031	0.79	12.77
-18.85	-19.51	0.033	0.65	18.43
-9.52	-10.18	0.021	0.66	19.96
0.55	-0.04	0.020	0.59	18.63
10.36	9.91	0.044	0.45	14.11
20.56	19.94	0.025	0.62	15.78
30.11	29.45	0.034	0.66	14.91
40.00	39.44	0.036	0.57	19.06
50.15	49.64	0.036	0.50	14.55
60.06	59.53	0.037	0.54	19.81

Table 1. 4 Points to calibrate thermocouple

Since uncertainty isn't the same for each point, the linear interpolation method calculated uncertainties at each state for T_{true}. The calibration curve is:

$$T_{true} = 0.638 + 0.998 * T_{inst} \qquad \textit{Eq 1. 2}$$

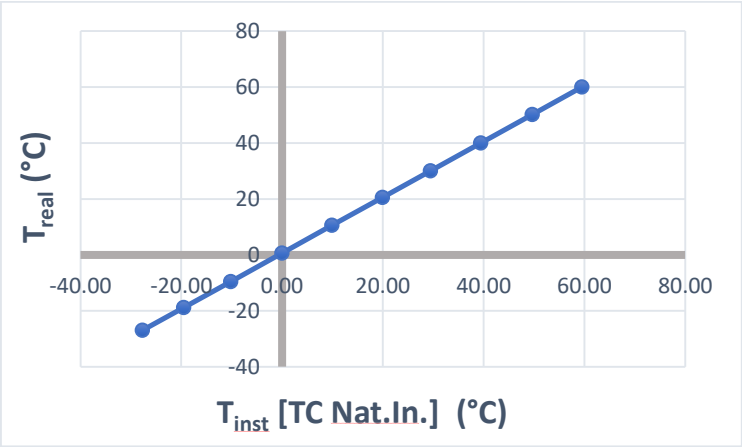

Figure 1.14 Calibration curve for thermocouple

1.2.6 Measurement and Uncertainty

The basic idea of measurement uncertainty is well explained by many authors [26] [27] [28]. Here, we follow the more specific procedure referred to as "multiple sample" or "multiple measurement" uncertainty analysis. All uncertainties are evaluated with a confidence level of 95%. Bias or systematic errors are calculated by summing up the contribution stated by the manufacturers for both the instrument and data acquisition system.

During data acquisition, each experimental point is obtained by averaging over a period longer than the longest period contained in the signal waveform. This is done in order to avoid interference errors [27]. The "precision index" or "random error" are evaluated by taking the "standard deviation of the mean" for

each measured quantity. The total uncertainty for each measured quantity is thusly given by:

$$U_{95\%} = \sqrt{(B)^2 + \left(t_{v,95}P\right)^2} \qquad \textit{Eq 1. 3}$$

Where B is the total bias or systematic error for the measured quantity, P is the precision index or random error for the measured quantity, $t_{v,95}$ is the "Student's t estimator" and v are the number of acquisitions. Rigorously, v should be number of degree of freedom and the t estimator should be evaluated by the Student's t distribution. However, when the number of acquisitions is higher than ~ 60 (as in our tests) the t estimator can be considered ~ 2 and the difference between the degrees of freedom and the number of acquisition can be safely neglected.

Error propagation for "derived quantities" (power, mass flow and enthalpies) is evaluated by square summation of the various "sensitivity indexes" (sometimes called partial uncertainties):

$$U_{95\%-derived} = \pm\sqrt{\sum_i \left(\frac{\partial R(x_i)}{\partial x_i}.\partial x_i\right)^2} = \pm\sqrt{\sum_i (\theta_i.\delta x_i)^2} \qquad \textit{Eq 1. 4}$$

Where Rx_i is the "derived quantity", which is function of several "measured quantities" x_i (e.g. temperature, pressure, etc…); θ_i is the sensitivity index, which represent the variation of the derived quantity subject to a variation δx_i of the measured quantity.

In the absence of an analytical formulation for the derived quantity (e.g. when evaluating the enthalpy of the refrigerant through NIST libraries), the sensitivity indexes are evaluated by "sequential perturbation" of the result [28], that is, by numerically evaluating the sensitivity index as follows:

$$\frac{\partial R(x_i)}{\partial x_i} = \frac{1}{2}\left(\left|\frac{R(\bar{x}_i + \delta x_i) - R(\bar{x}_i)}{\delta x_i}\right| + \left|\frac{R(\bar{x}_i) - R(\bar{x}_i - \delta x_i)}{\delta x_i}\right|\right)$$

Eq 1. 5

Where the bar over x_i indicate the average of the "measured quantity".

The experimental error obtained for derived quantities such as mass flow rates, ER and COP depends on the working condition and the reported graphically in the results presented in Chapter 2.

1.3 Working Fluid, R245fa

Synthetic fluids may have some peculiar advantages. A first point is undoubtedly the volumetric cooling capacity. Water, notwithstanding its unrivalled latent heat, has a very low vapour density at low temperature (Table 1.5), while common refrigerants have much higher values. The influence of volumetric cooling capacity on the size of an ejector chiller is not as straightforward as in vapour compression cycles featuring volumetric compressors. However, the values in Table 1.5 suggest that a steam ejector chiller is likely to be much more bulky for a given cooling capacity.

Fluid	Latent heat [kJ/kg]	Vapour density [kg/m^3]	Volumetric cooling capacity [kJ/m^3]	Saturation pressure [bar]	
				@ 0°C	@ 100°C
Water	2501	0.00485	12.13	0.00612	1.014
R134a	198.6	14.43	2866	2.929	39.72
R245fa	204.5	3.231	660.7	0.5295	12.65
Fluid properties calculated via NIST REFPROP [10]					

Table 1.5 Fluid properties – comparison

A second point is the operating pressures within the various parts of the chiller. Water has very low saturation pressure at all temperature levels encountered along an ejector cycle. The generator, if operated e.g. at 100°C, is at ambient pressure, but the evaporator typically works below 1 kPa. This requires very accurate sealing of the circuit. On the other hand, R134a has a

rather high pressure at typical generator temperatures (Table 1.5), which makes the operation and the energy consumption of the generator feed-pump more troublesome. R245fa is a good compromise, as it goes slightly below ambient pressure at evaporator but remains within a moderate 12.6 bar at 100°C.

A third point is the slope of the upper limit curve on the temperature – entropy diagram. R245fa has an inward slope of the limit curve. This means that the primary nozzle and the whole ejector are free from liquid condensation even if the expansion starts on the limit curve with no superheating. R134a and water, on the other hand, have a "wet expansion" and therefore they need a substantial superheating at generator exit (Figure 1.15).

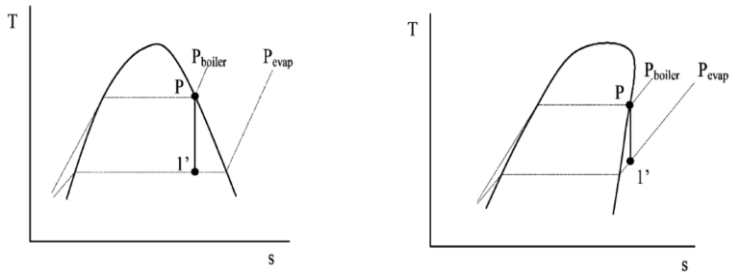

Figure 1.15 Typical TS diagram for wet (left) and dry (right) expansion fluid

A last point that favors synthetic fluids is the absence of icing, which may represent a serious problem for steam ejector chillers and limits their operation to above zero.

On the other hand, F-gas regulations limit the use of fluids with GWP>150 in Europe and other countries have similar limitations. Therefore R245fa (GWP = 950) could prove unusable in most applications. HFOs (Hydro-Fluoro-Olefins) are currently proposed as "drop-in" replacement of HFCs [30]. Among them, R1233zd has similar thermodynamic properties and hence experimental results gathered with R245fa may be an indication for the performance of an equivalent system using the low-GWP alternative fluid.

Everything considered, we decided to continue our experimental activity on the existing prototype and to substitute R245fa with R1233zd that will be discussed in Chapter 2.

R245fa was tested as a working fluid for an ejector chiller in 2006 by Eames et al. [22].The ejector was a CRMC design, i.e. the flow sections were calculated by imposing a constant rate of deceleration along the mixer/diffuser. The experimental results showed that, for saturation temperatures of 110°C at generator and 10°C at evaporator, the COP could be as high as 0.47, with a critical condenser temperature of 32.5°C. Raising generator temperature to 120°C decreased the COP to 0.31, but the critical condenser temperature increased to 37.5°C. Superior performance of CRMC design has been recently confirmed in [23].Here we present further experimental results from a modified version of the CRMC ejector, which has been tested on a wide range of operating conditions.

1.4 Results and Discussion

All the experimental points have been measured after at least 15 minutes of stable operation and are averaged over 3 minutes. The generator feed pump has a variable frequency control, but has been always operated at 100% rotation speed. The expansion valve is manually operated in order to fix the saturation temperature at the evaporator.

All saturation temperatures reported below are calculated from the pressure measured on top of each plate heat exchanger via NIST REFPROP functions. The experiments presented herein are all referred to a saturation temperature of 95°C, at generator, corresponding to the maximum power of the thermal oil electric heater. The expansion valve is manually operated in order to fix the saturation temperature at the evaporator.

For each evaporator condition, the water temperature at condenser inlet is raised by 0.3°C intervals until the cooling power vanishes. The results are reported in terms of COP v/s saturation temperature at condenser.

The higher generator temperature used in these new tests produces lower COP values with respect to those reported in [3]. Furthermore, entrainment ratio and COP have been negatively influenced by the decision to keep chilled water temperature constant (12°C at inlet and 7°C at outlet) throughout the test campaign. This causes a high superheating at evaporator exit, especially at low evaporation temperature, and hence a low vapour density at secondary inlet. On the other hand, the relatively high water temperature avoids any risk of icing.

1.4.1 Effect of Evaporator Saturation Temperature

The system behavior in terms of COP at reference working condition ($T_{E\text{-}sat}$ = 5°C, P_E = 0.662 bar) in Figure 1.16 shows a fairly constant value until point 5 and a sudden decrease at a condenser saturation temperature $T_{C\text{-}sat}$ around 31°C, before point 6.

Correspondingly, the static pressure at the wall measured by the 9 pressure transducers shows two easily distinguishable shapes (Figure 1.11). Note that the lines connecting the points are drawn only as a visual aid and do not give any indication about the pressure between the sensors. The curves from 1 to 5 all show a common pressure value at transducers 1 - 3, i.e. until 250 mm from the ejector inlet. The transition between supersonic and subsonic flow is apparently located between 250 and 350 mm, all sensors downstream being sensitive to the condenser pressure. Note that the diffuser throat is located around 300 mm.

The two further points 6 and 7 show a completely different behavior, featuring a sharp pressure increase before 250 mm and then a slower increase before 550 mm. In any case the pressure recovery after 550 mm is null or even negative, which raises some concern about the design of the final part of the ejector.

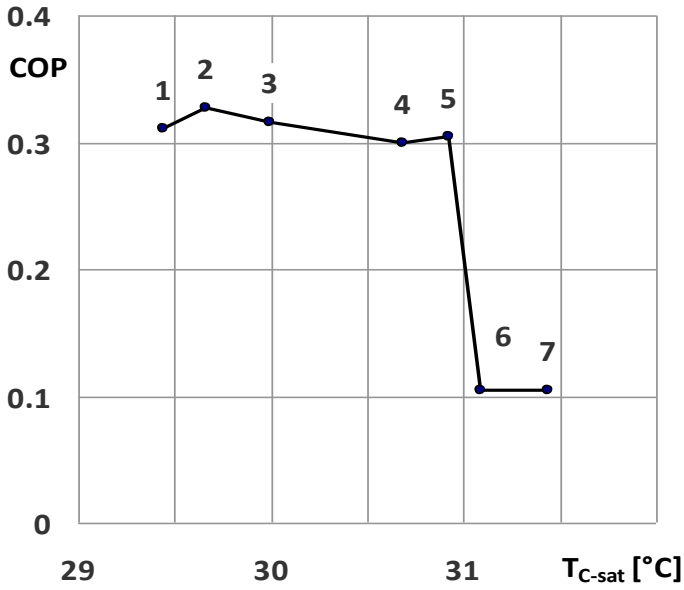

Figure 1.16 COP, $T_{E\text{-}sat}$ = 5°C and NXP = 0 mm

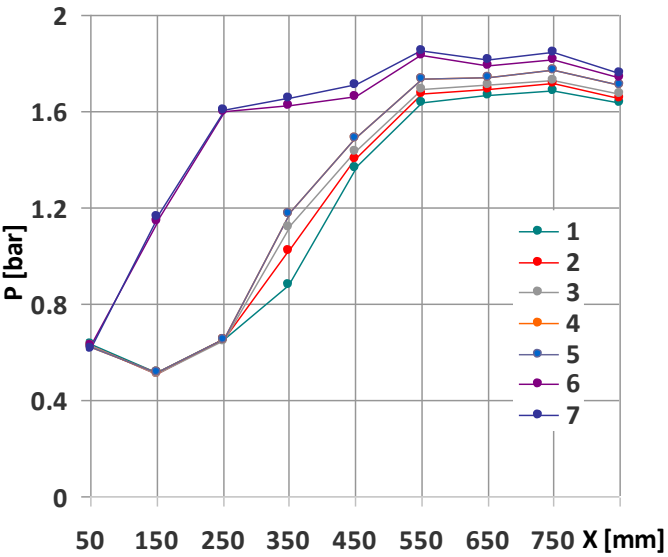

Figure 1.17 Static pressure at wall along the ejector, $T_{E\text{-}sat}$ = 5°C and NXP = 0 mm

Points 6 and 7 show that, once the critical pressure has been surpassed, a small secondary flow can still survive to a further small increase in condenser pressure. This part of the curve is usually truncated and is obviously not significant as a practical working condition. However, it is a quite general feature and represents a safety margin before a dangerous backflow.

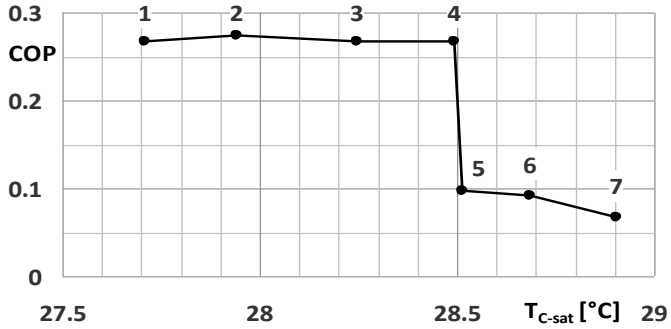

Figure 1.18 COP, TE-sat = 0°C and NXP = 0 mm

When the evaporation temperature is lowered to 0°C (P_E = 0.529 bar), the behavior changes as shown in Figure 1.18. Note the lower values of COP and critical pressure. Again, the operation continues beyond the critical condenser temperature even if at very low efficiency.

Further reduction of the evaporation temperature to -5°C (P_E = 0.419 bar) obviously gives an even lower COP and a very low range in terms of condenser temperature (Figure 1. 19). However, the ejector proves to be able to reach such a low value of suction pressure (Figure 1.20), even if designed for a quite different working condition. The transition between on-design and off-design operation is abrupt as in Figure 1.17.

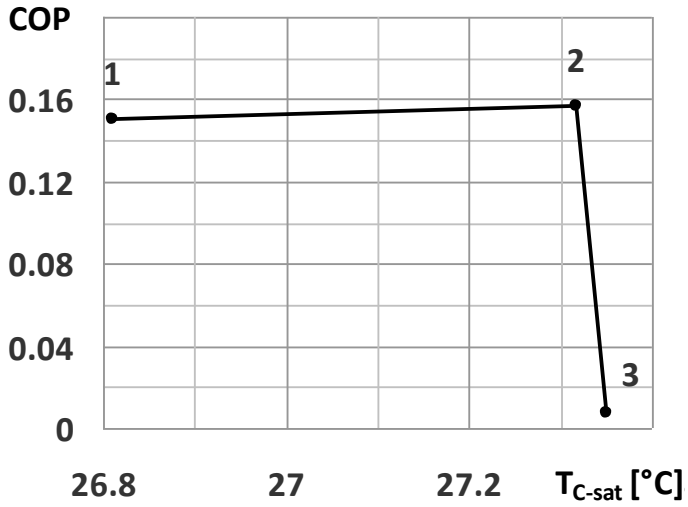

Figure 1. 19 COP, $T_{E\text{-}sat}$ = -5°C and NXP = 0 mm

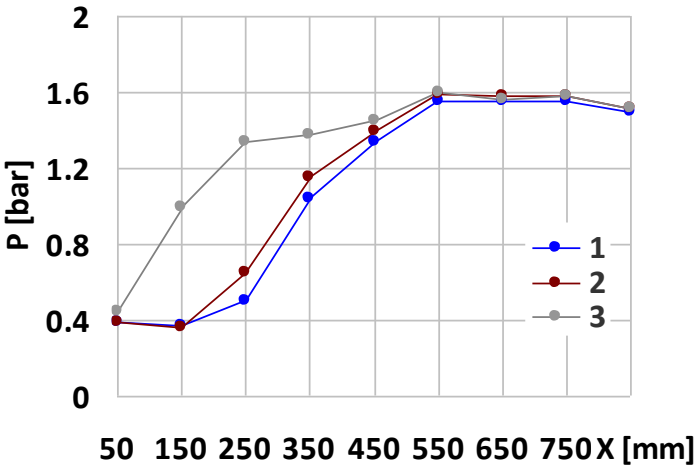

Figure 1.20 Static pressure at wall along the ejector, $T_{E\text{-}sat}$ = -5°C and NXP = 0 mm

1.4.2 Effect of Nozzle Position

According to the widely accepted model presented by Huang et al. [31] for the supersonic ejector operation, the entrainment ratio should be influenced by the area available for the secondary flow in the section where this latter reaches its sonic velocity. According to this view, an increase in the distance between the nozzle exit and the minimum area of the diffuser should cause an increase in the area occupied by the primary flow and hence a decrease in the secondary flow rate. A more realistic view sees the ejector as a momentum exchanger between the supersonic primary flow and the slow secondary flow [32]. Accordingly, an increased mixing length between the motive and entrained flow should actually increase the entrainment.

In the case of present measurements, the situation is complicated by the absence of a cylindrical mixing zone within the diffuser. The available flow section changes continuously from the inlet to the throat of the CRMC diffuser. This makes the effect of the nozzle exit position quite unpredictable.

The experimental results (Figure 1.21) show that the COP measured with the primary nozzle retracted by 5 mm from the design position is actually reduced by a very modest amount, if any. The critical condenser temperature, on the other hand, is significantly decreased. This may be explained considering that a withdrawal of the nozzle causes a corresponding retraction along the diffuser of the section where the flow is fully supersonic. Hence, the working condition that causes this section to overcome the diffuser throat is anticipated.

Another interesting point is the completely different shape of the decreasing part of the COP line. In this case, the transition seems to take place in a rather gradual way, in lieu of a sharp decrease as shown in Figure 1.16. Correspondingly, the pressure lines in Figure 1.22 are equally spaced between the lowest one, surely representing an on-design condition, to the highest. As explained in [11], the primary flow undergoes a sequence of oblique shocks starting from the interface between super and subsonic flow and featuring multiple reflections on the axis and

on the interface. The sequence of sharp descents and less inclined parts visible in Figure 1.18 could be a trace of the interaction between the oblique shocks and the ejector profile.

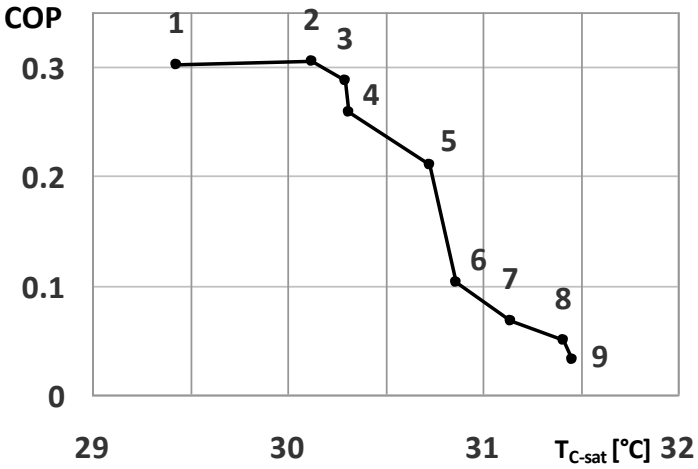

Figure 1.21 COP, $T_{E\text{-}sat}$ = 5°C and NXP = 5 mm

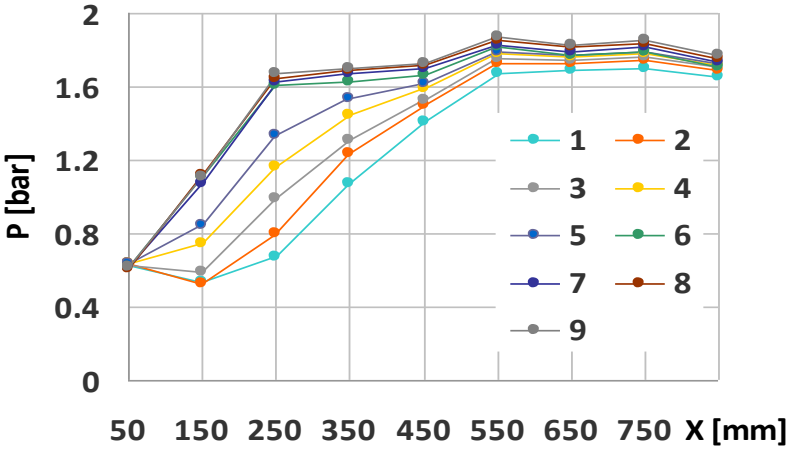

Figure 1.22 Static pressure at wall along the ejector, $T_{E\text{-}sat}$ = 5°C and NXP = 5 mm

Obviously a more detailed analysis would be necessary before drawing a conclusive description of this phenomenon.

Quite surprisingly, the behaviour experimented when the nozzle is moved inward by 5 mm is not so different (Figure 1.23). Again, we have a basically unchanged on-design COP and a decreased critical condenser temperature. The decrease after point 3 is less steep and operation at point 4 would still be acceptable. Point 6, which still has a COP > 0.1, is now above 31°C. As a whole, the off-design behavior in this condition seems a bit less deteriorated than at NXP = 5 mm, but the difference is rather subtle when compared to the on-design condition.

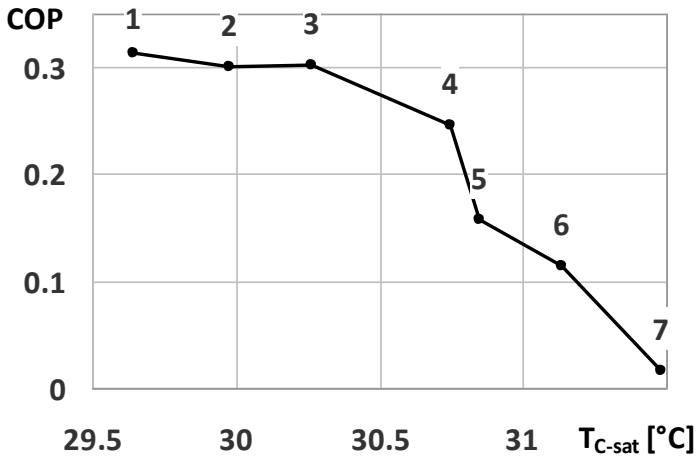

Figure 1.23 COP, $T_{E\text{-}sat}$ = 5°C and NXP = -5 mm

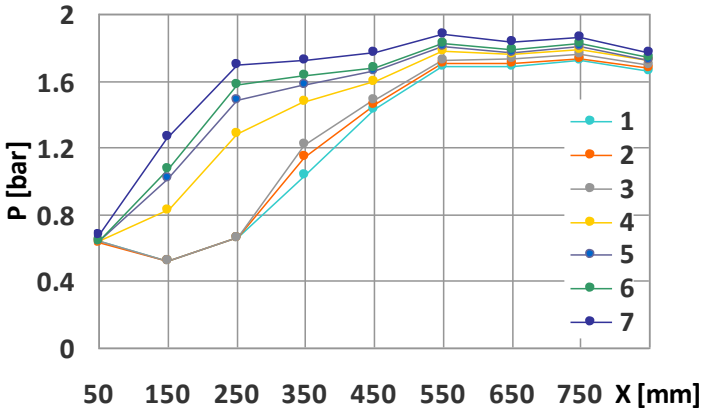

Figure 1.24 Static pressure at wall along the ejector, $T_{E\text{-}sat}$ = 5°C and NXP = -5 mm

1.5 Concluding Remarks

The CRMC ejector chiller working with R245fa has proved to be effective even at relatively low evaporation temperatures. The continuous profile offers higher efficiency and increased tolerance with respect to variations in operating conditions. For example, the bell-shaped inlet that smoothly connects the suction inlet to the CRMC profile allows an acceptable operation even when the primary nozzle is moved from the optimal position by significant amounts. On the other hand, an improved design should be sought for the ejector on the discharge side, where the straight cone does not give any contribution in terms of pressure recovery. If specifically designed, an ejector featuring an optimized, continuous profile could give an acceptable performance and superior flexibility when compared to other heat powered cycles.

The experimental activity will continue on the same prototype using R1233zd that has a low GWP replacement fluid and requires minor modifications to the chiller (Chapter 2).

2 Ejector cycle working with R1233zd

The experimental and numerical activity on R1233zd is described in this chapter. A part of the results shown in this chapter have been published in [33]. Another pair of articles, one experimental and one numerical, are in preparation.

2.1 Overview

The experimental results presented in this chapter have acquired with the same experimental setup described in detail in the first chapter.

The prototype has evacuated down to less than 50 Pa by Bigiesse 3PB2 vacuum pump after we made sure that R245fa was completely unloaded. System was recharged with the new refrigerant, R1233zd, by differential pressure between evacuated prototype and a warmed refrigerant cylinder.

Experimental data acquired in different generator and evaporator temperature give us an opportunity to analyse the system performance in different cases and try to reach the best system performance. Also, numerous CFD simulations were done in order to compare with experiments.

2.2 Working fluid, R1233zd

The refrigerant heavily affects the ejector performance, but nowadays it must above all comply with the regulations about its environmental impact. Many research works on ejector chillers in the recent past were carried out using refrigerants that have been or will soon be phased out [1]. Alternative, environmentally acceptable refrigerants are probably the most common

topic of discussion since the Montreal protocol has banned several high performance halocarbon refrigerants.

Milazzo and Rocchetti [34] compared several alternative fluids based on a thermodynamic ejector model accounting for real gas properties and adapting the ejector geometry to each gas by the CRMC criterion. Following the outcome of this study, we concentrated on R1233zd as a “dry expansion fluid” which has an inward slope of the upper limit curve on the temperature – entropy diagram. R1233zd, with 204.9 kJ/kg latent heat and 2.82 kg/m^3 vapour density, has similar thermodynamic properties to R245fa which was studied in [35] [36] [37] and proved to be very successful as a working fluid [25] [38]. R245fa is still investigated in the refrigeration systems by the researchers [39] [40] but we have to consider that R1233zd has very low GWP (at around 1) which put it in the fourth generation of refrigerants [41]. R1233zd was considered as a replacement for R245fa also in [42] [43] [44] [45].

2.3 Results and Discussion

2.3.1 Experimental

All saturation temperatures reported below are calculated from the pressure measured on top of each plate heat exchanger via NIST REFPROP functions [29]. The experiments presented herein are referred to saturation temperatures of 97°C and 103°C at generator. Chilled water temperature drop in the evaporator is kept on 5°C. Water temperature is at least 2.5°C higher than the evaporator saturation temperature throughout the test campaign (for instance, 7.5°C – 12.5°C chilled water for 5°C evaporation temperature). The higher water temperature avoids any risk of icing.

The four different performance curve at constant generator temperature in Figure 2.1 show the well-known behaviour of supersonic ejector chillers, featuring increasing COP and critical condenser temperature with increasing saturation temperature at

evaporator. In the case of higher generator temperature, it is notable that at high evaporator temperature the off-design condition takes place in a more gradual way, with relatively stable, though deteriorated, operation even at condenser temperature significantly above the critical value. At lower evaporator temperature the off-design lines are much steeper.

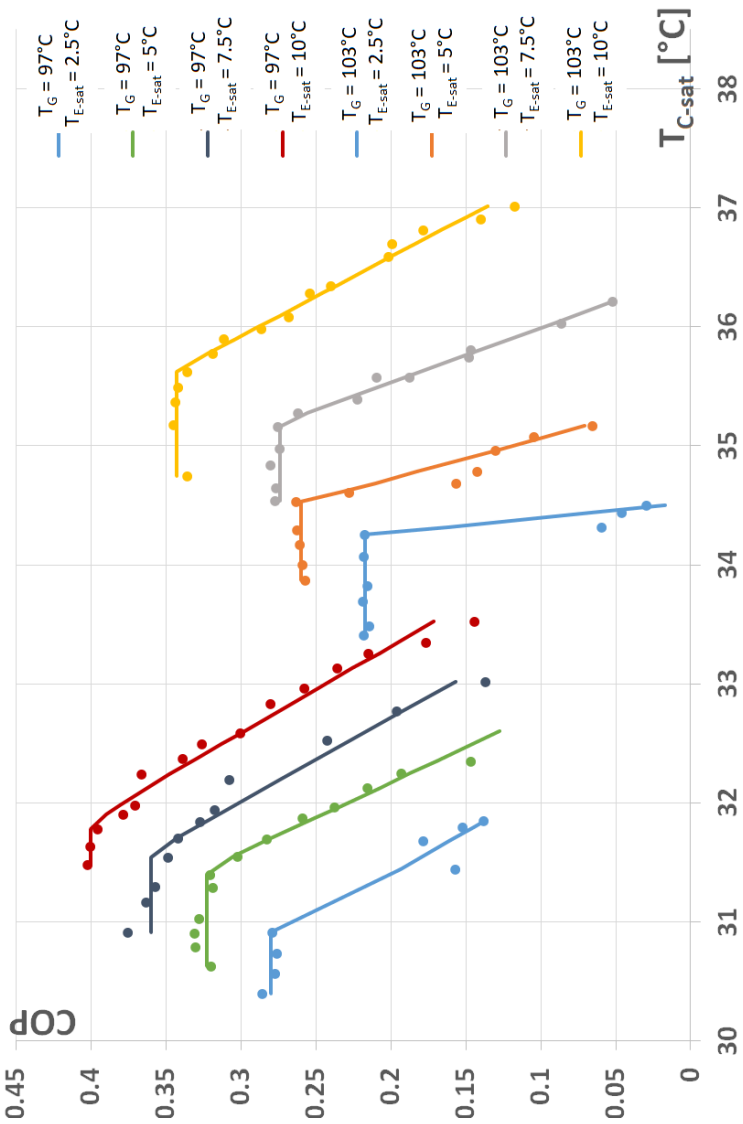

Figure 2.1 Experimental COP of the chiller in different conditions

A comparison of the system behavior for the two different generator temperatures in Figure 2.1, as usual shows higher COP and lower critical temperature for the low generator temperature. Lower amount of primary flow due to the lower generator temperature goes through the nozzle, while almost the same amount of secondary flow is entrained, so the COP and entrainment ratio are higher. On the other side, ejector critical back pressure is getting lower for decreasing generator temperature and make the ejector move to off-design at lower temperature.

A more detailed description of the ejector operation may be gathered from the observation of the pressure profile. The spacing between the transducers (100 mm – see Figure 1.11) does not allow a precise positioning of the shock train, but is sufficient to get a general picture and to discriminate between on and off-design working conditions[1]. For completeness, the readings of the pressure transducers at evaporator exit and at condenser inlet have been added as 0 mm and 1000 mm columns.

Two shapes are clearly distinguishable in the pressure profile along the ejector for the low evaporator saturation temperatures ($T_{E\text{-}sat}$ = 2.5°C). The curves from 1 to 4 in Figure 2.2 and 1 to 6 in Figure 2.3 all show a common pressure values until diffuser throat which is located around 300mm. Hence, sharp pressure rising between 250 and 350 mm in these curves obviously shows the transition between supersonic and subsonic flow. Further curves in these two figures show a completely different behavior, featuring a sharp pressure increases before 250 mm and then a slower increase before 550 mm, witnessing a fully off-design working condition.

On the other side, pressure profile at the lower evaporation temperature obviously gives a lower range of condenser temperature and consequently lower back pressure at ejector. This back pressure change cause difference outlet pressure at the ejector. I.e. ejector outlet pressure is around 1.6 bar at T_G = 97°C, $T_{E\text{-}sat}$ = 2.5°C (Figure 2.2), compare to T_G = 97°C, $T_{E\text{-}sat}$ = 10°C (Figure 2.3) that is almost 1.8 bar.

[1] The lines connecting the points are drawn only as a visual aid and do not give any indication about the pressure between the sensors.

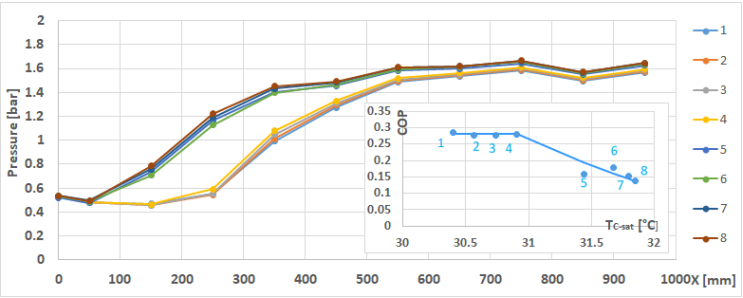

Figure 2.2 Pressure values along the ejector T_G = 97°C, $T_{E\text{-}sat}$ = 2.5°C

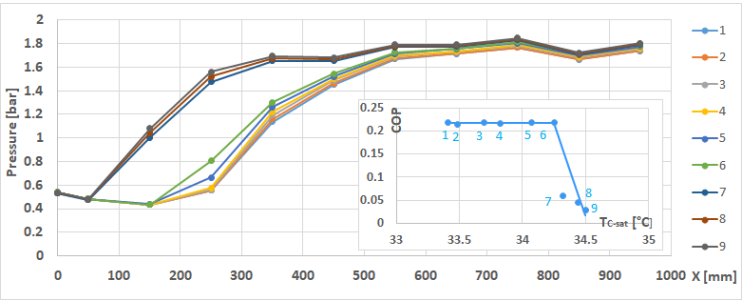

Figure 2.3 Pressure values along the ejector T_G = 103°C, $T_{E\text{-}sat}$ = 2.5°C

Figure 2.4 and Figure 2.5 referred to 10°C saturation temperature at evaporator in two different generator saturation temperature, show an almost continuous evolution of the pressure profile. Apparently, the first group of lines still have almost coincident pressures up to the second transducer. However, the other lines are equally distributed between the on-design profile and the extreme working condition (lines 15 in Figure 2.4 and line 16 in Figure 2.5) when the chiller does not produce significant cooling and the experiment is stopped in order to avoid backflow from the condenser to the evaporator.

Ejector outlet pressure can be compared at the different generator temperatures, also. Ejector outlet pressure in T_G=103°C is always higher than T_G= 97°C which shows dependency of the

ejector back pressure on the generator temperature more than evaporator temperature.

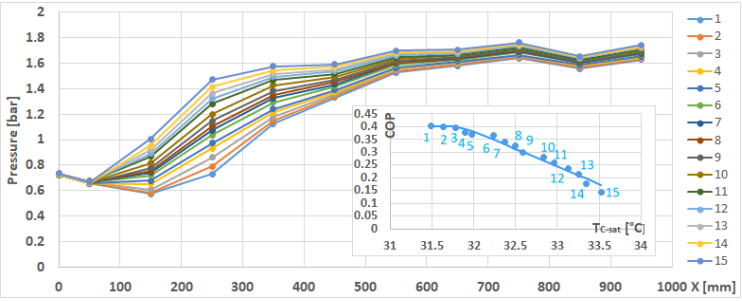

Figure 2.4 Pressure values along the ejector T_G = 97°C, $T_{E\text{-}sat}$ = 10°C

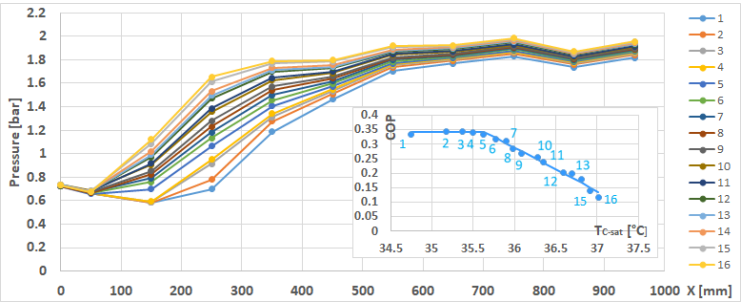

Figure 2.5 Pressure values along the ejector TG = 103°C, TE-sat = 10°C

In any case the pressure recovery after 550 mm is null or even negative and also, a remarkable pressure reduction occurs between 800 mm to 900 mm. As anticipated, this is probably due to a poor design of the last part of the ejector and/or to a flow recirculation. Another point which would deserve an improvement is the connection between evaporator exit and the ejector inlet. The pressure loss between evaporator exit (0 mm), which is in the close vicinity of the evaporator, and the measurement close to the diffuser inlet (50 mm) is due to a rather long path between these points, including two elbows and the “T” connection between secondary and primary flow lines.

The intermediate conditions, $T_{E\text{-}sat}$ = 5°C and $T_{E\text{-}sat}$ = 7.5°C, in both generator temperature conditions place themselves in between the two behaviours which are showing in Figure 2.6, Figure 2.7, Figure 2.8 and Figure 2.9

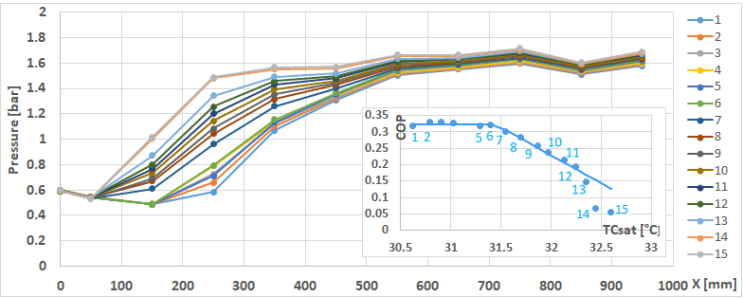

Figure 2.6 Pressure values along the ejector T_G = 97°C, $T_{E\text{-}sat}$ = 5°C

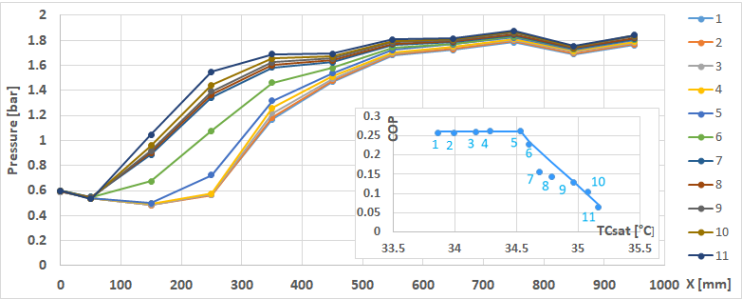

Figure 2.7 Pressure values along the ejector T_G = 103°C, $T_{E\text{-}sat}$ = 5°C

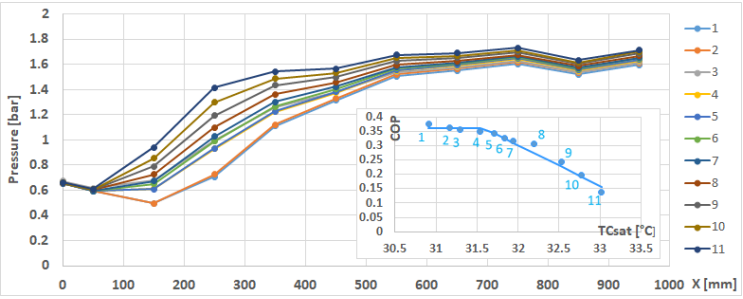

Figure 2.8 Pressure values along the ejector T_G = 97°C, $T_{E\text{-}sat}$ = 7.5°C

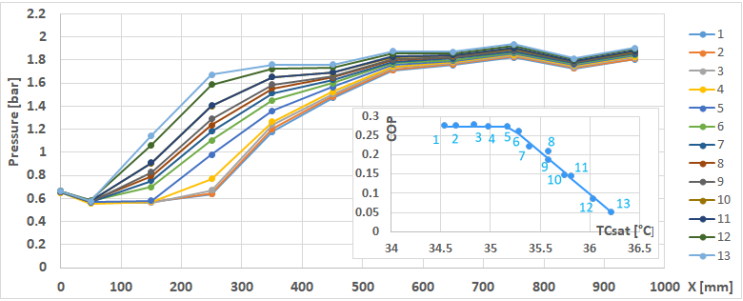

Figure 2.9 Pressure values along the ejector T_G = 103°C, $T_{E\text{-}sat}$ = 7.5°C

Figure 2.10 summaries the ejector performance curve by showing the critical state at four different evaporator temperatures and two generator temperatures and their effect on the ER of the system. The fundamental explanation of this graph is described at the introduction in detail (check Figure 4).

Each point in the graph represent the ER and condenser temperature at the critical state. Hence, it is clear that system performance improved by increasing the evaporator temperature due to the higher pressure at suction inlet that is cause higher secondary mass flux. ER increased over 10% and critical temperature at around 0.25°C by rising evaporator saturation temperature for 2.5°C.

On the other hand, raising generator temperature has both negative and positive effect on the ejector performance. The system reached the critical temperature with delay of 3°C but with decreasing ER when generator temperature raised by 6°C. If the generator temperature could be varied during operation, one would be able to use it as a control variable for the cooling system, giving priority to ER or critical temperature at will.

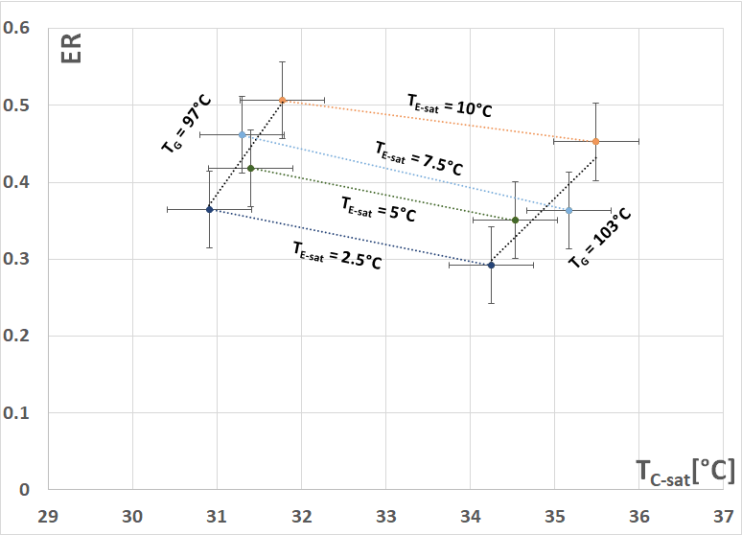

Figure 2.10 Experimental ejector operating performance curve

2.3.2 Computational Analysis

2.3.2.1 Numerical Modelling

CFD modelling of the ejector has a relatively short history. The review paper by Matsuo et al. (1999) [46] cited pioneering papers modelling shock trains like Carrol et al. (1993) [47] and Yamane et al. (1995) [48], although these works were not specific to ejector applications [49]. Sun and Eames [50] established a state of the art of the theoretical designs and studies of supersonic ejectors, besides providing an overview of their experimental application. The authors discussed mathematical modeling concepts for design, based on the thermodynamic approach.

Ejector computational investigations gathered more importance in the last decade, thanks to improved computational resources and the advent of advanced CFD software. Authors have focused their studies on the analysis of several numerical aspects among which turbulence models and 2D–3D approximations had a central role.

Pianthong et al. [17] showed that there is no remarkable difference in wall pressure distribution along the ejector between the 2D and 3D approximation. Mazzeli et al. [51] found good agreement for an air-operated ejector, across all 2D and 3D models at on-design conditions. Automatically adapted grids has also been explored in many research articles [52] [53] [54] in order to find a compromise between simulation accuracy and computational cost.

In terms of turbulence modelling selection, Bartosiewicz et al. [55] [56] made a deep study to examine the effect of turbulence model by studying six models, (*k*ε, *k*ε-RNG-, *k*ε-Realizable, RSM, *k*ω, *k*ω-SST) applied to an air supersonic ejector. He proved that *k*ε-RNG and *k*ω-SST are the best in predicting pressure variations while the *k*ω-SST model was better in predicting the mixing length of the motive jet. Following this work, he used the same turbulence models to evaluate the ER with R142b and found large prediction differences, especially in off-design operations [57]. Further works focusing on ejector operating with environmentally friendly fluids [58] [51] [59] under different conditions found that the *k*ε and *k*ω-SST gave the best performance with respect to other models [60].

In the present work, simulations are performed using the commercial CFD package ANSYS FLUENT v19.2 that is based on a finite volume approach. The numerical model is based on the standard Navier-Stokes equations for compressible flows. Spatial discretization of both the conservation and turbulence equations is third order accurate using the MUSCL scheme. Due to the high Mach numbers in the flow field, a density-based implicit solver is used [61]. Convergence of the solution is defined by an error in the mass flow imbalance of less than 10^{-5} kg s^{-1} and calculations are stopped when all residuals are stable. Bound-

ary conditions are provided as total pressure and static temperatures at inlets, static pressure at outlet. Walls are assumed to be adiabatic.

Based on successful implementations reported in the literature [62], [55] and [56], kω SST turbulence model is selected for all simulations. The grid is designed to have y+ values always less than 1 along the supersonic diffuser wall, where strong pressure gradients occur due to high back pressure and the presence of shocks.

Figure 2.11 shows the numerical grid together with detail in the proximity of the primary nozzle trailing edge and primary nozzle throat.

Grid dependence was checked in [25] by comparing the results Figure 2.11of three grids with approximately 40 000, 80 000 and 150 000 cells. The analysis showed that the 80 000 cells is the best trade-off in terms of accuracy and computational cost and the maximum error in the prediction of the mass flow rate was less than 0.1% with respect to the finest grid.

All calculations are performed by accounting for real gas properties of the refrigerant using a 3rd order algebraic Peng-Robinson equation of state (EOS).

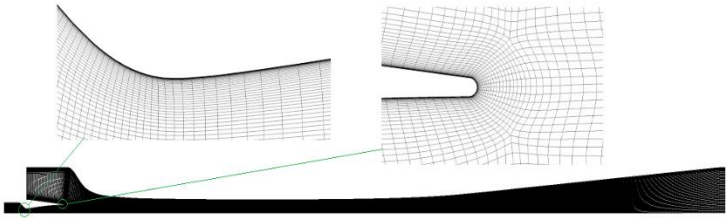

Figure 2.11 Numerical grid in the diffuser with the proximity of the primary nozzle trailing edge and primary nozzle

2.3.2.2 CFD Simulation

For clarity, Figure 2.12 reports again the experimental supersonic ejector performance curve at constant generator temperature. The highest evaporator temperature ($T_{E\text{-}sat}$ = 10°C) which has the maximum COP at around 0.35 and critical temperature over 35.5°C was chosen as the reference working condition for the setup of the CFD scheme. This choice was made because the experiments were most stable in this condition. Partly, this may be due to the fact that the off-design trend is less steep with respect to other curves, which makes this condition less prone to instabilities and more appealing for the setup of the CFD.

The setup of the CFD scheme was done by analyzing different computational models and comparing them against the selected experimental curve. The best model was then maintained for comparison with other experimental results.

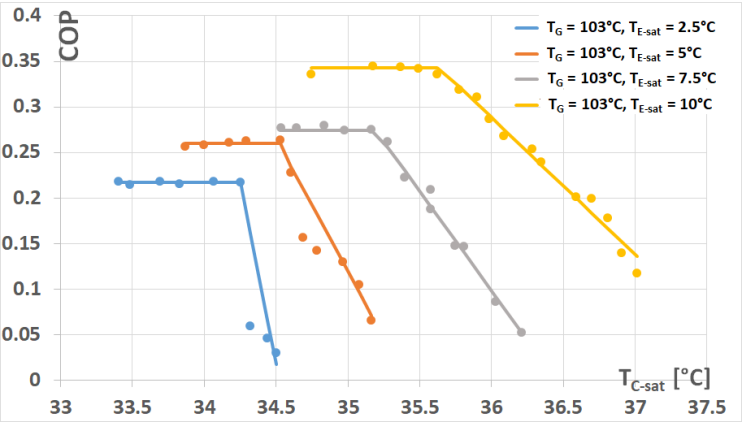

Figure 2.12 Experimental COP of the chiller in different conditions

Figure 2.13 shows the comparison between experimental ER and mass flow rates and the corresponding CFD values calculated with different turbulence models and wall roughness.

The differences in the predicted entrainment ratios is around 15% at on design conditions. Clearly, all the numerical models show the same trend and differences between various models and roughness heights are negligible in on-design (choked) conditions.

On the other hand, the bottom graph shows that the error appears much lower when the mass flow rates are compared separately and they reach average values of 5.7% and 7.3% for the primary and secondary mass flow rate respectively. This effect is due to a compensation of the error caused by the fact that CFD underestimates the primary flow rate while, at the same time, it overestimates the secondary mass flow rate.

As the condenser pressure increases, higher values of friction cause the critical state to appear in advance. This result is indeed expected, as greater friction translates into larger amounts of total pressure losses, thus reducing the capability of the mixed flow to withstand high values of back pressure. On the contrary, in the case of smooth surfaces ($k\varepsilon$-Realizable), the simulated ejector maintains choked conditions for higher temperature at the condenser. This analysis highlights the importance of the manufacturing process on the performance of a supersonic ejector refrigerator, as smoother surfaces implies achieving larger values of critical pressures.

Although the numerical transition to off-design seems steeper than the experiments for any of the CFD models, nevertheless it appears that the $k\omega$-SST method with wall roughness 40μ more closely reproduces the experimental data (this is in line with the finding of [25] which showed that roughness could lie somewhere between 40 and 20 microns). At roughness height of 60μ the transition appears earlier than experiments and the range of “non-choked” operations becomes larger. On the other hand, a lower level of roughness yields a higher critical pressure than the experimental one. Therefore, the 40μ roughness is selected for all subsequent calculations.

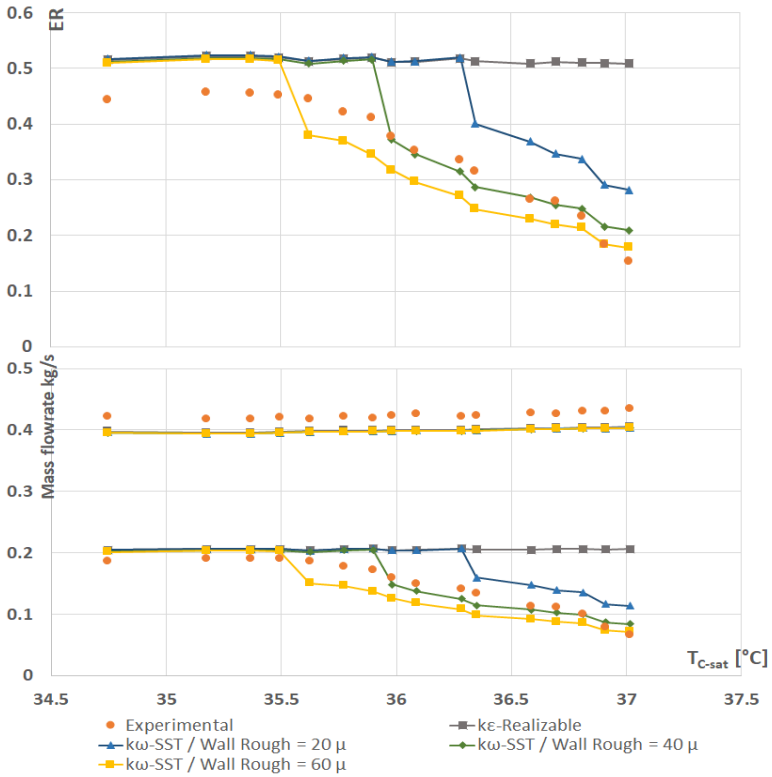

Figure 2.13 Experimental/numerical comparison Entrainment Ratio (top), and ejector primary (upper curve of bottom graph) and secondary (lower curve of bottom graph) mass flow rate for different values of simulated wall roughness; T_G = 103°C, $T_{E\text{-}sat}$ = 10°C

Figure 2.14 shows the comparison of the selected computational model (*k*ω-SST, wall roughness = 40μ) with all the experimental curves presented in Figure 2.12. As the evaporator temperature is decreased, the computed condenser critical temperature is getting farther from the experimental one and it reaches a difference greater than1°C (for $T_{E\text{-}sat}$ = 2.5°C and $T_{E\text{-}sat}$ = 5°C).

For higher saturation temperatures, the computational trends show a sharper drop at the critical state with respect to experiments. At lower temperatures both the numerical and experimental results show a steeper transition to off-design.

Such rapid transition to off-design reminds of the typical behavior of supersonic wind tunnel applications, which are characterized by the presence of hysteresis phenomena related to the start-up issue. The presence of hysteresis could also explain the large error in the critical pressure at low evaporation temperature. Therefore, additional analysis were carried out in this regard, which are presented in the following section.

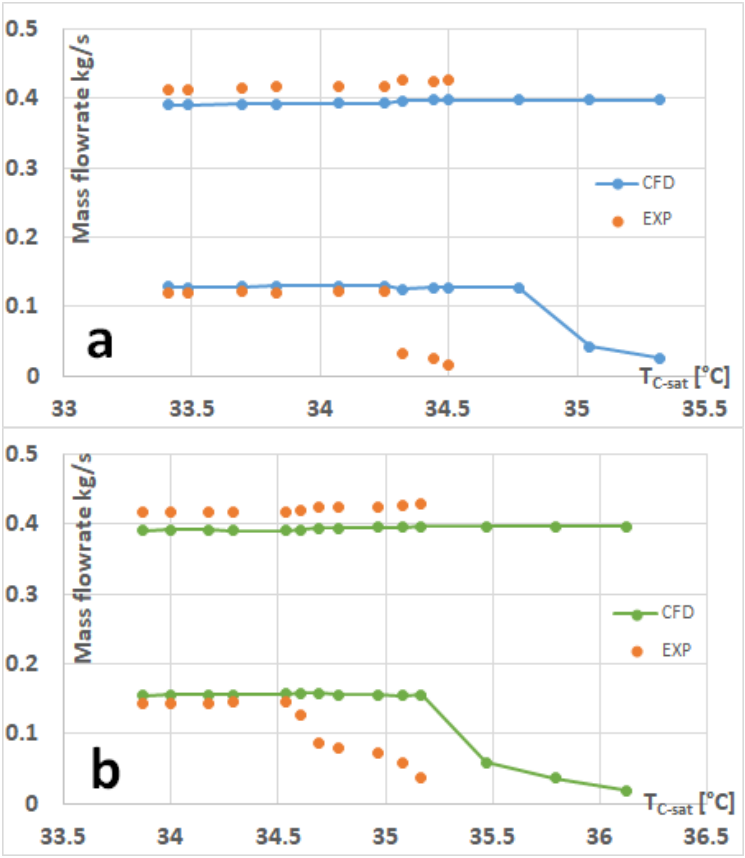

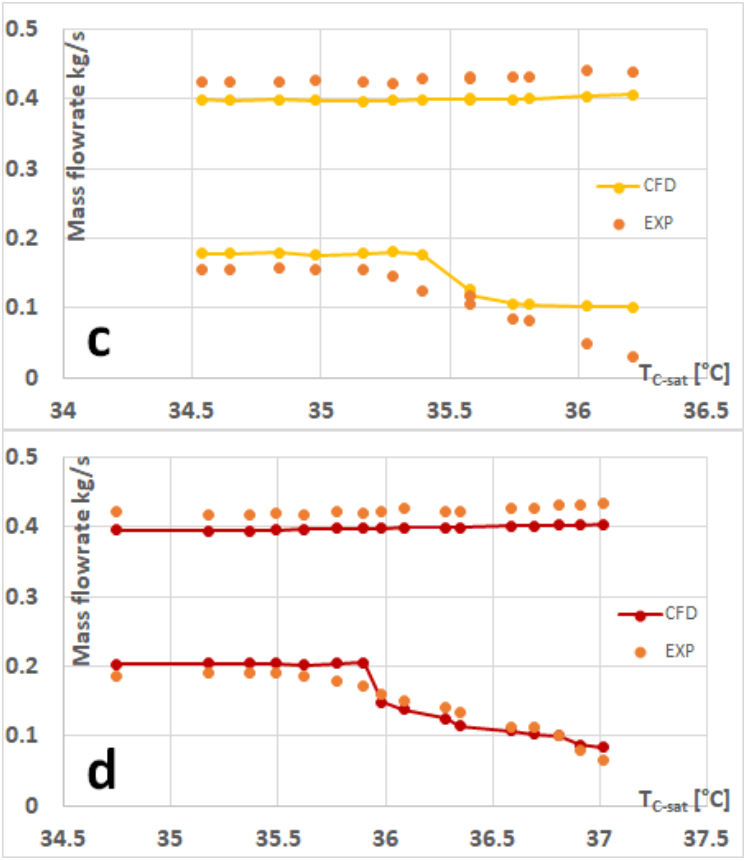

Figure 2.14 Experimental/numerical comparison of ejector primary (upper curve) and secondary (lower curve) mass flow rate at T_G = 103°C, (a) $T_{E\text{-}sat}$ = 2.5°C, (b) $T_{E\text{-}sat}$ = 5°C, (c) $TE_{\text{-}sat}$ = 7.5°C, (d) $T_{E\text{-}sat}$ = 10°C

2.3.2.3 Hysteresis in the CFD Simulations

Figure 2.15 Figure 2.15 Experimental/numerical (hysteresis) comparison of ejector secondary mass flow rate at TG = 103°C, (a) TE-sat = 2.5°C, (b) TE-sat = 5°C, (c) TE-sat = 7.5°C, (d) TE-sat = 10°Cshows the comparison amongst experimental data

and CFD results obtained by “moving forward and backward” along the performance curve. Stated differently, the curve labelled “CFD forward” in Figure 2.15 was obtained by initializing each CFD simulation from the solution at its left (with lower condenser pressure). Conversely, the “CFD backward” curve was obtained starting the simulations from off-design conditions and progressively increasing the condenser pressure.

Figure 2.15 shows clearly that, the critical temperature is anticipated in the backward results and creates a gap with the “CFD forward” curve, i.e., the ejector presents hysteresis with respect to the outlet pressure changes.

This hysteresis appears to be more significant at lower evaporator temperatures. At 2.5°C evaporation temperature, the difference in the critical pressure between the “CFD backward” and “CFD forward” curves is greater than 15000 Pa (around 1°C in condenser temperature). Moreover, the return to on-design conditions appears to be more gradual than the transition toward off-design conditions (i.e., the forward curve is steeper).
In general, numerical results obtained moving backward appear to more closely reproduce experimental data. This is especially true at higher evaporator temperatures, where both the steepness and starting position of the off-design curve is well reproduced by the backward cases. Conversely, at 2.5°C evaporation temperature, the experimental data predict a critical pressure which is between the values of the forward and backward curves. However, the very sudden collapse of the experimental ER appears to be in closer agreement with the forward curve. The error in critical temperature in this case is around 0.5 °C.

It should be noted, that experimental tests were generally carried out starting from on-design conditions and progressively increasing the condenser pressure (i.e., moving forward). However, as the system moved closer to the critical state, the oscillation in the pressure and generator power caused the system to jump between on- and off-design before becoming stable. This may have caused an earlier transition to off-design than that predicted by CFD (which is not subject to experimental noise and oscillation). This fluctuation between chocked and

non-chocked diffuser may be the main reason of the experimental agreement with “CFD backward” results.

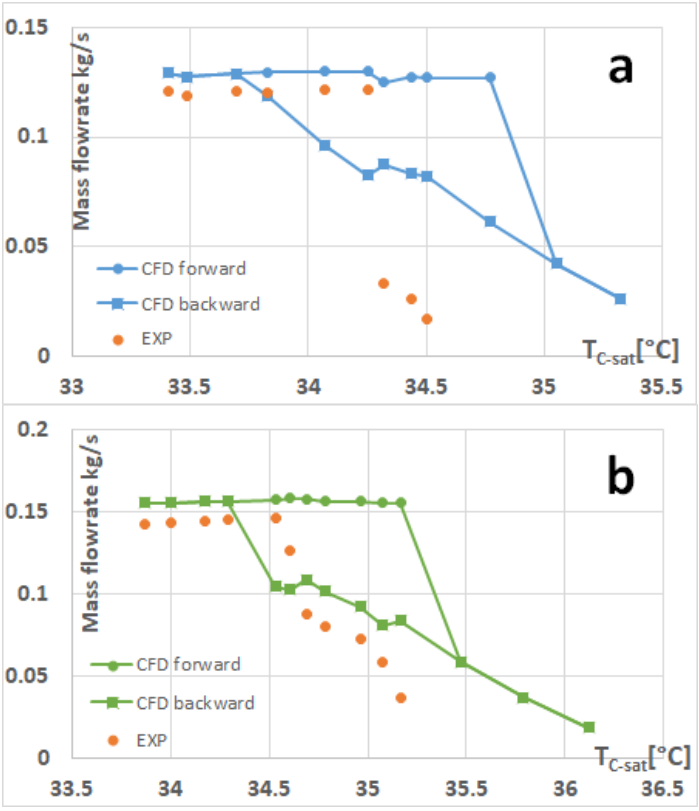

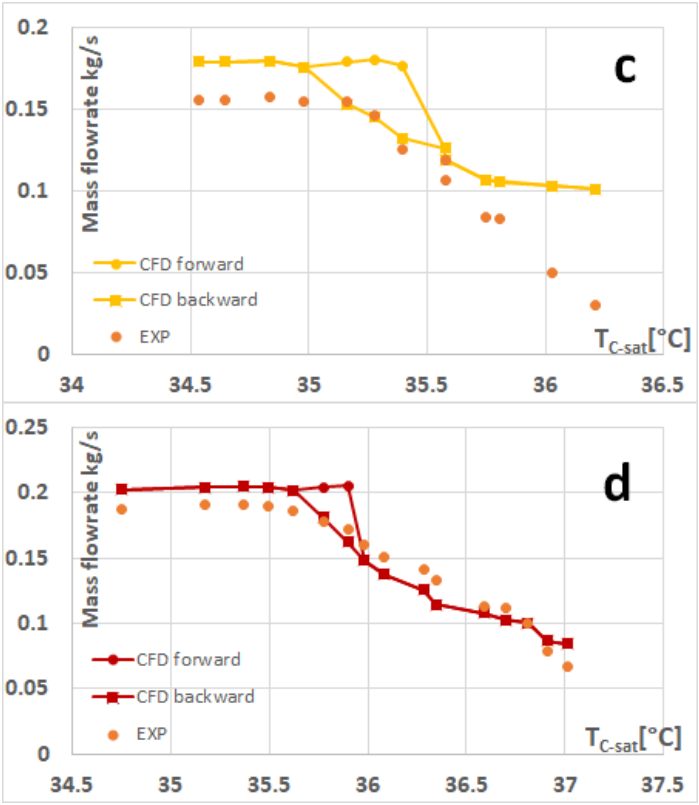

Figure 2.15 Experimental/numerical (hysteresis) comparison of ejector secondary mass flow rate at T_G = 103°C, (a) $T_{E\text{-}sat}$ = 2.5°C, (b) $T_{E\text{-}sat}$ = 5°C, (c) $T_{E\text{-}sat}$ = 7.5°C, (d) $T_{E\text{-}sat}$ = 10°C

It is interesting to analyze the flow behavior in the ejector for both the numerical forward and backward cases in more details.

Figure 2.16 compares the Mach field between the forward and backward cases for $T_{E\text{-}sat}$ = 10°C. In particular, points a/a' to d/d' presents the same Mach field for both the forward and backward cases. On the contrary, points b and c represent the Mach field for the numerical forward curve, which still display the diffuser in chocked (on-design) working conditions. On the other side, points c' and d' in the backward curve shows a remarkable

difference to their respective points in the forward curve, points c and d. In these cases the ejector operates in non-chocked or off-design regime.

This behavior is also visible for the case with $T_{E\text{-}sat}$ = 2.5°C illustrated in Figure 2.17. The figure presents the supersonic Mach field together with regions of negative axial velocities (these are indicative of recirculation regions). Points b', c' and d' are showing off-design condition in the backward simulations, whereas b, c and d illustrate the same boundary conditions in the forward numerical simulations, which are still at on-design.

Another reason for the different results between forward and backward simulations can be the rise of the flow recirculation that is visible in the low evaporator temperature case (Figure 2.17). In this case, the raising of condenser pressure in the backward curve creates a recirculation in the convergent area which may partly explain the larger differences between backward and forward simulation. This recirculation is clearly evident at state c' and d'. At point e/e', the flow behavior is the same for both backward and forward numerical simulations, and both show a strong recirculation in non-chocked conditions.

Recirculations cannot be the main reason of the appearance of hysteresis, as they are not visible in the high evaporator saturation temperature (see Figure 2.16). However, they may be responsible for the hysteresis becoming more persistent and longer when the evaporation temperature is lower.

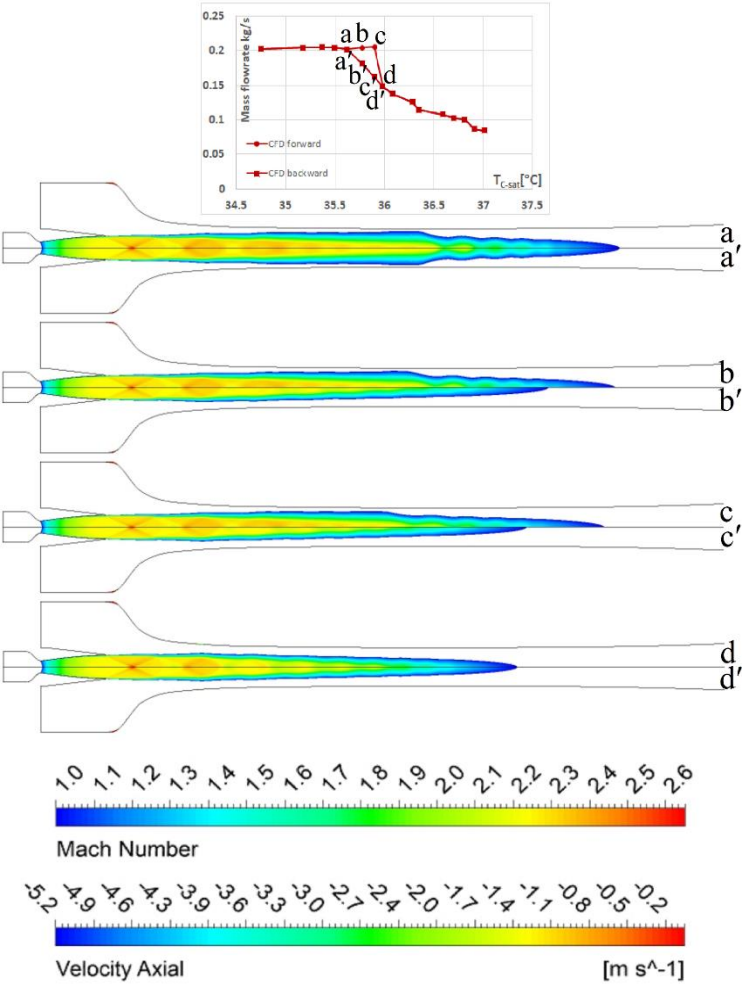

Figure 2.16 Supersonic Mach filed and static pressure (recirculation) along the diffuser T_G = 103°C, $T_{E\text{-}sat}$ = 10°C for CFD forward (above the axis) and CFD backward (below the axis)

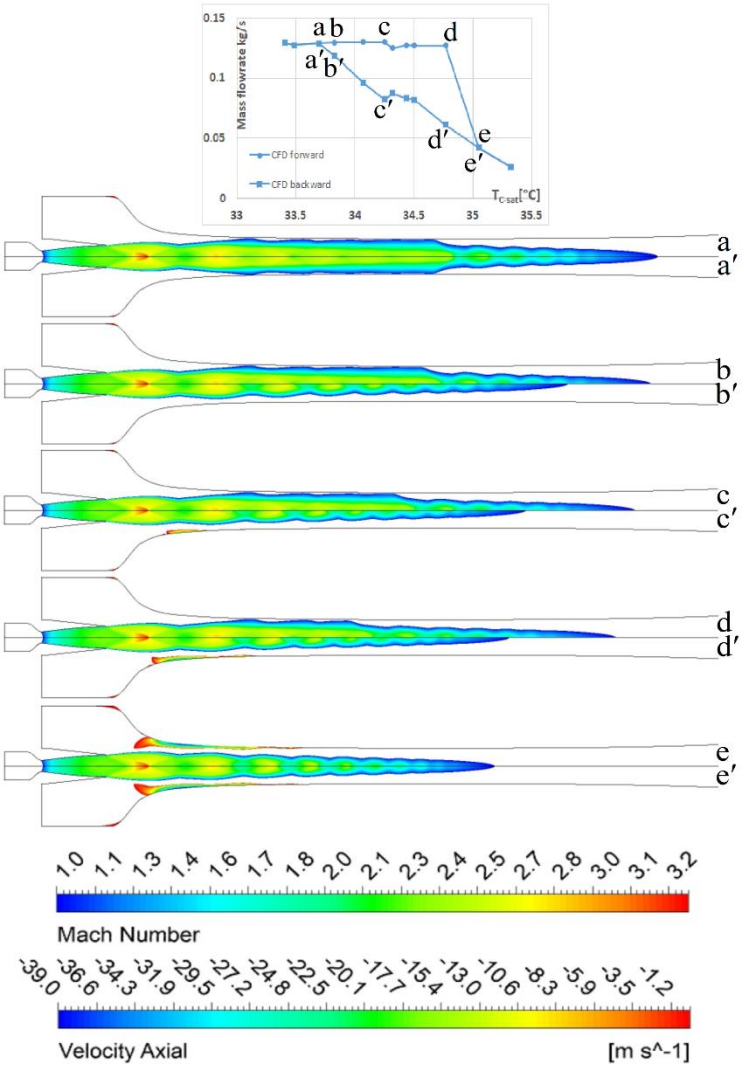

Figure 2.17 Supersonic Mach filed and static pressure (recirculation) along the diffuser T_G = 103°C, $T_{E\text{-}sat}$ = 2.5°C for CFD forward (above the axis) and CFD backward (below the axis)

2.3.2.4 Pressure Profile

Figure 2.18 shows the comparison between the static pressures measured along the diffuser wall and the corresponding profiles obtained by CFD (kω-SST, wall roughness = 40μ) at T_G = 103°C and $T_{E\text{-}sat}$ = 10°C. In all the graphs, the diffuser throat is located at around 272 mm on the axial direction, between the 4th and 5th pressure transducer.

The first graph of Figure 2.18 shows that the forward and backward simulations are completely overlapping. Pressure fluctuations due to shock diamonds pattern appears before the throat. The sharp rise at around 350 mm from the inlet is indicative of the transition between supersonic and sonic flow. The second graph shows almost the same behavior of the first, with a slightly smoother pressure rise that indicates that the shock has moved closer to the diffuser throat (i.e., at lower mach numbers). In terms of experimental data, this graph illustrate that the pressure measured by the 4th pressure probe (located at 250 mm) is increased. This pressure increase before the throat may indicate that the ejector is not in choked conditions, at least for experimental data. Nevertheless, the ejector can still work with a performance that is almost as good as that at on-design. This smooth transition makes difficult to understand the jump between chocked and non-chocked diffuser during the experimental test. On the other hand, this behavior is beneficial as the ejector can operate with high performance and in a stable manner even after the inception of off-design conditions.

By contrast, the numerical results are still predicting on-design behavior, but the agreement with experiments is still substantial, because the ejector is close to the critical conditions.
The on-design conditions are maintained in the third and fourth graphs for the CFD forward results, with a slight retraction of the position and strength of the pressure growth. On the other hand, the numerical backward result presents a completely different pressure profile, with the pressure increment located between 50 – 100 mm from the inlet, which indicates the completed transition to off-design.

The experimental pressure profile fall in the middle of numerical pressure profiles. This indicates that while the forward curve underestimate the value of the critical pressure, the backward curve may predict a too early transition to off-design.

Figure 2.19 shows the same pressure trend for $T_{E\text{-}sat}$ = 2.5°C. For this case, the agreement with CFD decrease both for the forward and backward curves. In particular, the backward curve anticipates the critical point, whereas the forward curve shows a delay in the transition to off-design. At the highest outlet pressure, the forward curve is still in choked conditions, while the backward curve appears to delay the pressure rise with respect to experiments.

These errors, may be caused by the flow recirculation that appears in the CFD simulation at $T_{E\text{-}sat}$ = 2.5°C. Such recirculations are very difficult to predict by steady RANS simulations and their extent may be significantly different from those existing in the real ejector flow. Therefore, it is expected that a lower agreement occur at lower evaporation temperatures.

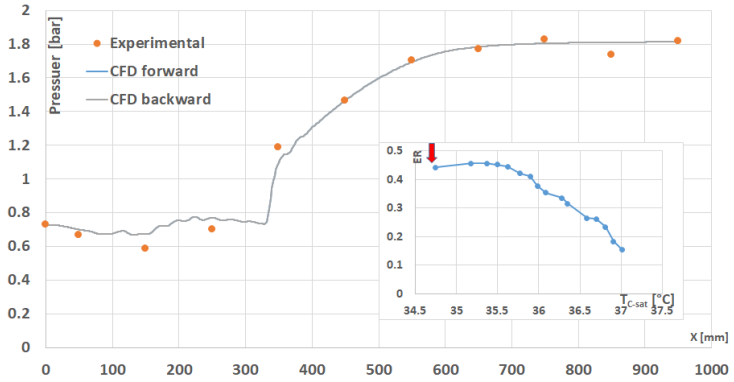
Pressuer [bar]
Experimental
CFD forward
CFD backward
ER
$T_{C\text{-}sat}$ [°C]
X [mm]

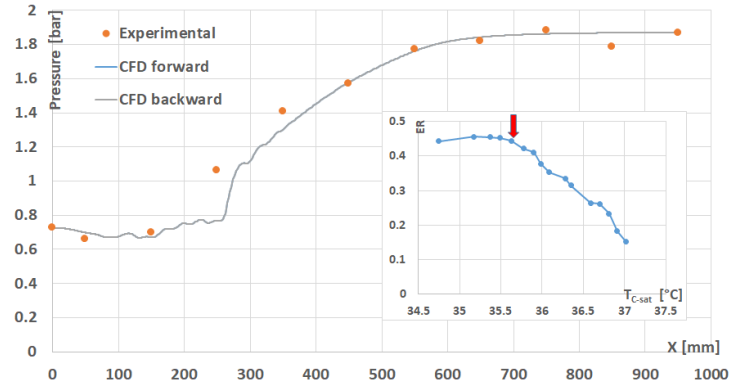
Pressure [bar]
Experimental
CFD forward
CFD backward
ER
$T_{C\text{-}sat}$ [°C]
X [mm]

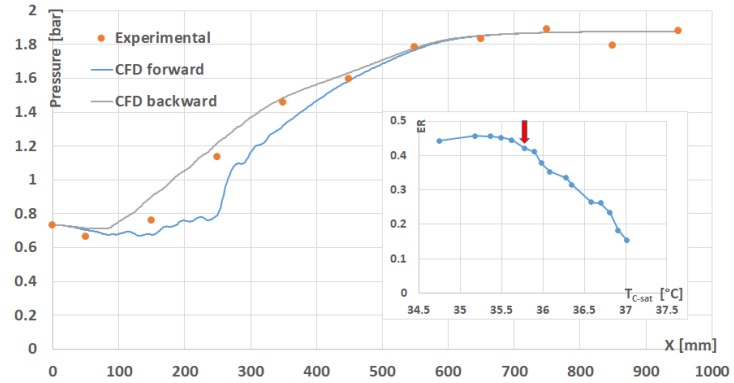
Pressure [bar]
Experimental
CFD forward
CFD backward
ER
$T_{C\text{-}sat}$ [°C]
X [mm]

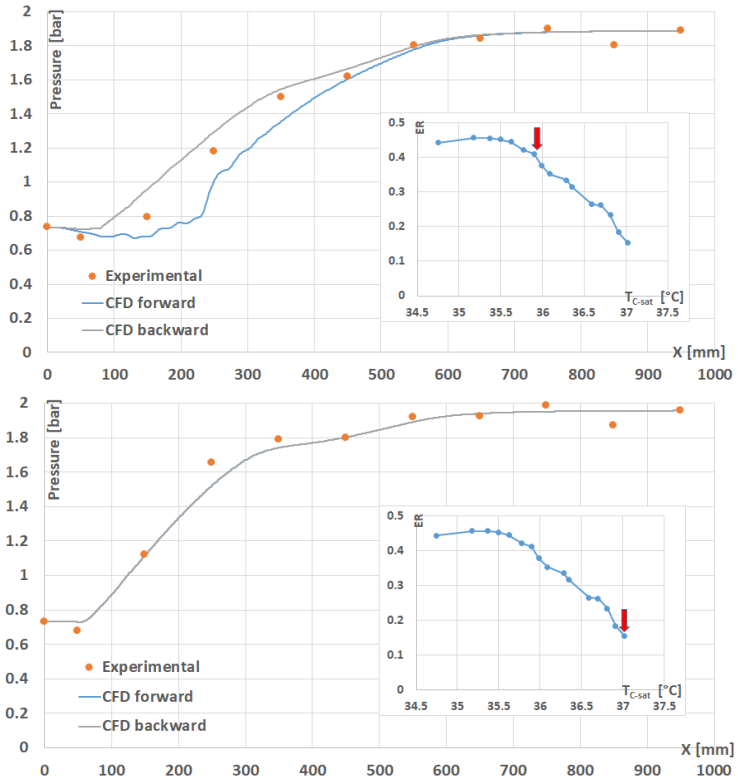

Figure 2.18 Experimental/numerical comparison of ejector pressure profile at T_G = 103°C, $T_{E\text{-}sat}$ = 10°C

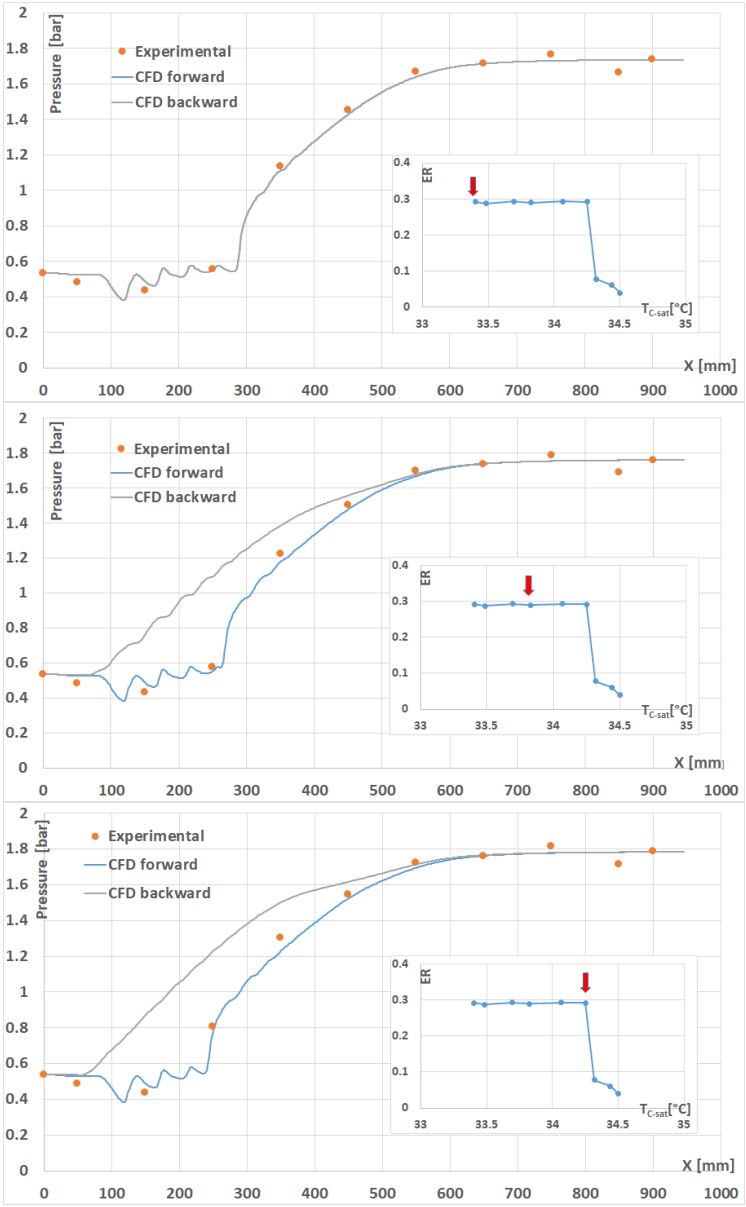
Pressure [bar]
Experimental
CFD forward
CFD backward
ER
$T_{C\text{-}sat}$[°C]
X [mm]

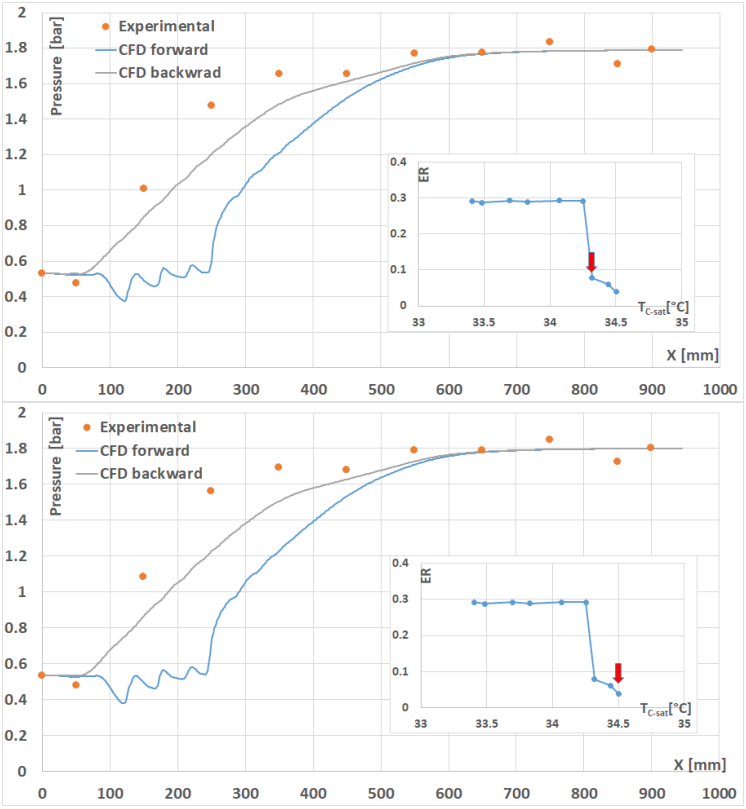

Figure 2.19 Experimental/numerical comparison of ejector pressure profile at T_G = 103°C, $T_{E\text{-}sat}$ = 2.5°C

2.3.2.5 Ejector Analysis

Finally, the CFD results were post-processed in order to understand details of the ejector internal flow field. The analysis is made at varying evaporator temperature, whereas the condenser and generator temperatures are kept constant. The green curve in Figure 2.20 illustrates the simulated points considered for this analysis. The dashed lines in Figure 2.20 shows that we

followed the on-design curve of each case to reach the back pressure of the lowest evaporator temperature ($T_{E\text{-}sat}$ = 2.5°C).

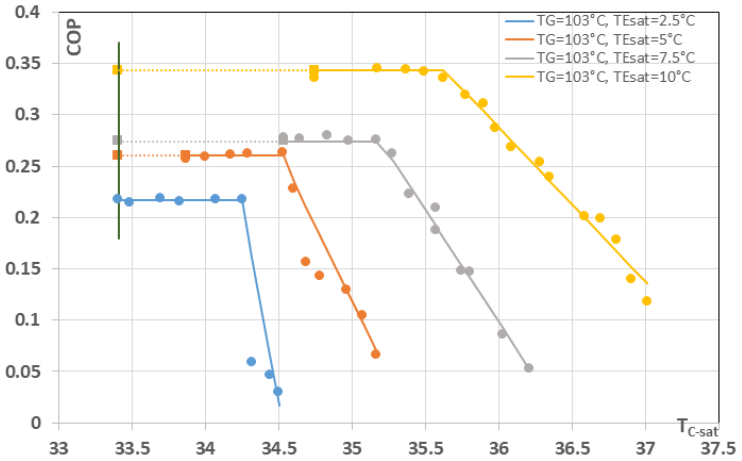

Figure 2.20 Experimental COP of the chiller in different condition with same back pressure (vertical line)

Figure 2.21 shows supersonic Mach field and static pressure along the diffuser for these cases. Clearly, the values of Mach number increase with decreasing the evaporator temperature. Accordingly, the pressure oscillations are greater, indicating that stronger shocks and expansion waves are taking place at lower evaporator temperature. Conversely, at $T_{E\text{-}sat}$ = 10°C, (d) the sonic line appears to be smoother, the pressure fluctuations are reduced and shocks and expansion waves are barely visible. This information tells us that the primary nozzle is correctly expanded when the pressure of the mixing chamber is close to the saturation pressure at 10°C. When decreasing such pressure, the primary nozzle becomes over-expanded, giving rise to strong shocks and expansion waves that take the familiar diamond pattern. Moreover, the advancement of the diffuser shock at higher evaporator temperature is caused by the higher energy content of the suction flow as well as the lower viscous dissipation when the primary nozzle is correctly expanded.

In conclusion, this analysis allows us to understand the best operating conditions for the primary nozzle and ejector in general, by providing information on how the flow is expanding, where it shocks and dissipate energy due to a non-optimal design.

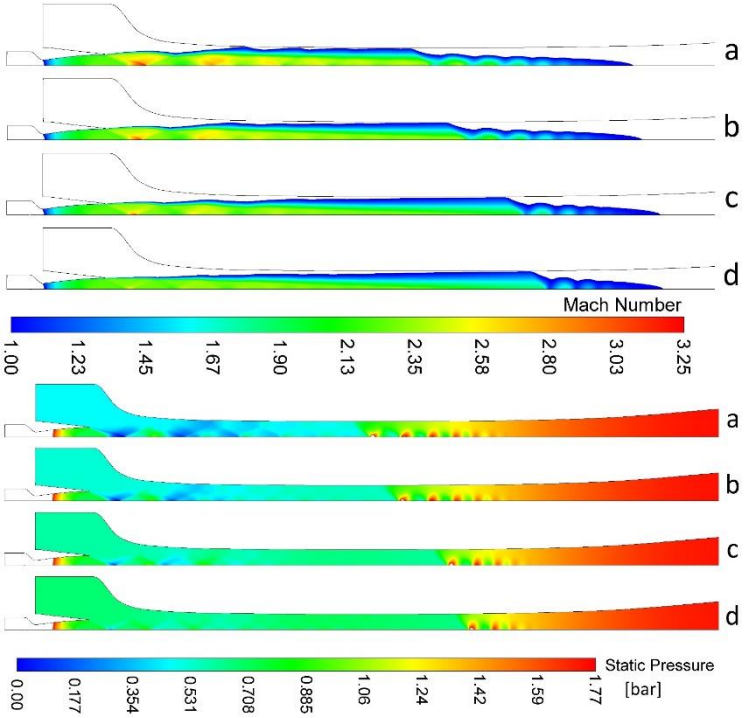

Figure 2.21 Supersonic Mach field (up) and static pressure (bottom) along the diffuser for different evaporator saturation temperature and same back pressure, T_G = 103°C, (a) $T_{E\text{-}sat}$ = 2.5°C, (b) $T_{E\text{-}sat}$ = 5°C, (c) $T_{E\text{-}sat}$ = 7.5°C, (d) $T_{E\text{-}sat}$ = 10°C

2.4 Concluding Remarks

This chapter presented experimental and numerical results on a supersonic ejector chiller working with R1233zd as a refrigerant.

Results are obtained for operating condition which are typical in air conditioning and waste-heat recovery applications (Generator: 97°C and 103°C, Evaporator: from 2.5°C to 10°C). An extensive numerical campaign was performed which resulted in reasonably close agreement with experimental data both in terms of global and local parameters.

The main result of this chapter can be summarized as follows:

- The satisfactory results obtained by our CRMC ejector chiller with R245fa can be replicated with the low-GWP, drop-in substitute R1233zd.
- High compression ratio has been preferred to high entrainment ratio (i.e. high COP) in order to enlarge the system potential market.
- The performance given by the two refrigerants is substantially aligned.
- A significant amount of work is still needed in order to optimize the chiller, i.e. increase its performance and reduce its cost.
- The ejector design offers a large space for improvement, e.g. the shape of the conical part on the exit side, which should be optimized by a CFD analysis.
- Wall surface roughness should be kept to a minimum,
- Wall heat exchange should be analysed and integrated in the ejector optimization.
- Ejector chillers can be useful as a low cost alternative for LiBr absorption chillers.
- Synthetic refrigerants may reach sub-zero temperatures and have high volumetric cooling capacity
- These pros must suffice to counterbalance the higher cost of the refrigerant.
- The environmental safety of the R1233zd needs to be proved on the long term.

In terms of numerical analysis, the following results can be understood from our analyses:

- Good agreement between experimental and numerical data can be achieved when the wall roughness is correctly evaluated
- Wall roughness has not significantly influence on the ER at chocked (on-design) condition but friction losses have a large impact on the onset of the non-chocked (off-design) regime, thus reducing the critical pressure
- The CFD results show hysteresis when simulating the performance curve in forward or backward direction with respect to the condenser pressure. This behavior is typical of supersonic wind tunnel application and it's related to the startup issue
- The hysteresis appears to be more significant at lower evaporator temperatures
- The presence of hysteresis can partly explain the large error in the critical pressure. In particular, the experimental results seem to be in closer agreement with the "CFD backward" curve.
- Experimental fluctuation between chocked and non-chocked diffuser may be the main reason of the experimental agreement with "CFD backward" results
- The appearance of rcirculation in CFD results may be responsible for the hysteresis becoming more persistent and longer when the evaporation temperature is lower
- The experimental pressure profiles fall in the middle of numerical pressure profiles, (numerical forward curve underestimate the value of the critical pressure and numerical backward curve may predict a too early transition to off-design)

References

[1] A. Trott and T. Welch, Refrigeration and air conditioning, Reed educational and professional publishinh Ltd, 2000.

[2] E. Groll, "Ejector technology," *Internationak journal of refrigeration,* vol. 34, no. 7, pp. 1543-1544, 2011.

[3] G. Flügel, "the design of jet pump," *NACA technical momerandum,* vol. 982, 1941.

[4] J. Fischer, "On ejector technology," *International journal of refrigeration,* vol. 36, no. 4, pp. 1399-1400, 2013.

[5] J. Keenan, E. Neuman and F. Lustwerk, "A simple air ejector," *Mech ASME,* vol. 64, pp. 75-81, 1942.

[6] J. Keenan, E. Neumann and F. Lustwerk, " An Investigation of Ejector Design by Analysis and Experiment," *Journal of Applied Mechanics ,* vol. 17 , pp. 299-309, 1950.

[7] K. Chunnanond and S. Aphornratana, "Ejectors: applications in refrigeration technology," *Renewable and Sustainable Energy Reviews,* vol. 8, p. 129–155, 2004.

[8] J. T. Munday and D. F. Bagster, "A new ejector theory applied to steam jet refrigeration," *Ind. Eng. Chem. Proc. Des. Dev.,* vol. 164, pp. 442-449, 1977.

[9] S. Kneass, Practice and theory of the injector, New York: John Wiley & Sons, 1910.

[10] R. Thévenot, A history of refrigeration: throughout the world, International institute of refrigeration, 1979.

[11] C. Arora, Refrigeration and Air Conditioning, Tata-McGraw-Hill, 2003.

[12] K. Banasiak, A. Hafner and T. Andresen, "Experimental and numerical investigation of the influence of the two-phase ejector geometry on the performance of the R744 heat pump," *International Journal of Refrigeration,* vol. 35, pp. 1617-1625, 2012.

[13] ASHARE, "Steam-jet refrigeration equipment," in *ASHARE equipment Handbook*, Atlanta, GA, USA, 1983, pp. 13.1-13.6.

[14] Z. Aidoun, K. Ameur, M. Falsafioon and M. Badache, "Current advances in ejector modelling, experimentation and applications for refrigeration and heat pump. Part1: Single phase ejectors," *Inventions,* vol. 4, no. 1, 2019.

[15] S. Aphornratana, S. Chungpaibulpatana and P. Srikhirin, "Experimental investigationof an ejector refrigerator: Effect of mixing chamber geometry on system performance," *Energy Research,* vol. 25, pp. 397-411, 2001.

[16] R. Yapici and H. Ersoy, "Performance characteristics of the ejector refrigeration system based on the constant area ejector flow model," *Energy conversion and managemement,* vol. 46, pp. 3117-3135, 2005.

[17] K. Pianthong, W. Seehanam, M. Behnia, T. Sriveerakul and S. Aphornratana, "Investigation and improvement of ejector refrigeration system using computational fluid dynamics technique," *Energy Conversion and Management,* vol. 48(9), pp. 2556-2564, 2007.

[18] Z. Ma, H. Boa and A. Roskilly, "Thermodynamic modelling and parameter determination of ejector for ejection refrigeration system," *International journal of refrigeration,* vol. 75, pp. 117-128, 2017.

[19] A. Hanafi, G. Mostafa, A. Waheed and A. Fathy, "1-D mathematic modelling and CFD investigation on supersonic steam ejector in MED-TVC," in *the 7th international conference on applied energy - ICAE2015*, 2015.

[20] J. Mahmoudian, A. Milazzo, I. Murmanskii and A. Rocchetti, "Experimental results from R245fa chiller," in *Heat powered Cycles*, Bayreuth, Germany, 2018.

[21] I. Eames, "A new prescription for the design of supersonic jet-pumps: the constant rate of momentum change method," *Applied Thermal Engineering,* vol. 22, p. 121–31, 2002.

[22] I. Eames, A. Ablwaifa and V. Petrenko, "Results of an experimental study of an advanced jet-pump refrigerator operating with R245fa," *Applied Thermal Engineering,* vol. 27, pp. 2833-284, 2007.

[23] B. Kittratana, S. Aphornratana, T. Thongtip and N. Ruantrakoon, "Comaprison of traditional and CRMC ejector performance used in steam ejector refrigeration," *Energy procedia,* vol. 138, pp. 476-481, 2017.

[24] A. Milazzo, A. Rocchetti and I. Eames, "Theoretical and experimental activity on Ejector Refrigeration," *Energy Procedia ,* vol. 45 , p. 1245 – 1254, 2014 .

[25] F. Mazzelli and A. Milazzo, "Performance analysis of a supersonic ejector cycle working with R245fa," *International Journal of Refrigeration,* vol. 49, pp. 79-92, 2015.

[26] J. Taylor, An introduction to error analysis, 2nd edition, Sausalito, CA: University science books, 1997.

[27] R. Figliola and D. Beasley, Theory and design for mechanical measurements, 3rd edition, Hoboken, NJ: John Wiley & Sons Inc, 2000.

[28] R. Moffat, "Describing the uncertainties in experimental results," *Experimental thermal and fluid science,* vol. 1, pp. 3-17, 1988.

[29] *NIST REFPROP, Reference Fluid Thermodynamic and Transport Properties Database, version 9.1,* 2018.

[30] Y. Fang, S. Croquer, S. Poncet, Z. Aidoun and Y. Bartosiewicz, "Drop-in replacement in a R134 ejector refrigeration cycle by HFO refrigerants,," *Int. J. Refrigeration, ,* vol. 121, pp. 87-98, 2017.

[31] B. Huang, J. Chang, C. Wang and V. Petrenko, "A 1-D analysis of ejector performance," *International Journal of Refrigeration ,* vol. 22, p. 354–364, 1999.

[32] G. Grazzini, A. Milazzo and F. Mazzelli, Ejectors for Efficient Refrigeration, Springer, 2018.

[33] J. Mahmoudian, F. Mazzelli, A. Milazzo and A. Rocchetti, "Experiemntal and numerical activity on a prototype ejector chiller," in *37th UIT Heat transfer conference* , Padova, 2019.

[34] M. Milazzo and A. Rocchetti, "Modelling of ejector chillers with steam and other working fluids," *International Journal of Refrigeration,* vol. 57, pp. 277-287, 2015.

[35] K. Shestopalov, B. Huang, V. Petrenko and O. Volovyk, "Investigation of experimental ejector refrigeration machine operating with refrigeratnt R245fa at design and off-design working condition. Part1: Theoretical analysis," *internation journal of refrigeration,* vol. 29, pp. 201-211, 2015.

[36] K. Shestopalov, B. Huang, V. Petrenko and O. Volovyk, "Investigation of an experimental ejector refrigeration machine operating with refrigerant R245fa at design and off-design working conditions. Part2: Theoretical and

experimental results," *International journal of refrigeration,* vol. 55, pp. 212-223, 2015.

[37] J. Mahmoudian, A. Milazzo, I. Murmanskii and A. Rocchetti, "Experimental results from R245fa chiller," in *Heat powered Cycles*, Bayreuth, Germany, 2018.

[38] A. Ablwaifa, I. Eames and V. Petrenko, "Experimental validation of CFD model used to design jet-pumps," in *International seminar on ejector/jet-pump technology and application*, Louvain-La-Neuve, Belgium, 2009.

[39] E. Narimani, M. Sorin, P. Micheau and H. Nesreddine, "Dynamic modeling of an R245fa ejector based refrigeration system," *International journal of refrigeration,* 2019.

[40] M. Bencharif, S. Poncet, H. Nesreddine and S. Zid, "Droplet injection at the diffuser outlet in an ejector-based refrigeration cycle working with R245fa," in *25th IIR international congress of refrigeration*, Montréa, Canada, 2019.

[41] J. M.Calm, "The next generation of refrigerants - historical review, consideration, and outlook," *International journal of refrigeration,* vol. 31, no. 7, pp. 1123-1133, 2008.

[42] S. Eyerer, F. Dawo, J. Kaindl, C. Wieland and H. Spliethoff, "Experimental investigation of modern ORC working fluids R1224zy(Z) and R1233zs(E) as replacemnets for R245fa," *Applier energu journal,* vol. 240, pp. 946-963, 2019.

[43] Y. Jingye, h. ye, B. Yu, H. Ouyang and J. Chen, "Simultaneous experimental comparison of low GWP refrigerants as drop-in replacemnets to R245fa for Organic Rankine cycle application: R1234ze(Z), R1233zd(E) and R1336mzz(E)," *Energy,* vol. 173, pp. 721-731, 2019.

[44] B. Dalta and J. Brasz, "Comparing R1233zd and R245fa for low temperature ORC applications," in *15th International refrigeration and air conditioning conference*, Purdue, 2014.

[45] S. Eyerer, C. Wieland, A. Vandersickel and H. Spliethoff, "Experimental study of an ORC (Organic Rankine Cycle) and analysis of R1233zd-E as a drop-in replacement for R245fa for low temperature heat utilization," *Energy,* vol. 103, pp. 660-671, 2016.

[46] K. Matsuo, Y. Miyazato and H. Kim, " Shock train and pseudo-shock phenomena in internal gas flows," *Progress in Aerospace Sciences ,* vol. 35 , pp. 33-100, 1999.

[47] B. Carroll, P. Lopez-Fernandez and J. Dutton, "Computations and experiments for a multiple normal shock/boundary-layer interaction," *propul power,* vol. 9, pp. 405-411, 1993.

[48] R. Yamane, S. Oshims, Y. Nakamura, T. Ishii and M. Park, "Numerical simulation of pseudo-shock in straight channels," *JSME Int.J.Series B,* vol. 38, pp. 549-554, 1995.

[49] A. Little and S. Garimella, "A critical review linking ejector flow phenomena with component- and system-level performance," *International Journal of Refrigeration,* vol. 70, pp. 243-268, 2016.

[50] D. Sun and I. Eames, "Recent developments in the design theories and applications of ejectors- a review," *Energy,* vol. 68, pp. 65-79, 1995.

[51] F. Mazzelli, A. B. Little, S. Garimella and Y. Bartosiewicz, "Computational and Experimental Analysis of Supersonic Air Ejector: Turbulence Modeling and Assessment of 3D Effects," *International Journal of Heat and Fluid Flow,* vol. 56, pp. 305-316, 2015.

[52] H. Al-ansary and S. Jeter, "Numerical and experimental analysis of single-phase and two-phase flow in ejectors," *HVAC R Res.,* vol. 10, pp. 521-538, 2004.

[53] P. Desevaux and O. Aeschbacher, "Numerical and experimental flow visualization of the mixing process inside an induced air ejector," *Turbo jet-engines,* vol. 19, pp. 71-78, 2002.

[54] Y. Zhu and P. Jiang, "Experimental and numerical investigation of the effect of shock wave characteristics on the ejector performance," *International Journal of Refrigeration,* vol. 40, pp. 31-42, 2014b.

[55] Y. A. Z. D. P. M. Y. Bartosiewicz, "CFD/experiments integration in the evaluation of six turbulence models for supersonic ejector modeling," in *Integration CFD and Exsperiments*, Glasgow, UK, 2003.

[56] Y. Bartosiewicz, Z. Aidoun, P. Desevaux and Y. Mercadier, "Numerical and experimental investigations on supersonic ejectors," *International Journal of Heat and Fluid Flow,* vol. 26, pp. 56-70, 2005.

[57] Y. Bartosiewicz, Z. Aidoun and Y. Mercadier, "Numerical assessment of ejector operation for refrigeration applications based on CFD," *Applied thermal engineering,* vol. 26, pp. 604-612, 2006.

[58] J. García del Valle, J. Sierra-Pallares, P. Garcia Carrascal and F. Castro Ruiz, "An experimental and computational study of the flow pattern in a refrigerant ejector. Validation of turbulence models and real-gas effects," *Applied Thermal Engineering 1,* vol. 89 , pp. 795-81, 2015.

[59] S. Croquer, S. Poncer and Z. Aidoun, "Turbulence modeling of a single-phase R134a supersonic ejector. Part1: numerical benchmark," *International journal of refrigeration,* vol. 61, pp. 140-152, 2016.

[60] Z. Aidoun, K. Ameur, M. Falsafioon and M. Badache, "Current Advances in Ejector Modeling, Experimentation and Applications for Refrigeration and Heat Pumps. Part 1: Single-Phase Ejectors," *Inventions,* 2019.

[61] ANSYS Inc., ANSYS Fluent Theory Guide, Canonsburg, PA: release 19.0, 2018.

[62] F. Menter, J.C. Ferreira, T. Esch, B. Konno, "The SST turnulance mdel with improved wall treatment for heat transfer predictions in gas turbines," in *International Gas Turbine Congress*, Tokyo, 2003.

Part II: Water Vapour Condensation inside a Supersonic Nozzle Operated through Shock tunnel

3 Water Vapour Condensation

This chapter presents a shock tunnel for analysis of steam nozzle flows has been developed and tested at University of Southern Queensland. High-speed flow visualisation of the water vapour condensation shock in the throat region of a supersonic nozzle attached to the shock tube are performed. This chapter describe the facility performance and the time-resolved 2D visualisation results using quasi-one-dimensional thermodynamic analyses based on ideal gas for the water vapour in different operating conditions.

This research is linked to the previously described activity on ejector chillers [1], whose ultimate target is to build a steam ejector chiller. Condensation problems within the primary nozzle of the ejector are thought to be a major problem and the chance of getting a first-hand experience on the experimental and numerical analysis of supersonic steam nozzles offered by University of Southern Queensland was indeed a precious opportunity. The experience gathered in Australia is here resumed in detail.

3.1 Overview

Non-equilibrium condensation of steam occurs in many jet and turbomachinery devices, such as supersonic nozzles and across low pressure stages of steam turbines. Normal operation of these devices involves very high expansion rates that lead to a substantial departure from the equilibrium process [2]. As the steam accelerate inside a nozzle or blade vane, thermodynamic equilibrium is not maintained and, at a certain degree of expansion, the vapour state collapses and condensation takes place as a “condensation shock” [3]. This sudden phase change leads to a localized heat release that increases the pressure and temperature and reduces the Mach number [3]. Downstream of the condensation shock, the flow contains a considerable number

of tiny liquid droplets (of the order of $10^{19}/cm^3$, [4]) that can interact in non-trivial ways with shock waves and turbulent structures.

Experimental analysis of condensation shocks can be performed by at least two different techniques: the first involves condensation in cloud and expansion chambers and is commonly used in meteorological studies. The second deals with the analysis of supersonic expansions in De Laval nozzles. This last approach is generally employed in the fields of turbomachinery and aerodynamics studies and, as was shown by many authors (e.g., [3]; [4]), it is a remarkable test configuration for wet steam model theories. The advantages are numerous: first, converging/diverging nozzles generally entail a **steady** 1D flow configuration that can be easily reproduced by quasi-1D (Q1D) theories and that allows detecting the effects of condensation by simple pressure measurements. Moreover, it was shown by Stodola that for this type of expansion the effects of dust particles are entirely insignificant, meaning that the condensation is of the homogeneous type [4]. By contrast, the major drawback of nozzle experiments is that the water cluster nucleation and droplet growth stages are tightly coupled and is hard to validate the corresponding theories separately [5]. Therefore, it is crucial to design experiments that provide for redundant information, such as pressure trends, condensation onset locations and information on droplet sizes distribution.

Among the many nozzle experiments that can be found in the literature, that of Moore *et al.* [6] and Moses and Stein [7] appear to be still the most popular test cases for validating wet steam models, as proved by their recent adoption in the International Wet Steam Modelling Project [8].

Moses and Stein [7] investigated steam condensation inside a planar cross section nozzle with static pressure probes and laser light scattering. The pressures were acquired along the nozzle centerline, thus providing information on both the condensation onset position and pressure increase due to the latent heat release. The authors concluded that the use of both static pressure and light scattering measurements proved to be complementary for certain operating conditions. In addition, the light

scattering proved to be more sensitive to changes in droplet size distributions than the static pressure.

Moore et al [6] investigated different planar convergent-divergent nozzles with various expansion rates. Pressure measurements were achieved both on the plane side-wall and along the centerline. The Sauter mean droplet radius on the centerline was obtained using a light extinction method [9]. The tests were compared with various nucleation theories, of which, the one of Deich et al [10] gave the best accord with experiments.

More recent studies involving visualization of condensation of pure steam were reported for instance by Dykas et al. [11] who carried out experimental and numerical investigations on a De-Laval nozzle with small divergence angle of the supersonic region. The authors justify this choice by arguing that it leads to an increased numerical sensitivity of the condensation wave location to the boundary layer model, inlet conditions and fluid properties. The comparative analysis of the results provided unequivocal confirmation of significant differences that occur between CFD and measurements. The authors suggested that these differences may either be due to experimental or modelling uncertainties and insisted that numerical studies should focus not on the models calibration, but rather on the search for a physical justification for the discrepancies in the results compared to measurements [11].

Most of the experiments that can be found in the literature use pure steam in a steady or quasi-steady flow experiment configuration. This approach has the advantage of an easy control of inlet stagnation conditions and allows a clear visualization of the condensation shock due to the practically unlimited availability of vapour molecules that can condense over the liquid clusters surface, thus producing a clean-cut disturbance. Nonetheless, these types of steady flow experiments require massive amounts of pure steam. For instance, Moore et al. used relatively large throat sizes (the smallest being 62 x 152 mm) which amounted to a maximum flow rate of around 5 kg/s [6], which means ~18 tons of steam per hour of operation. Such quantities of steam can become extremely difficult to achieve in a University context mostly because of budget constraints.

One way to overcome this issue is to analyze the condensation of water vapour inside a stream of humid air. This type of approach has the key advantage that no steam must be produced. One of the most interesting study that used this technique was carried forward by Schnerr [12], who made a very detailed visualization study of condensation inside an air stream with different relative humidity. Schnerr used an atmospheric air blow-down wind tunnel facility. The main limitation of this approach is that the stagnation conditions are dictated by the atmospheric pressure and temperature. Therefore, it is difficult to control the degree of superheat of the water vapour. Besides, flow stagnation pressure conditions other than atmospheric pressure are not readily obtainable with this kind of arrangement.

In order to obtain a good control of the inlet stagnation conditions and simultaneously reduce the amount of required test gas it is possible to employ a fast transient flow test configuration, such as shock tunnels or Ludwieg tubes [13]. In this type of experimental approach, a driver fluid (e.g., nitrogen or air) is compressed via a batch process and then used to accelerate a driven fluid through a convergent divergent nozzle, typically connected to an evacuated dump tank [14]. As long as sufficiently fast instrumentation is adopted, useful contributions can be made because the quasi-steady flow establishment process occurs rapidly when the flow speeds are high. Thanks to the low amount of working fluid, these fast transient approaches allow to relatively large nozzle dimensions to be mentioned, thus enabling convenient optical access and easier insertion of other sensors.

Shock tubes and Ludwieg tubes have been successfully used to generate a wide range of supersonic flow conditions suitable for aerodynamic testing. For example, high enthalpy, hypersonic testing facilities have been operated for a number of decades and developed [15], [16] and [17]. These facilities sometime use a free piston compressor to generate a new facilities continue to be high temperature gas reservoir, which drives a strong shock wave through the test gas. Ludwieg tunnel facilities have been developed for fundamental experiments using different test gases [18] and in supersonic flow experiments [19].

Prior work with shock tunnel and Ludwieg has used single phase flow of dry air or other gases and the liquefaction of the test gas is purposely avoided in order to generate suitable aerodynamic test conditions. To the authors' knowledge, this work represents the first attempt to analyze the water vapour condensation inside steam using shock tunnel and Ludwieg tubes. In what follows, the paper presents the preliminary results obtained using both these techniques.

3.2 Experimental Apparatus

3.2.1 2D Supersonic nozzle

The two dimensional convergent-divergent nozzle (Figure 3.1) was specified using a circular arc profile in the throat region and a Bezier curve in divergent region. The inlet convergent region (Figure 3.2B) starts with 5 mm radius in order to have a smooth transition at the end of shock tube into the nozzle contraction. The inlet, on the other hand, is large enough to allow a ruptured diaphragm to lay against it and not interfere with flow in throat contraction region. Flow keeps accelerating towards the nozzle throat through 8 degrees contraction angle in order to avoid boundary layer separation (Figure 3.2B). Then, the 75 mm radius of curvature throat region is large enough to give a sonic line with only moderate curvature (Figure 3.2C)

Figure 3.1 3D printed nozzle

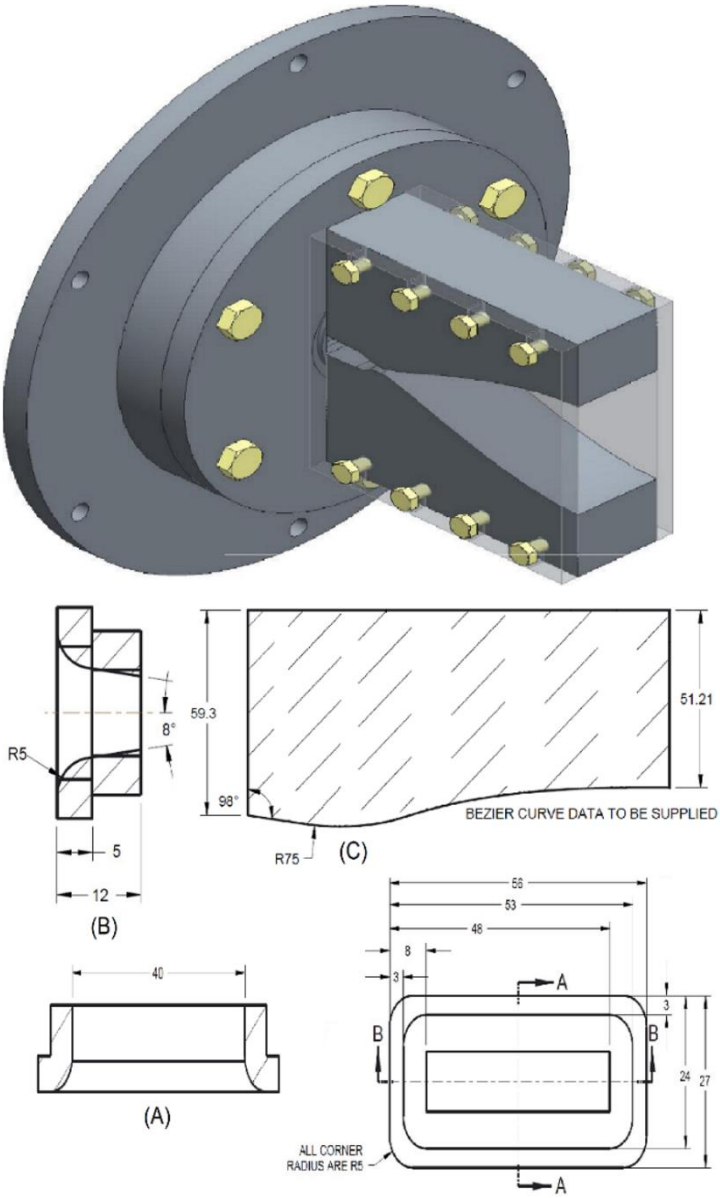

Figure 3.2 Solid model rendering illustrating the nozzle

The throat area (3 mm height and 40 mm nozzle width) is less than 5% of the shock tube area in order to minimize the impact of the discharge through the nozzle on the reflected shock strength that forms at the end of the tube. The nozzle was designed using a method of characteristic in order to achieve a uniform flow at M = 3.5 at the nozzle exit for γ = 1.33. It has an area ratio of $A_{exit}/A^* = 8.5$ and is fabricated in nylon by 3D printing. The main geometrical parameters of the nozzle are shown in Table 3.1.

Width [mm]	40
Throat height [mm]	3
Inlet height [mm]	10.68
Exit height [mm]	25.58
Length [mm]	140
Material	Nylon

Table 3.1 Main geometrical parameters of the 2D supersonic nozzle

The full detail and more information about design of the nozzle, nozzle connector and nozzle flange show in Figure 3.14, Figure 3.15, Figure 3.16 and Figure 3.17respectively.

3.2.2 Impulse Facility

3.2.2.1 General Arrangement and Operation

Figure 3.3 presents a schematic illustration of the impulse tunnel: a 6.5 m long tube with an internal diameter of 62 mm is coupled to the nozzle. An evacuated test section is connected to the dump tank via a series of axially aligned pipes. The nitrogen reservoir has a total volume of approximately 7.5 liters and is connected to the other side of the tube.

Initially, the high vacuum pump evacuates the air and produces low pressure in the tube. Subsequently, the tube is filled up with dry nitrogen, which is then evacuated out a second time in order to minimise any residual moisture in the tube.

Temperature and pressure sensors are mounted in all the significant points along the experimental apparatus, while two fast response pressure sensors are flush mounted along the tube and driven section at specific location. In addition, thermocouples sensors are more concentrated close to the nozzle in order to monitor the flow temperature passing through nozzle. The specifications of the main sensors are reported in Table 3.2.

3.2.2.2 Operation as Ludwieg Tunnel

Operation as Ludwieg tunnel consists in placing one cellophane diaphragm at the nozzle inlet. Water vapour is introduced in the evacuated tube. The desired Relative humidity "Rh" is reached by injecting a controlled amount of liquid water mass. During this operation, the value of Rh is monitored by measuring the ratio between the static pressure inside the tube and the water vapour saturation pressure at the tube temperature.

Once the desired Rh is reached, the experiment is initiated by rupturing the cellophane diaphragm at the nozzle inlet by adding nitrogen to the tube until the bursting pressure is reacted.

3.2.2.3 Operation as Shock Tunnel

In shock tunnel operation mode, a light diaphragm (Mylar, 100 μm thick) divides the driver (2.5 m long, high pressure) and driven sections (4 m, low pressure). Moreover, a cellophane layer separates the driven sections from the nozzle and dump tank.

Again, the desired relative humidity in the driven section is measured considering the ratio between the static pressure and the water vapour saturation pressure at the driven section temperature. The final step of the experimental preparation consists in incrementing the pressure in the driven section up to the am-

bient pressure with Nitrogen. The experiment is initiated by rupturing the Mylar diaphragm by means of the introduction of compressed air into the driver section.

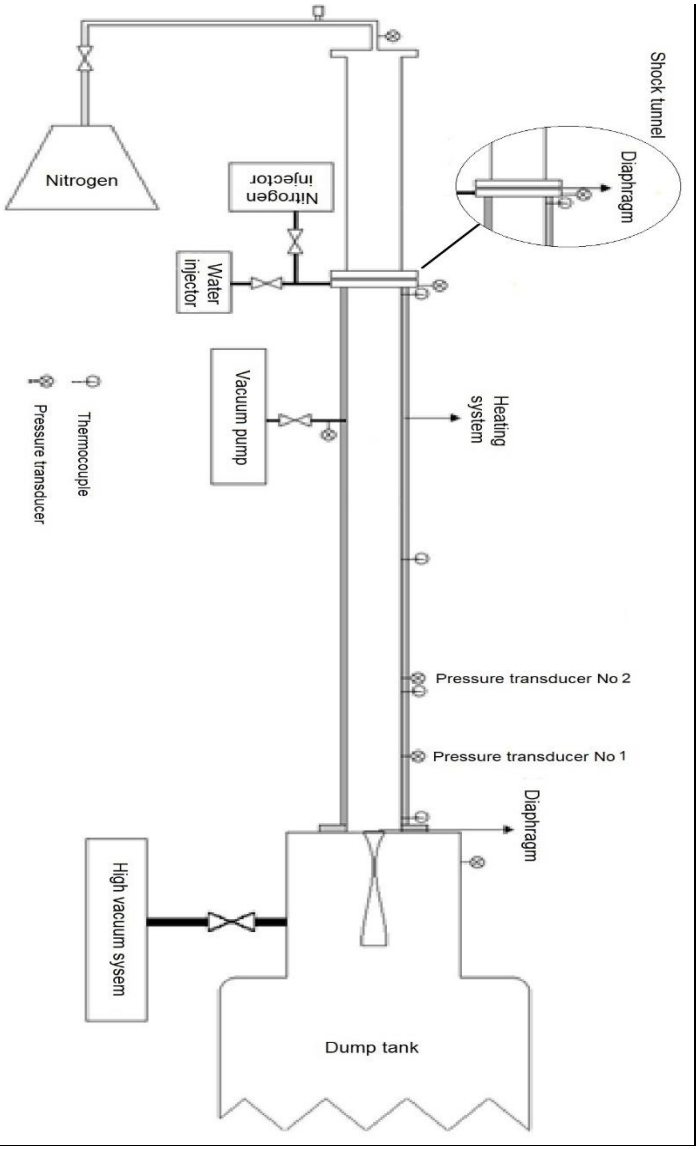

Figure 3.3 Impulse (Ludwieg) tunnel experimental setup. The shock tunnel configuration is created by adding a diaphragm in the tube middle section and changing nitrogen with air.

Instrument	Model/Type	position	ADC Module	Total uncertainty
Piezoreistive pressure transducer	PTX 1400 0 – 2.5 bar	Ludwieg tunnl	PCI-6110	±(0.15% – 0.25% FS)
		Shock tunnel		
	WIKA A10 0 – 40 bar	Ludwieg tunnl	PCI-6110	≤ ±0.5 % FS
		Shock tunnel		
	WIKA A10 -1 – 0 bar	Ludwieg tunnl	PCI-6110	±(0.25% – 0.5% FS)
		Shock tunnel		
	PCB 482	Ludwieg tunnl	PCI-6110	
		Shock tunnel		
Thermocouple	T	Ludwieg tunnl	NI9219	±1.0°C
		Shock tunnel		

position
Tube (Nitrogen feed)

Driver section inlet (Dry air)
Tube, Tank
Driven section, Tank
Tube
Driven section
Tube
Driven section

Table 3.2 Specification of the sensors and data acquisition

3.2.3 Schlieren Imaging System

A Schlieren imaging system (Figure 3.4) is used to visualize condensation shock in the vicinity of the nozzle throat. The windows in the present system provide a field of view of 100 mm diameter and they are fixed into the flanges on the test section, so the current arrangement allows only for discrete viewing positions, corresponding to the pitch of the flange boltholes. The Schlieren system for the present work used a continuous LED light source collimated by a 1000 mm focal length lens. The focusing lens also had an $f_1 = f_2 = 1000$ mm focal length and a horizontal knife edge was positioned at the focus of the light source image. A Photron SA3 camera with a frame rate of 5000 frame per second was used to image the flow.

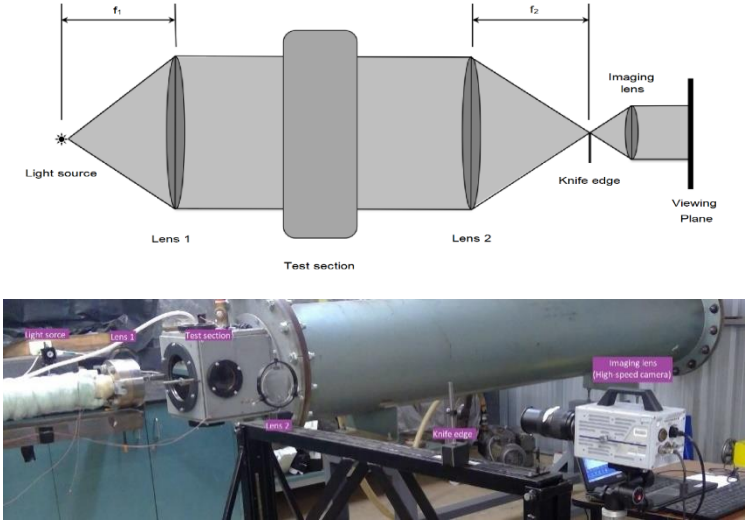

Figure 3.4 Schlieren scheme (top) and Schlieren test platform (bottom)

3.3 Thermodynamic Modelling

3.3.1 Shock Tube

Figure 3.5a shows the original concept of the shock tube, which consists of a straight cylindrical tube closed at both ends, with a diaphragm separating a region of high-pressure gas (region 4 / Driver section) from a region of low-pressure gas (region 1 / Driven section). The gasses in both regions can be at different temperatures and have different molecular weight. Figure 3.5b sketches an incident shock wave that propagates into the driven section and the corresponding expansion wave that propagates into the driver section after the diaphragm is ruptured.

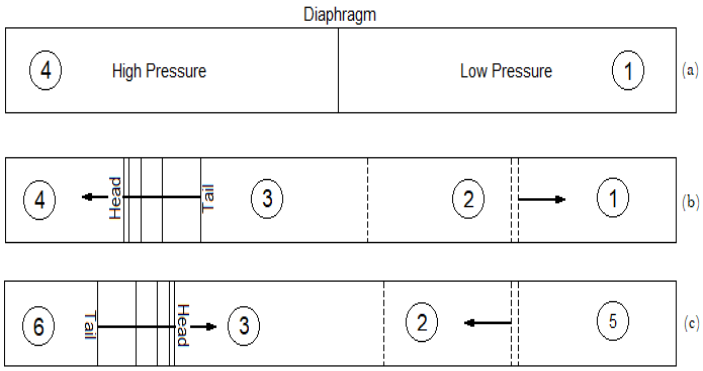

Figure 3.5 Incident, expansion and reflected shock waves in shock tube

Anderson [20] reports the incident shock wave velocity, W_s and mass motion velocity, u_2 by the following formulas:

$$a = \sqrt{\gamma RT} \qquad \textit{Eq 3. 1}$$

$$W_s = a_1 * M_s = a_1 * \sqrt{\frac{\gamma_1+1}{2\gamma_1}\left(\frac{P_2}{P_1}-1\right)+1} \qquad \textit{Eq 3. 2}$$

$$u_2 = \frac{a_1}{\gamma_1}\left(\frac{P_2}{P_1} - 1\right)\left(\frac{\frac{2\gamma_1}{\gamma_1+1}}{\frac{P_2}{P_1} + \frac{\gamma_1-1}{\gamma_1+1}}\right)^{1/2}$$

Eq 3. 3

$$\frac{P_4}{P_1} = \frac{P_2}{P_1}\left\{1 - \frac{(\gamma_4 - 1)(a_1/a_4)(P_2/P_1 - 1)}{\sqrt{2\gamma_1[2\gamma_1 + (\gamma_1+1)(P_2/P_1 - 1)]}}\right\}^{-2\gamma_4/(\gamma_4-1)}$$

Eq 3. 4

P_4/P_1 is the diaphragm pressure ratio before the rupturing, whereas the relation $P_2 = P_3$ is valid after the diaphragm removal.

The local velocity of any part of the left running expansion wave is $u - a$, hence the head of the wave spreads through the driver section with a velocity $-a_4$ because the mass-motion velocity in region 4 is zero. The velocity behind the expansion wave is calculated by [20]:

$$u_3 = \frac{2a_4}{\gamma_4 - 1}\left[1 - \left(\frac{P_2}{P_4}\right)^{(\gamma_4-1)/2\gamma_4}\right]$$

Eq 3. 5

The incident shock wave traveling to the right has mass velocity in the front $u_1 = 0$. Behind the shock the velocity is u_2.

When the incident shock wave impacts the end wall it is reflected back. The reflected shock wave moves to the left with velocity W_r and mass velocity behind the wave $u_5 = 0$.

$$\frac{M_R}{M_R^2 - 1} = \frac{M_S}{M_S^2 - 1}\sqrt{1 + \frac{2(\gamma_1 - 1)}{(\gamma_1+1)^2}(M_S^2 - 1)(\gamma_1 + \frac{1}{M_S^2})}$$

Eq 3. 6

$$W_r = a_1 * M_r \qquad \textit{Eq 3. 7}$$

$$\frac{P_5}{P_2} = 1 + \frac{2\gamma_1}{\gamma_1 + 1}(M_r^2 - 1) \qquad \textit{Eq 3. 8}$$

$$\frac{P_5}{P_1} = \frac{P_5}{P_2} * \frac{P_2}{P_1} \qquad \textit{Eq 3. 9}$$

3.3.2 Shock Tunnel

The shock tube formulations presented in section 3.3.1 are used to compute the pressure trend during the shock tunnel experiments. In contrast with the basic shock tube configuration, in the shock tunnel (shown in Figure 3.6a), the driven section is directly connected to the steam nozzle. When the diaphragm ruptures, a right-running incident shock start to sweep the driven section and then enters the steam nozzle after rupturing the cellophane diaphragm at its inlet. The shock then accelerates through the nozzle (Figure 3.6b) and cause the nozzle to choke. On the other side of the tube, expansion waves spread through the driver section. During this stage, nozzle and tube are staying at constant pressure $P_2 = P_3$, named as the first plateau. The incident shock wave creates a reflected normal wave when it makes contact with the tube end wall and it moves back toward the center of the tube. A similar process occurs for the left-running expansion wave, which is reflected by the left end wall and accelerate to the right (Figure 3.6c). The system reaches the second plateau when the reflected expansion wave arrives at the nozzle inlet and is reflected again toward the tube. This process is repeating and gives rise to a number of successive plateaus.

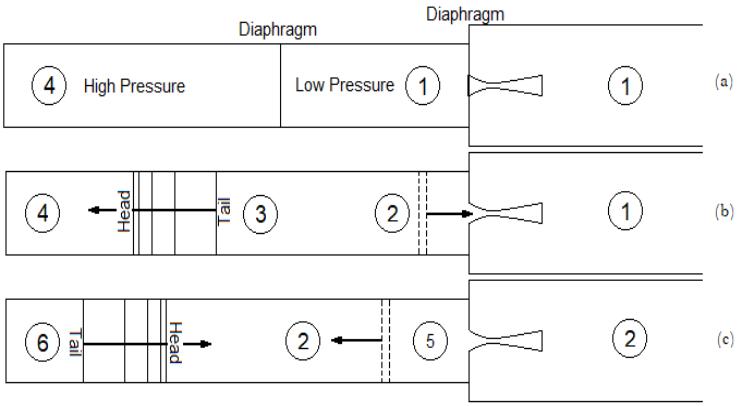

Figure 3.6 Incident, expansion and reflected shock waves in shock tunnel

3.3.3 Ludwieg Tunnel

In the Ludwieg tunnel experimental setup, the cellophane diaphragm separates the nozzle from the tube. In this configuration, the nozzle act as the driven section and the whole tube is the driver section (Figure 3.7a). When the diaphragm is ruptured, the incident shock wave immediately propagates into the evacuated nozzle and an unsteady expansion wave spreads upstream the driver tube (Figure 3.7b). The driver tube flow is somewhat more complex since it must accommodate the nozzle boundary conditions at the downstream end of driver tube [21]. Knauss et al. [22], calculated the Mach number behind the expansion wave (M_3) by imposing the mass conservation between the nozzle throat and driver tube section. The knowledge of M_3 determines the strength of the expansion wave, from which other properties follow,

$$\left(\frac{A_4}{A^*}\right)^2 = \frac{1}{M_3^2}\left[\frac{2}{\gamma_4+1}\left(1+\frac{\gamma_4-1}{2}M_3^2\right)\right]^{(\gamma_4+1)/(\gamma_4-1)} \qquad \textit{Eq 3. 10}$$

$$\frac{T_4}{T_3} = \left(1 + \frac{\gamma_4 - 1}{2} M_3\right)^2 \qquad \textit{Eq 3. 11}$$

$$\frac{P_3}{P_4} = \left(\frac{T_3}{T_4}\right)^{\gamma_4/(\gamma_4 - 1)} \qquad \textit{Eq 3. 12}$$

Solving the equations above returns the value of pressure $P_2 = P_3$ providing the first stable pressure in the driver section. i.e., the first plateau. During this time there are steady conditions at the nozzle entrance which produce a steady flow through the nozzle. The reflected expansion shock wave generates by the impact of the expansion wave with the left side end wall. This wave sweeps the whole tube and comes back to the nozzle (Figure 3.7c). After the reflected expansion wave passes through the nozzle, the second plateau is obtained (Figure 3.7d). During this time interval, both the nozzle and tube are in stable pressure P_6. The process is repeating in the system and goes through each of the plateaus [21].

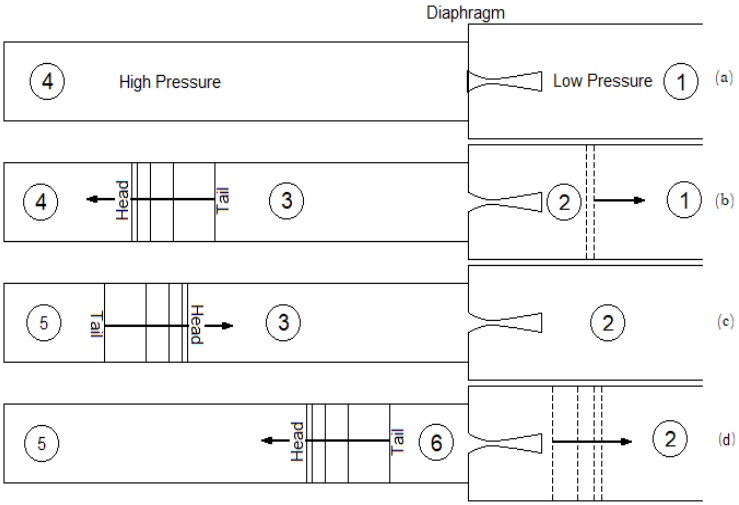

Figure 3.7 Incident, expansion and reflected shock waves in Ludwieg tube

The large volume of the evacuated dump tank ensures that the pressure at the nozzle exit does not increase appreciably during the run time. The run time is limited by the time it takes the non-steady expansion wave to propagate from one end of the driver tube to the other and back, or approximately twice the length of the driver tube. During experiments, each time the expansion runs through the driver tube the pressure is reduced, but as long as it remains high enough for sustaining supersonic flow through the nozzle the tunnel will continue to operate as a Ludwieg tube.

3.4 Results and Discussion

3.4.1 Ludwieg Tunnel

A typical trace of the Ludwieg tunnel pressure during a 100ms run time is presented in Figure 3.8.The figure shows the various pressure plateaus (1, 2, 3…) reached after the passage of the left-running expansion waves. The expansion wave velocity is calculated by dividing the distance between sensor 1 and sensor 2 (exactly 100 cm, see Figure 3.3) by the time interval between the pressure drops measured by the two sensors, named i in Figure 3.8. The first and second reflected expansion wave velocities, are calculated with the same method considering the intervals ii and iii respectfully.

As can be noted, the pressure trend produced by the pressure transducer 2 shows an anomalous drifting tendency. This anomaly is probably due to a physical damage to the diaphragm during installation. Despite this problem, the transducer is still able to accurately sense the passage of the pressure wave, which is highlighted by a steep change in signal, as shown in Figure 3.8. Consequently, the pressure sensor 2 is used in the present investigation only to calculate the expansion and shock wave speed, as explained above. Conversely, data from pressure transducer 1 are used to calculate both the absolute pressure existing in the tube and the waves speed.

The Ludwieg tunnel is tested at relative humidity ranging from 15% to 100% to study the effect of amount of steam on the nozzle condensation shock. These differential relative humidity tests are made considering two different temperatures, 20°C and 74°C, in order to study the wave reactions with the temperature.

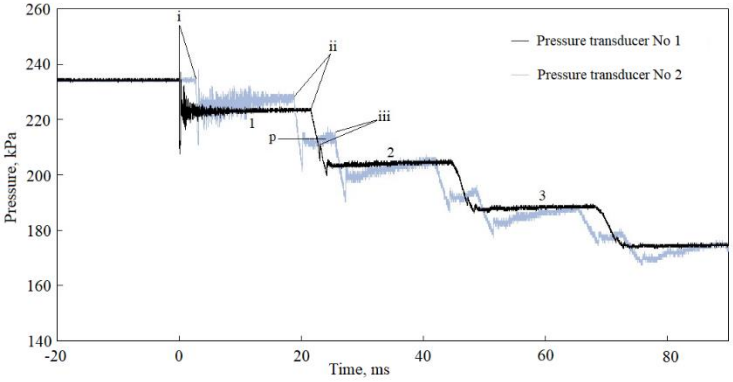

Figure 3.8 Pressure registered by fast respond transducers on the Ludwieg tunnel (Rh = 49% and T = 293°K), 1-first plateau, 2-second plateau, 3-third plateau, i-Expansion wave velocity, ii-reflected expansion wave velocity, iii-second reflected wave velocity, p-pressure behind the reflected expansion wave. Pressure transducer 2 shows an anomalous drift and is used in the present work only to measure the waves speed.

Rh %	T (°C)	First plateau pressure (Pa)		Expansion wave velocity (m/s)		Reflected expansion wave velocity (m/s)		Second plateau pressure (Pa) Experimental (2)
		Experimental (1)	Thermodynamic formula	Experimental (i)	Thermodynamic formula	Experimental (ii)	Thermodynamic formula	
23	293	261801	260170	352.2367	353.6185	363.1082	364.9975	238775
49	293	223270	221650	354.7357	361.0242	370.2332	372.7100	204269
70	293	269402	267900	353.2331	363.3226	370.7824	375.1031	245449
92	293	269402	244190	352.7337	369.2159	370.0962	381.2431	224761
14	347	207704	206850	400.8016	383.3210	417.8855	395.6516	186566
23	347	232224	231440	398.8831	383.9853	410.8463	396.3558	210333
50	347	202029	200740	402.2526	393.9516	422.8330	406.7310	184308
97	347	175723	172530	406.8348	415.4367	420.6984	429.0878	164690

Table 3.3 Experimental and thermodynamic calculation of Ludwieg tunnel

Table 3.3 compares the experimental pressures and wave velocities against thermodynamic calculations. Thermodynamic results are obtained by considering a steam and nitrogen mixture in the tube and air in the evacuated dump tank. The mixture

gas constant and specific heat are evaluated using NIST Refprop libraries [23] by calculating the mass fraction of each compound. The results show a good agreement with the experimental data, with an average difference of about 1% in the first pressure plateau, which is the lowest error in the Ludwieg tunnel calculations. Discrepancies are increasing with the number of reflections because viscous dissipation and due to waves disturbance caused by the presence of the nozzle inlet, both of which were not considered in the calculations.

Figure 3.9 presents the Schlieren photos of the condensation shock in the nozzle throat for the case of Rh = 92%, T = 292k, which is also illustrated in Figure 3.8.Only the first 22ms of run time are presented, which consists of the first plateau with steady condition in the nozzle. Each photo has 3ms time gap with respect to the previous one, in order to better display the change in the shock position and configuration.

In particular, the first frame captures the exact moment of formation of the condensation shock. The first nuclei are forming right downstream of the nozzle throat and disturbance appears to be widespread. In the next 3-4 frames the shock becomes clearer and it emerges as neat X-shaped wave. As time increases, the shock moves toward the nozzle throat and it assumes a normal layout. Again, the shock appears to be widespread. This effect could be due to high frequency oscillation that moves the shock position back and forth and that are smoothed out by the high speed camera.

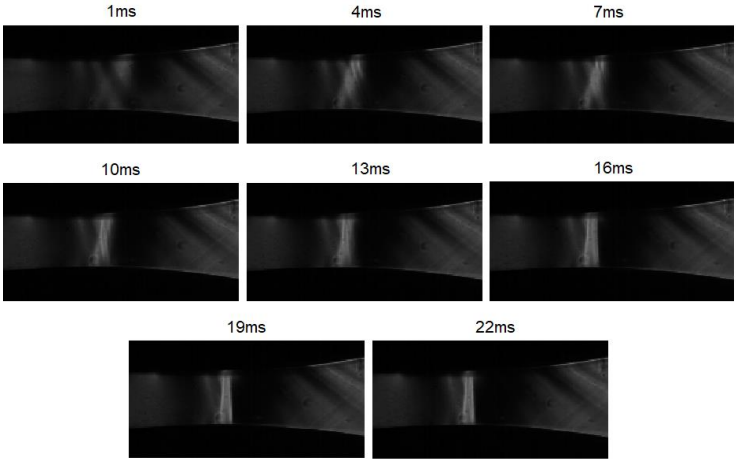

Figure 3.9 Schlieren images from the first 22 ms of steam flow for the case of Ludwieg tunnel, Rh = 92%, T = 293°K. Times are specified relatively to the start of the flow, as shown in Figure 3.8.

3.4.2 Shock Tunnel

A typical trace of the shock tunnel pressure during a 100ms run time is presented in Figure 3.10. The figures show various plateaus (1, 2, 3…) created after the incident shock wave made by rupturing the diaphragm. The incident shock wave velocity and normal reflected shock wave are shown with i and ii in Figure 3.10 and are calculated by the time interval between the pressure drops measured by the two sensors, as explained in section 3.4.1.

Table 3.4 shows the comparison between the calculated and measured incident and reflected shock wave pressure and velocities. The average difference for the incident shock wave (3.5%) is slightly higher than Ludwieg tunnel experiment. The difference increase notably after the first shock reflection, reaching values close to 13%. This large discrepancy may be

due to the stronger influence of the nozzle inlet in the shock reflection process.

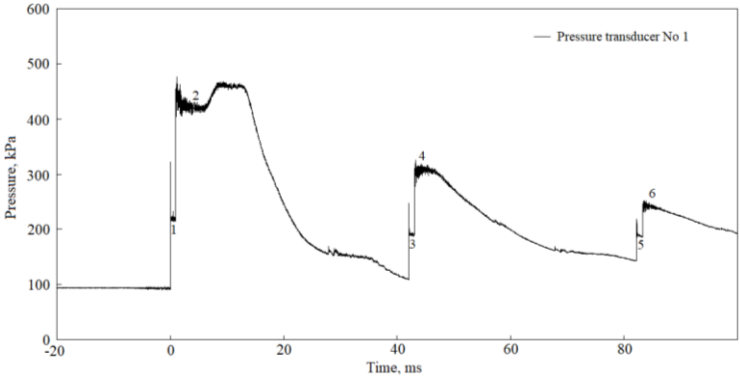

Figure 3.10 Pressure registered by the fast respond pressure transducer No 1 on the shock tunnel (Rh = 50% and T = 297°K); numbers corresponds to the plateaus.

Rh%		25	50
T (°C)		297	297
First plateau pressure (pa) (1)	Experimental	221557	221212
	Thermodynamic formula	207040	207460
Second plateau pressure (pa) (2)	Experimental	429550	421470
	Thermodynamic formula	419520	421060
Incident wave velocity (m/s) (i)	Experimental	503.78	500.75
	Thermodynamic formula	502.31	502.45
Reflected normal wave velocity (m/s) , (ii)	Experimental	310.17	310.55
	Thermodynamic formula	270.79	270.38

Table 3.4 Experimental and thermodynamic calculation of shock tunnel

Figure 3.11 illustrates the Schlieren photos of the condensation shock inside the nozzle throat for the case with Rh = 50%, T = 296k. Considering Figure 3.10, the photos shows the sixth plateau with a steady condition in the nozzle. Although less clear than for the Ludwieg tunnel experiments, the first three photos show that the formation of the condensation shock inside the nozzle occur at a greater distance from the nozzle inlet. The

lower intensity of the shock may be due to a lower pressure difference between the tube and the dump tank. Also, the use of a nitrogen-steam mixture (as opposed to pure steam) may contribute to reduce the intensity and clarity of the shocks, due to a lower presence of available water molecules that condense on the droplet surface. In the 4th and 5th frame the shock moves toward the nozzle throat. Again, the shock appears somewhat widespread and X-shaped. However, as it moves toward the nozzle throat, it gets more concentrated and neat. In the last photo the condensation shock reaches the throat and assumes a normal layout. This change in shock configuration is indeed expected because the angle of a shock disturbance strongly depends on the value of the Mach number upstream of it. As it moves toward the nozzle throat, the condensation shock crosses regions with progressively lower Mach number (in the throat is exactly one), thus assuming a layout closer to a normal shock.

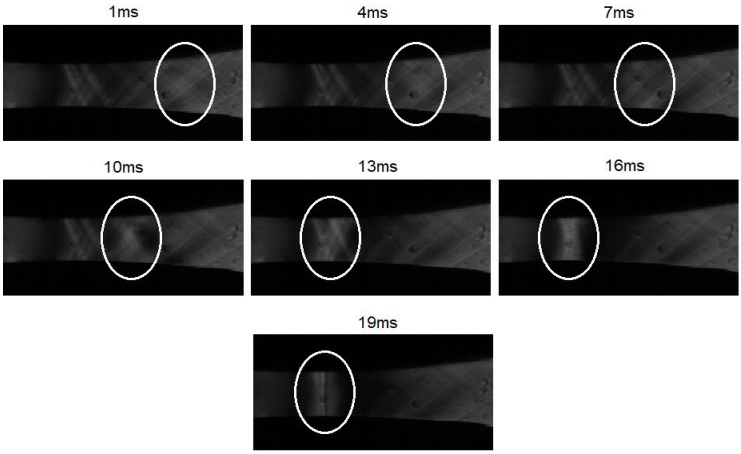

Figure 3.11 Schlieren images from the hypersonic flow for the case of Shock tunnel, Rh = 50%, T = 297°K. Times in the images are shifted with respect to Fig. 9 by setting the zero at the start of the sixth plateau (0.082401 s later than the time zero in Figure 3.10)

Therefore, the visualization of the shock inclination is an important information that can be used to estimate the Mach number inside the nozzle, as will be shown next.

3.4.3 Mach number

The nozzle was designed to achieve M = 3.5 at the nozzle exit. Figure 3.12 shows the Mach number distribution along the nozzle centerline calculated by using a 2D planar method of characteristic. This Mach number trend can be compared with the experiments by estimating the local Mach number from the condensation shock angle. Figure 3.13 shows the condensation shock angles with respect to nozzle centerline (μ) measured during the shock tunnel experimental test (this is the same test illustrated previously in Figure 3.11). As can be seen, the shock angles correctly increase as the disturbance moves closer the nozzle throat. In a single phase flow, the Mach number can be calculated from the compression wave inclination by using the following equation:

$$M = 1/\,sin(\mu) \qquad \textit{Eq 3. 13}$$

The use of this formula to estimate the experimental Mach numbers returns an acceptable agreement between experiments and nozzle design calculations. As illustrated in Figure 3.12.

However, it should be noted that during a condensation shock, the latent heat release can modify the angle of the pressure wave. As Wegener and Mack [3] demonstrated, the governing equation for the condensation shock are different from those of a classical adiabatic shock. In particular, the solution of a standing normal condensation shock should be found by intersecting Rayleigh lines with Hugoniot lines. In our tests, the condensation shocks are mostly oblique, which further increase the complexity of the Mach number evaluation. Nevertheless, the good agreement showed in Figure 3.12 indicates that the effect of

latent heat release may be negligible in the present experiments. This fact may be justified by considering that the tests are performed by using a Nitrogen-Steam mass ratio that is generally below 2% steam, which should significantly reduce the amount and effects of the latent heat release.

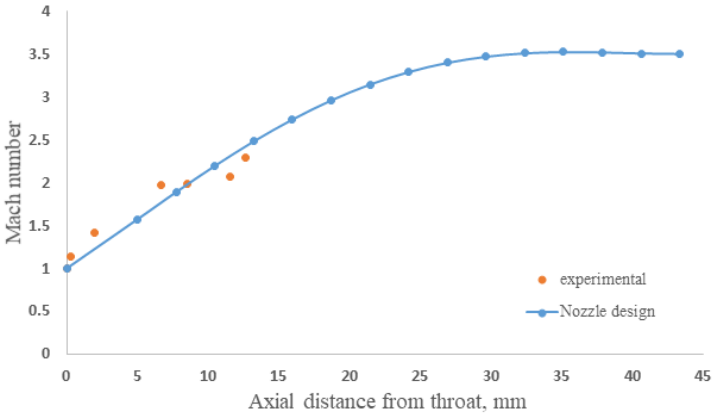

Figure 3.12 Mach number distribution along the nozzle centreline

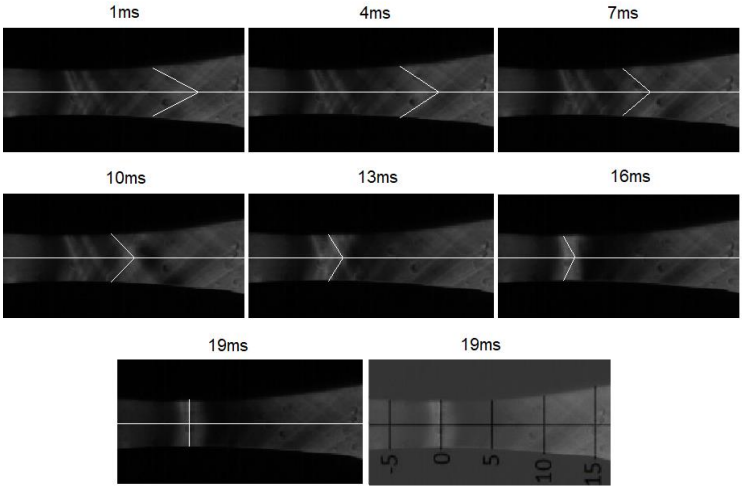

Figure 3.13 Schlieren images of the condensation shock angle with respect to the nozzle axis (Shock tunnel, Rh = 50%, T = 296k). The axial length, shown in the last frame, is measured in mm.

3.5 Concluding Remarks

We have demonstrated the possibility of using a Ludwieg tube and shock tunnel to study the steam condensation inside a convergent-divergent nozzle. Thanks to the fast transient test configuration, this setup allows to obtain a good control of the inlet stagnation conditions and to simultaneously reduce the required amount of operating fluid (either steam or humid air).
Although further perfecting of the equipment is still needed, the experimental apparatus has produced qualitative and quantitative data on pressure and temperature trend, shock wave speed, condensation shock location and condensation shock angle that allow to investigate the fundamental process of supersonic steam expansion with a relatively simple and inexpensive apparatus.

In terms of pressure trend and wave speeds, the comparison between experiments and ideal Q1D calculations have shown a general good agreement, especially in the case of the firsts incident shocks and expansion waves. The differences progressively increase with the number of reflections due to the effect of viscous dissipation and the non-ideal end-wall interaction caused by the presence of the nozzle inlet.

Flow visualization have further allowed to evaluate the condensation shock position. The images have shown a somewhat widespread condensation area. This effect could be due to high frequency oscillation that moves the shock position back and forth and that are smoothed out by the high speed camera.
Finally, the assessment of the condensation angle permitted the indirect estimation of the flow Mach number inside the nozzle, whose values agreed fairly well with theoretical calculations.

References

[1] G. Grazzini, A. Milazzo and S. Piazzini, "Prediction of condensation in steam ejector for a refrigeration system," *International Journal of Refrigeration,* vol. 34, pp. 1641-1648, 2011.

[2] G. Grazzini, A. Milazzo and F. Mazzelli, Ejectors for Efficient Refrigeration, Springer, 2018.

[3] P. Wegener and L. Mack, Condensation in supersonic and hypersonic wind tunnels, New York: Academic Press Inc., 1958.

[4] P. G. Hill, "Condensation of water vapour during supersonic expansion in nozzles," *J. Fluid Mech.,* vol. 25, no. 3, pp. 593-620, 1966.

[5] F. Bakhtar, J. B. Young, A. J. White and D. A. Simpson, "Classical nucleation theory and its application to condensing steam flow calculations," in *Proceedings of the Institution of Mechanical Engineers, Part C: Journal of Mechanical Engineers Science*, 2005.

[6] M. J. Moore, P. T. Walters, P. I. Crane and B. J. Davidson, "Predicting the fog-drop size in wet-steam turbines," 1973.

[7] C. A. Moses and G. D. Stein, "On the growth of steam droplets formed in a Laval nozzle using both static pressure and light scattering measurements," *Journal of Fluids Engineering,* pp. 311-322, 1978.

[8] J. Starzmann, F. R. Huges, A. J. White, J. Halama, V. Hric, M. Kolovratnik, H. Lee, L. Sova, M. Statny, S. Schuster, M. Grubel, M. Schatz, D. M. Vogt, P. Y., G. Patel, T. Turunen-Saaresti, V. Gribin, V. Tishchenko, I. Garilov and

e. al., "Results of the International Wet Steam Modelling Project, Wet Steam Conference," Prague, 2016.

[9] P. T. Walters, "Optical measurement of water droplets in wet steam flows," in *Proc. of IMECHE Conf. Wet Steam 4, Paper C32/73,*, Coventry, UK, 1973.

[10] M. Deich, V. Stepanchuk and G. Saltanov, "Raschet skorosti obrazovaniya tsentrov kondesatsii v pereokhlazhdenom pare (calculation of the rate of formation of condensation nuclei in supercooled steam)," *Izv. Akad. Nauk Uzbek SSR, Energetika i Transport,* vol. 34, no. 2, 1968.

[11] S. Dykas, M. Majkut, K. Smołka and M. Strozik, "An attempt to make a reliable assessment of the wet steam flow field in the De-Laval nozzle," *Heat and Mass Transfer,* vol. 54, p. 2675–2681, 2018.

[12] G. Schnerr, "2-D transonic flow by homogenous condensation: Onset condition and 2-D structure of steady Laval nozzle flow," *Experiments in Fluids,* vol. 7, pp. 145-156, 1989.

[13] H. Ludwieg, "Tube wind tunnel, a special type of blowdown tunnel, technical report," North Atlantic Treaty Organization, 1957.

[14] D. Johnson, "The Design and Implementation of a Supersonic Indraft Tube Wind Tunnel for the Demonstration of Supersonic Flows," Faculty of California Polytechnic State University, 2018.

[15] R. Stalker, A. Paull, D. Mee, R. Morgan and P. Jcop, "Scramjet and shock tunnels - the Queensland experience," *progress in aerospace science,* vol. 41, pp. 471 - 513, 2005.

[16] D. Buttsworth and M. Smart, "develepment of a Ludwieg tube with free piston compression heating for scramjet

inlet starting experiments," in *AIAA aerospace sciences meeting including the new horizons froum and aerospace exposition*, Orlando, Florida, 2010.

[17] B. Byrenn, D. Buttsworth, R. Choudhury and N. Stern, "Characterization of a compression heating in mach 6 configuration," in *international space planes and hypersonic systems and technologies conference*, Orlando, 2018.

[18] D. Buttsworth, "Nitrous oxide decomposition foe supersonic combustion experiments in the USQ Ludwieg tube facility," in *proceeding of the Australian combustion symposium*, Brisbane, Australia, 2009.

[19] D. Buttsworth, "Ludwieg tunnel facility with free piston compression heating supersonic and hypersonic testing," in *proceeding of the 9th Australian space sience conference*, Sydnet, Austalia, 2009.

[20] J. Anderson, Modern compressible flow with historical perspective, McGraw-Hill, 1990.

[21] R. Kimmel, M. Borg, J. Jewell, K. Lam, R. Bowersox, R. Srinivasan, S. Funchs and T. Mooney, "AFRL Ludwieg tube initial performance," in *Aerospace science meeting*, Grapevine, Texas, 2017.

[22] H. Knauss, R. Riedel and S. Wagner, "The shock wind tunnel of Stuttgart University - a facility for testing hypersonic vehicles," *AAIA,* pp. 45-59, 1999.

[23] *NIST REFPROP, Reference Fluid Thermodynamic and Transport Properties Database, version 9.1,* 2018.

Appendix

- Ideal gas shock tube calculations for comparison

```
% g4 = Gamma mixture
% R4 = Rmixture
% T4 = Tmixture
% P4 = Pmixture

g4 = 1.4;
g1 = 1.3926;
R4 = 287;
R1 = 324;
T1 = 297.15;
T4 = 297.15;
p4 = 423.9674e3;
p1 = 94000;
a4 = sqrt(g4*R4*T4);
a1 = sqrt(g1*R1*T1);
p2p1 = [100:1:1500]';

% gp = g1+1
% gm = g1-1
gpgm = (g1+1)/(g1-1);
rho2rho1 = (1+gpgm*p2p1)./(gpgm+p2p1);
Ms = sqrt((g1+1)/2/g1*(p2p1-1)+1);
W = Ms*a1;
up = W.*(1-1./rho2rho1);
a = Ms./(Ms.^2-1).*sqrt(1+2*(g1-
1)/(g1+1).^2.*(Ms.^2-1).*(g1+1./Ms.^2));
b = -1;
c = -a;
Mr = (-b+sqrt(b.^2-4*a.*c))/2./a;
p4p1 = p2p1.*(1-(g4-1)*a1/a4*(p2p1-
1)./sqrt(2*g1*(2*g1+(g1+1)*(p2p1-1)))).^(-
2*g4/(g4-1));
p5p2 = 1 + 2*g1/(g1+1)*(Mr.^2-1);
p5p1 = p5p2.*p2p1;
```

```
rho5rho2 = (1+gpgm*p5p2)./(gpgm+p5p2);
rho5rho1 = rho5rho2.*rho2rho1;
T5T1 = p5p1./rho5rho1;

% Interpolate
p2p1_perfect = interp1(p4p1,p2p1,p4/p1)
p5p1_perfect = interp1(p2p1,p5p1,p2p1_per-
fect);
T5T1_perfect = interp1(p2p1,T5T1,p2p1_per-
fect);

% delete ratio
% P5 = Reflected shock from incident
p5_p = p5p1_perfect*p1
T5_p = T5T1_perfect*T1
Ms_p = sqrt((g1+1)/2/g1*(p2p1_perfect-1)+1);
W_p = Ms_p*a1

% P2 = incident shock
p2_perfect = p2p1_perfect*p1
p4p2 = p4/p2_perfect
```

- Ideal gas Ludwieg tunnel calculations for comparison

```
P4 = 182175.1;
T4 = 346.85;

% Adt == cnst
Adt = 3017.54;

% Aa == A* == cnst
Aa = 120;
g4 = 1.356;
R4 = 366.9512;
a4 = sqrt(g4*R4*T4)
M2dt = [0.0001:0.00001:1];
AaAdt = (M2dt.*(((2/(g4+1))*(1+((g4-
1)/2*M2dt))).^((g4-1)/(g4+1)))).^0.5;
M2dtperfect = interp1(AaAdt,M2dt,Aa/Adt);
Mdt = M2dtperfect^(1/2);
Tdt = T4/((1+(((g4-1)/2)*Mdt)) ^2);
P3 = ((Tdt/T4)^(g4/(g4-1)))*P4
adt = sqrt(g4*R4*Tdt);
u3 = (2*(a4-adt))/(g4-1);
refspeed = u3+adt
```

- Mach number distribution along the nozzle centerline by the design characteristic curve

```
g = 1.395;
R = 50;
% 20; % radius of curvature of throat relative
to throat height (half height)
hstar = 1;
% set up axial distance points - all normal-
ized by throat half-height
dx = 0.01;
x = [-R/20:dx:R/20]';
% referenced to physical throat location
% calculate local nozzle height at each point
h = hstar + (R-sqrt(R^2-x.^2));
% initialize M array
M = zeros(size(x));
% solve for Mach number
for i = 1:length(h),
    AR = h(i)/hstar;
    if x(i) < 0,
        Mstart = 0.9;
    else
        Mstart = 1.1;
    end
    M(i) = fzero(@(M) solveAR(AR,M,g),Mstart);
end
% replace solved value at x = 0 with M = 1
(equation solving is inaccurate
% for this case)
ifind0 = find(x == 0);
M(ifind0) = 1;
% find indices of Mach numbers in transonic
region -- another attempt to
% eliminate invalid results
ifindvalid = find((M > 0.85)&(M < 1.15));

% fit a polynomial (5th order) to Mach number
distribution because seems to
% have errors in vicinity of throat
```

```
p = polyfit(x(ifindvalid),M(ifindvalid),5);
Mfit = polyval(p,x);

% calculate values of gradient numerically
dMfitdx = (Mfit(3:end)-Mfit(1:end-2))/(2*dx);
dMdx = (M(3:end)-M(1:end-2))/(2*dx);
% and plot
%plot(x(2:end-1),dMdx,x(2:end-1),dMfitdx)

% specify the exit conditions
Mexit = 3.5;
% 3.7; fsolve(@(M)
solveM(AexitonAstar,M,g),1.1);
AexitonAstar = AonAstar(Mexit,g);
hexit = AexitonAstar*hstar;
mu_exit = asin(1/Mexit);

% specify values at extremes of the required
Mach number profile
% within the nozzle expansion
x0 = 0; M0 = 1;
x2 = 100/1.5;
% nozzle exit location relative to throat,
normalised units
x1 = x2-hexit/tan(mu_exit); M1 = Mexit;
dMdx0 = sum(p(1:5).*[5*x0^4 4*x0^3 3*x0^2 2*x0
1]);
dMdx1 = 0;
% sum(p(1:5).*[5*x1^4 4*x1^3 3*x1^2 2*x1 1]);
d2Mdx20 = sum(p(1:4).*[20*x0^3 12*x0^2 6*x0
1]);

% solve for coefficents for 4th order poly
A = [x0^4 x0^3 x0^2 x0 1; x1^4 x1^3 x1^2 x1 1;
     4*x0^3 3*x0^2 2*x0 1 0; 4*x1^3 3*x1^2
2*x1 1 0;
     12*x0^2 6*x0 2 0 0];
b = [M0; M1; dMdx0; dMdx1; d2Mdx20];
coeff = A\b;

% number of points along axis for MOC solution
```

```
nptsAxis = 15;
xstart = 5;
dXaxis = (x1-xstart)/(nptsAxis-1);
Xaxis = [xstart:dXaxis:x1]
% Xaxis = log-
space(log10(x0+1+0.3),log10(x1+1),nptsAxis)-1;
Maxis = polyval(coeff,Xaxis)
dMaxisdx = sum([Xaxis'.^3 Xaxis'.^2 Xaxis'
ones(length(Xaxis),1)].* ...
          (ones(length(Xaxis),1)*[4*coeff(1)
3*coeff(2) 2*coeff(3) coeff(4)]),2);
d2Maxisdx2 = sum([Xaxis'.^2 Xaxis'
ones(length(Xaxis),1)].* ...
          (ones(length(Xaxis),1)*[12*coeff(1)
6*coeff(2) 2*coeff(3)]),2);

figure(1)
plot(x,M,'bs',x,Mfit,'r',Xaxis,Maxis,'-ok')
xlabel('axial distance from throat')
ylabel('Mach number')

figure(2)
plot(Xaxis,Maxis,Xaxis,dMaxisdx',Xaxis,d2Max-
isdx2')

% number of points along nozzle exit C+ for
MOC solution
dXexit = (Xaxis(end)-Xaxis(end-1))*0.6; %
first estimate
dXexit = (x2-x1)/round((x2-x1)/dXexit); % ac-
tual value
Xexit = [x1:dXexit:x2]';
Yexit = tan(mu_exit)*(Xexit-x1);
nptsExit = length(Xexit);
figure(2)
plot(Xaxis,ze-
ros(size(Xaxis)),'s',Xexit,Yexit,'o')

% initialize flow angle and Mach number arrays
for ...
```

```
% throat region
theta_t = zeros(nptsAxis,nptsAxis);
M_t = zeros(nptsAxis,nptsAxis);
M_t(1,:) = Maxis;
xmoc_t = zeros(nptsAxis,nptsAxis);
xmoc_t(1,:) = Xaxis;
ymoc_t = zeros(nptsAxis,nptsAxis);
mdotp_t = zeros(nptsAxis,nptsAxis);
% cumulative mass flux from centre plane along
C+
mdotm_t = zeros(nptsAxis,nptsAxis);
% ... along C-

figure(3)
Xarc = [0:R/20:R/2]';
Yarc = -sqrt(R^2 - Xarc.^2) + (1+R);
plot(xmoc_t(1,:),ymoc_t(1,:),'s',Xarc,Yarc)
% ,xmoc_e(1,:),ymoc_e(1,:),'d')

% initialize contour array
ncp = 0; ncm = 0;

X0 = x0;
X1 = x1;
X2 = x2; Y2 = hexit;

% first calculate the throat region by march-
ing upwards off the centre
% plane
N = nptsAxis;
for i = 1:nptsAxis-1,
    for j = 1:N-1,
        M1 = M_t(i,j);
        M2 = M_t(i,j+1);
        theta1 = theta_t(i,j);
        theta2 = theta_t(i,j+1);
        x1 = xmoc_t(i,j); x2 = xmoc_t(i,j+1);
        y1 = ymoc_t(i,j); y2 = ymoc_t(i,j+1);
        [theta3,M3,x3,y3,dmdotp,dmdotm] =
unit_pro-
cess(theta1,M1,x1,y1,theta2,M2,x2,y2,g);
```

```
        theta_t(i+1,j) = theta3;
        M_t(i+1,j) = M3;
        xmoc_t(i+1,j) = x3;
        ymoc_t(i+1,j) = y3;
        mdotp_t(i+1,j) = mdotp_t(i,j)+dmdotp;
        mdotm_t(i+1,j) =
mdotm_t(i,j+1)+dmdotm;
        fracp = (1-mdotp_t(i,j))/dmdotp;
        fracm = (1-mdotm_t(i,j+1))/dmdotm;

        figure(3)
        hold on

plot(x1,y1,'s',x2,y2,'s',x3,y3,'rd',[x1
x3],[y1 y3],[x2 x3],[y2 y3])
        if (fracp >= 0)&(fracp <= 1),
            xcp = x1 + fracp*(x3-x1);
            ycp = y1 + fracp*(y3-y1);
            plot(xcp,ycp,'ks')
            ncp = ncp + 1;
            cont_p(ncp,1:2) = [xcp,ycp];
        end
        if (fracm >= 0)&(fracm <= 1),
            xcm = x2 + fracm*(x3-x2);
            ycm = y2 + fracm*(y3-y2);
            plot(xcm,ycm,'ks')
            ncm = ncm + 1;
            cont_m(ncm,1:2) = [xcm,ycm];
        end
     end
    N = N - 1;
end

% intialize ...
% nozzle straightening region approaching exit
theta_e = zeros(nptsAxis,nptsExit);
M_e = zeros(nptsAxis,nptsExit);
M_e(1,:) = ones(1,nptsExit)*Mexit;
xmoc_e = zeros(nptsAxis,nptsExit);
xmoc_e(1,:) = Xexit;
```

```
ymoc_e = zeros(nptsAxis,nptsExit);
ymoc_e(1,:) = Yexit;
mdotp_e = zeros(nptsAxis,nptsExit);
% cumulative mass flux from centre plane along
C+
gp = g+1; gp2 = gp/2;
gm = g-1; gm2 = gm/2;
gp2gm = gp2/gm;
mdotp_e(1,:) =
Mexit*((1+gm2)/(1+gm2*Mexit^2))^gp2gm*Yexit;
mdotm_e = zeros(nptsAxis,nptsExit);
% ... along C-
mdotm_e(1,:) = mdotp_e(1,:);

for i = 2:nptsAxis,
    theta_e(i,1) = theta_t(i,nptsAxis+1-i);
    M_e(i,1) = M_t(i,nptsAxis+1-i);
    xmoc_e(i,1) = xmoc_t(i,nptsAxis+1-i);
    ymoc_e(i,1) = ymoc_t(i,nptsAxis+1-i);
    mdotp_e(i,1) = mdotp_t(i,nptsAxis+1-i);
    mdotm_e(i,1) = mdotm_t(i,nptsAxis+1-i);
end

% now calculate flow straightening region by
marching upwards off the centre
% plane
for j = 1:nptsExit-1,
    for i = 1:nptsAxis-1,
        M1 = M_e(i+1,j);
        M2 = M_e(i,j+1);
        theta1 = theta_e(i+1,j);
        theta2 = theta_e(i,j+1);
        x1 = xmoc_e(i+1,j); x2 =
xmoc_e(i,j+1);
        y1 = ymoc_e(i+1,j); y2 =
ymoc_e(i,j+1);

        figure(3)
       % [x1 y1 x2 y2]
        plot(x1,y1,'*m',x2,y2,'*g')
```

```
        [theta3,M3,x3,y3,dmdotp,dmdotm] =
unit_pro-
cess(theta1,M1,x1,y1,theta2,M2,x2,y2,g);
        theta_e(i+1,j+1) = theta3;
        M_e(i+1,j+1) = M3;
        xmoc_e(i+1,j+1) = x3;
        ymoc_e(i+1,j+1) = y3;
        mdotp_e(i+1,j+1) =
mdotp_e(i+1,j)+dmdotp;
        mdotm_e(i+1,j+1) =
mdotm_e(i,j+1)+dmdotm;
        fracp = (1-mdotp_e(i+1,j))/dmdotp;
        fracm = (1-mdotm_e(i,j+1))/dmdotm;

        figure(3)
        hold on

plot(x1,y1,'s',x2,y2,'s',x3,y3,'rd',[x1
x3],[y1 y3],[x2 x3],[y2 y3])
        if (fracp >= 0)&(fracp <= 1),
            xcp = x1 + fracp*(x3-x1);
            ycp = y1 + fracp*(y3-y1);
            plot(xcp,ycp,'ks')
            ncp = ncp + 1;
            cont_p(ncp,1:2) = [xcp,ycp];
        end
        if (fracm > 0)&(fracm <= 1),
            xcm = x2 + fracm*(x3-x2);
            ycm = y2 + fracm*(y3-y2);
            plot(xcm,ycm,'ks')
            ncm = ncm + 1;
            cont_m(ncm,1:2) = [xcm,ycm];
        end
    end
end

cont_all = [cont_p; cont_m];
cont_all = sort(cont_all,1);
cont_all(end+1,1:2) = [X2,Y2];
```

```
p = polyfit(cont_all(:,1),cont_all(:,2),5);
xplt = [0:1:X2,X2]';
yplt = polyval(p,xplt);

figure(4)
plot(cont_p(:,1),cont_p(:,2),'s',cont_m(:,1),c
ont_m(:,2),'o',cont_all(:,1),cont_all(:,2),xpl
t,yplt)


function [theta3,M3,x3,y3,dmdotp,dmdotm] =
unit_pro-
cess(theta1,M1,x1,y1,theta2,M2,x2,y2,g);
%
% 1 to 3 follows C+
% 2 to 3 follows C-
% theta = flow angle
% nu = Prandtl-Meyer function
% mu = Mach angle
% dmdotp = local mass flux across C+ charac-
teristic normalised by mdot*
% dmdotm = local mass flux across C- charac-
teristic normalised by mdot*
%
nu1 = PMfunction(M1,g);
nu2 = PMfunction(M2,g);
K1p = theta1 - nu1;
K2m = theta2 + nu2;
nu3 = (K2m - K1p)/2;
theta3 = (K1p + K2m)/2;
if nu3 == 0,
    M3 = 1,
else
    M3 = fzero(@(M) solvePM(nu3,M,g),M2);
end
mu1 = asin(1/M1);
mu2 = asin(1/M2);
mu3 = asin(1/M3);
m13 = (theta1 + mu1 + theta3 + mu3)/2;
m32 = (theta3 - mu3 + theta1 - mu1)/2;
```

```
x3 = (y2 - y1 + m13*x1 - m32*x2)/(m13 - m32);
y3 = y1 + m13*(x3 - x1);
% Average Mach numbers
Mp = (M1+M3)/2; Mm = (M2+M3)/2;
% Average flow angles
thetap = (theta1+theta3)/2; thetam =
(theta2+theta3)/2;
% Areas normal to flow directions
dAp = ((y3-y1)-(x3-x1)*tan(thetap))*cos(the-
tap);
dAm = ((y3-y2)+(x2-x3)*tan(thetam))*cos(the-
tam);
%
gp = g+1; gp2 = gp/2;
gm = g-1; gm2 = gm/2;
gp2gm = gp2/gm;
dmdotp = Mp*((1+gm2)/(1+gm2*Mp^2))^gp2gm*dAp;
dmdotm = Mm*((1+gm2)/(1+gm2*Mm^2))^gp2gm*dAm;

function val = solvePM(nu,M,g);
val = nu - PMfunction(M,g);

function val = solveAR(AR,M,g)
val = AR-AonAstar(M,g);
```

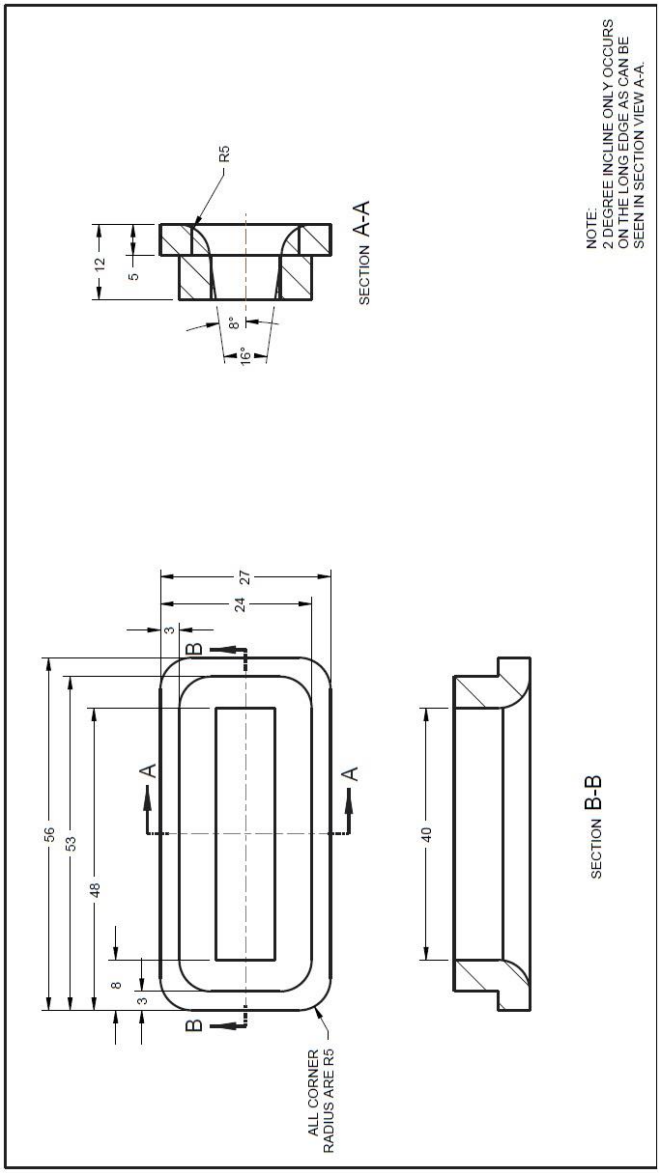

Figure 3.14 Nozzle inlet figure

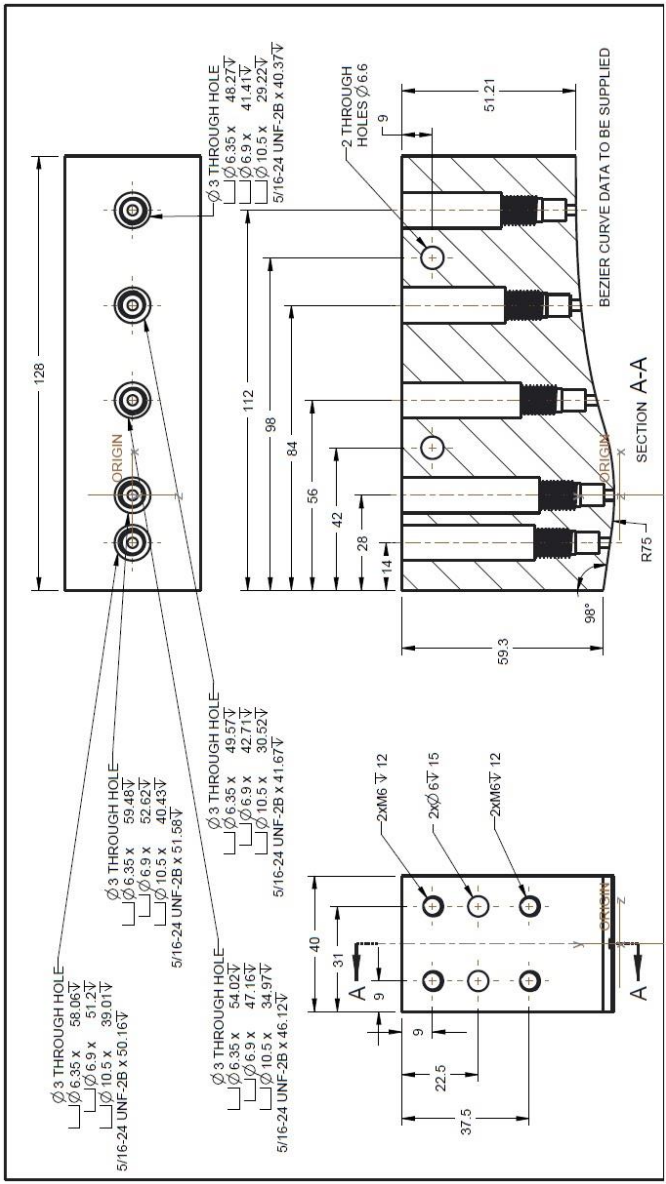

Figure 3.15 Nozzle throat and expansion

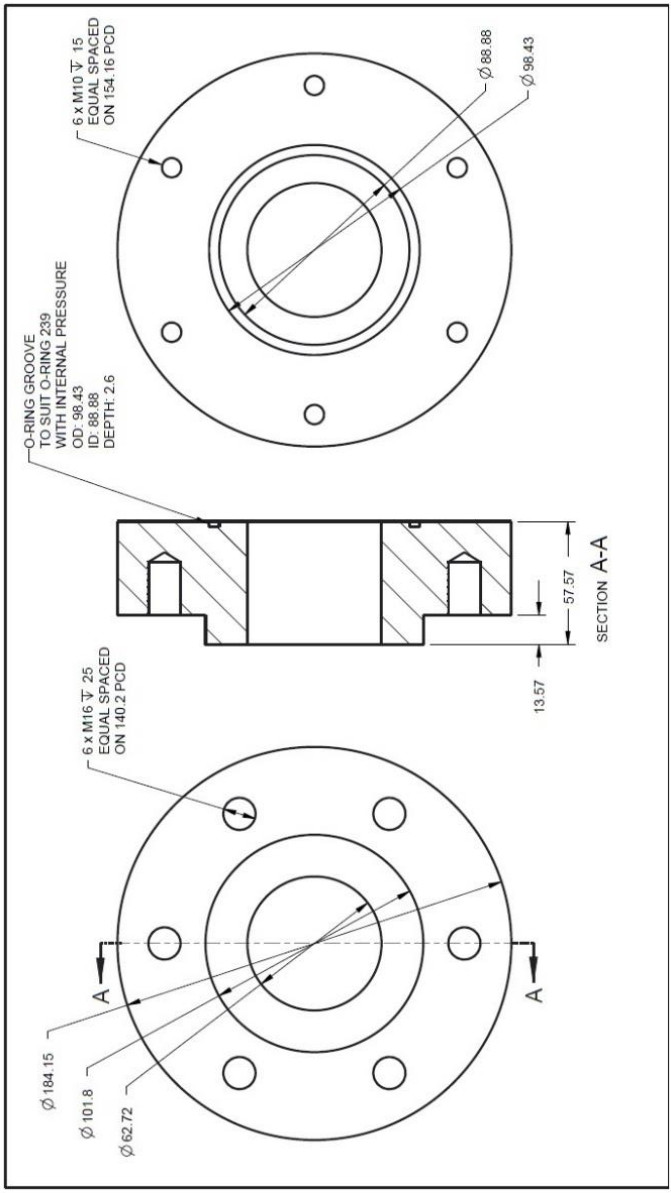

Figure 3.16 Nozzle connector

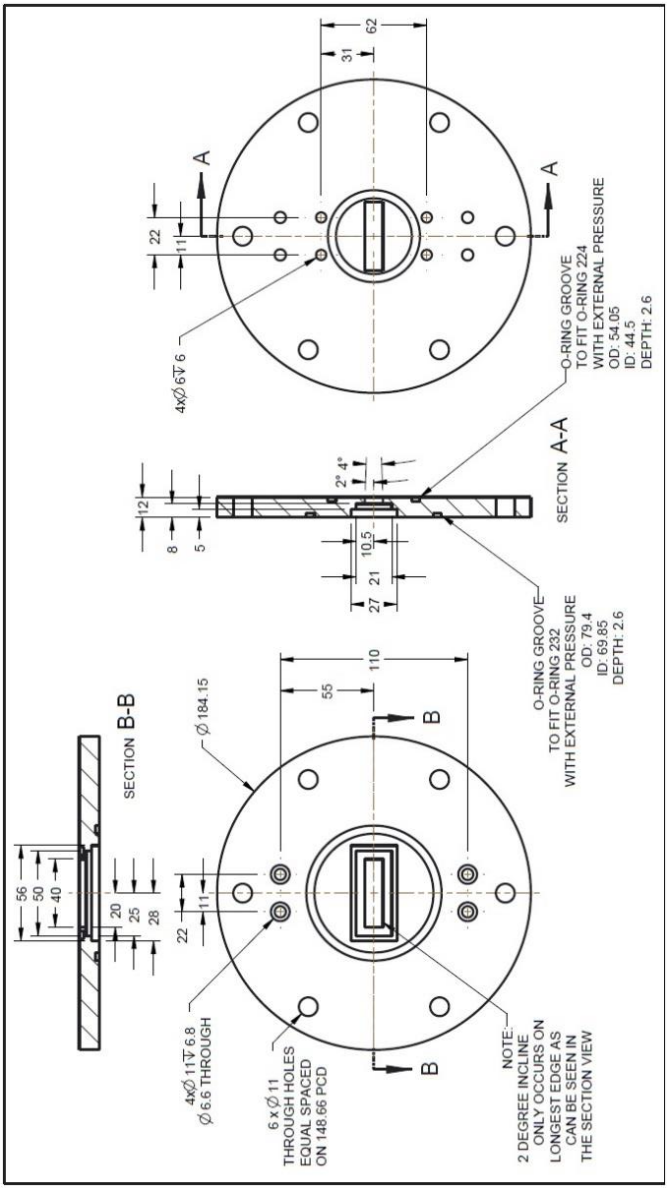

Figure 3.17 Nozzle flange